Repository Istituzionale dei Prodotti della Ricerca del Politecnico di Bari

Multidimensional Dynamic Analysis of Human Brain Connectivity

This is a PhD Thesis

Original Citation:
Multidimensional Dynamic Analysis of Human Brain Connectivity / Lombardi, Angela. - (2018).
[10.60576/poliba/iris/lombardi-angela_phd2018]

Availability:
This version is available at http://hdl.handle.net/11589/120525 since: 2018-01-20

Published version
DOI:10.60576/poliba/iris/lombardi-angela_phd2018

Publisher: Politecnico di Bari

Terms of use:

(Article begins on next page)

24 June 2026

Politecnico di Bari

Department of Electrical and Information Engineering
Electrical and Information Engineering
Ph.D. Program
SSD: ING-INF/03–Telecommunications

Final Dissertation

Multidimensional Dynamic Analysis of Human Brain Connectivity

---

by
Angela Lombardi:

Supervisors:

Prof. Cataldo Guaragnella

Dott.ssa Sabina Tangaro

Coordinator of Ph.D Program:
Prof. Vittorio Passaro

Course n°30, 01/11/2014-31/10/2017

Acknowledgements

I would like to express my gratitude to all the people who supported me during the PhD course.

I'm grateful to my supervisors, Cataldo Guaragnella and Sonia Tangaro, for the active contribution they have made to the research carried out and for the valuable advice received during the writing of the articles and the thesis work.

I'm also thankful to Roberto Bellotti for inviting me to join the Medical Physics Research Group where I have been able to actively discuss problems related to Computational Neuroscience.

Finally, I would express my special thanks to my colleagues and friends Angelo Cardellicchio, Eufemia Lella, Giuseppe Dentamaro and Gennaro Vessio and to Graziano De Scisciolo for the useful scientific debates and for making this important journey more pleasant.

Abstract

The human brain is one of the most complex system existing in nature. The emergence of cognitive and physiological phenomena is the outcome of a complex series of interactions that occur hierarchically. Hence, explaining cognition is not possible just by taking into account the single parts the brain is composed of, but a comprehensive view of the collective behaviors of its constituents and the interactions with its environment should be considered to study the global system behavior. A network formulation simplifies the analysis of a complex system by providing mathematical tools able to capture different aspects of its organization in a compact manner. Graph theoretical methods have been extensively applied to many neuroimaging datasets in order to describe the topological properties of both functional and structural brain networks. Although these methods have become a gold standard for analyzing the complex behavior of the human brain, several important issues related to the identification of the networks, their temporal evolution and new complex metrics for their topological description need to be further explored in order to provide a general and comprehensive analysis framework. Indeed, the human brain is a highly flexible dynamic system: executing both complex and simple functions requires the ongoing reconfiguration of the connections among the general- and specific-domain subsystems. In this work, some methodological procedures are proposed to address the outlined issues. Firstly, a new synchronization-based metric is developed to assess the functional connectivity in human brain through functional magnetic resonance imaging (fMRI). In details, the whole brain volume is partitioned into regions of interest (ROIs) and a phase-space framework is used to map pairs of signals of each region of interest, in their reconstructed phase space, i.e. a topological representation of their behavior under all possible initial conditions. Cross recurrence plots (CRPs) are then employed to reduce the dimensionality of the phase space and compare the trajectories of the interacting systems. The synchronization metric is then extracted from the cross recurrence to assess the coupling behaviour of the

time series. The proposed metric is a generalized synchronization measure that takes into account both the amplitude and phase coupling between pairs of fMRI series. It differs from the correlation measures used in the literature, as it seems to be more sensitive to nonlinear coupling phenomena between time series and it is more robust against the physiological noise. Then an extended multidimensional framework is presented to describe completely the functional interactions of couple of signals in the phase space. More specifically, a set of metrics is extracted from the CRP of each couple of signals to form a multilayer connectivity matrix in which each layer is related to a specific complex phenomenon occurring in phase space. Hence, machine-learning algorithms are used to identify markers of the dynamic states in brain activity to characterize pathological conditions in a clinical context. Finally, a new perspective to characterize node centrality in complex networks is discussed and some preliminary results of the application of a new resilience index are shown. This metric quantifies the importance of the node in relation to its survival rate for progressive removal of links in the network and can be useful for identifying the most persistent nodes in a network.

Table of contents

List of figures

List of tables

Nomenclature

Roman Symbols

ACC Accuracy

ADL Average Diagonal Line Length

AUC Area Under ROC Curve

BOLD Blood Oxygen Level-Dependent

CRP Cross Recurrence Plot

DET Determinism

DTI Diffusion Tensor Imaging

EDL Entropy of Diagonal Length

EEG Electroencephalography

ENTR LOS Entropy of LOS

FA Fractional Anisotropy

fMRI Functional Magnetic Resonance Imaging

FN False Negatives

FNN False Nearest-Neighbors

FP False Positives

GM Gray Matter

HARD SYNC Hard Synchronization

ICNs Intrinsic Connectivity Networks

LAM Laminarity

LLD Length of the Longest Diagonal Line

LLV Length of the Longest Vertical Line

LOS Line of Synchronization

MD Mean Diffusivity

MEG magnetoencephalography

NC Normal Controls

NMI Normalized Mutual Information

ROI Region of Interest

RPDE Recurrence Period Density Entropy

RR Recurrence Rate

RT1 Recurrence Times of First Type

RT2 Recurrence Times of Second Type

sMRI Structural Magnetic Resonance Imaging

SVM-RFE Support Vector Machine-Recursive Feature Elimination

SYNC Synchronization Index

TBI Traumatic Brain Injury

TN True Negatives

TNR True Negative Rate

TP True Positives

TPR True Positive Rate

TRANS Transitivity

TT Average Length of Vertical Lines

WM White Matter

Chapter 1

Introduction

Physiological and biological systems can be imagined as complex processes whose dynamics are continuously influenced by nonlinear interactions. In particular, the complexity of the brain arises from different aspects. The brain has a complex temporal and spatial multi-scale structure, from which emerging cellular and neuronal phenomena form the physical and biological basis of cognition [1]. On the microscopic scale, neurons are connected through axonal, dendritic connections and synaptic terminals, forming both local and global neuronal circuits. At mesoscales and macroscales, neural columns and large-scale brain regions are interconnected by short- and long-range axonal white matter projections, forming a brain-wide network of neural interactions [2]. In addition, it exhibits a hierarchical fractal organization: the structure within any given scale is organized into anatomically and functionally modules which can be adapted to external conditions [3, 4].

In order to understand the dynamics that regulate both structure and function of the human brain, in recent decades, scientists have felt the need to leave a reductionist approach, based on detailed investigations of the various tissues that compose it, with the aim to incorporate the dense network of relationships and mechanisms of large-scale synchronization that are the basis of the functioning of neuronal networks. The term "connectome" was coined to indicate a complete map of the neural elements and structural links within a neural system, together forming the fundamental substrate for neural communication, information processing and neural integration in the brain [5]. Mapping the brain's structural organization and understanding how neural function is related to connectome is one of the main goal of the modern neuroscience. Complex network theory provides a powerful mathematical framework to study human brain

networks [6, 2, 7]. The network formulation describes the brain as a graph composed by nodes (i.e., brain regions) linked by edges (their structural/functional connectivity).

Neuroimaging techniques have been of fundamental importance in the connectomics' advances. They are currently the main methods to investigate the macroscale connectome architecture of human brain [8]. Both the rapid development of innovative analysis techniques and the growing interest of the scientific community have produced a large amount of available data concerning the different structural and functional nature of the brain. These data are often shared in projects and collaborations to improve the current understanding of the brain by combining different approaches and heterogeneous data [9, 10]. In this context, it is necessary to develop multidimensional processing techniques covering the various ways in which the brain can be examined and identify new topological descriptors that consider also their multidimensional nature.

For example, in order to take into account simultaneously the dynamic relations in time and space of brain activity, some techniques have been proposed. A number of them aim at partitioning the brain activity into a specif domain (time or frequency) and observing its evolution. Most of these processing techniques assume linear functioning. However, neurodynamics are characterized by complex and nonlinear phenomena that arise from feedback responses to environmental stimuli and physiological interactions among various subsystems that comprise the brain [11]. Nonlinear dynamic principles and nonlinear time series tools have been exploited for in-depth investigation of neuronal transient responses and coupling mechanisms with the goal of enhancing the understanding of human cognition and dynamic processes underlying normal and pathological brain states [12]. A key aspect of dynamical analysis is the reconstruction of the phase space of a system. Both local and global changes of its dynamics can be inferred by means of complexity and stability measures in the phase space [13]. Dynamical analysis methods have been extended for bivariate characterization of coupled interactive systems. Specifically, generalized synchronization measures have been suggested to assess the dynamic interaction of neurophysiological signals in their reconstructed phase space [14–16]. In detail, generalized synchronization between couple of signals is measured by mapping the manifolds of the signals into a common phase space and then comparing their local neighboring states. In this work, a novel framework to capture such dynamics is presented. It exploits a phase-space approach to observe brain signals in a generalized way. The main goal of the framework is to achieve a

multidimensional representation of the interaction between couple of signals in order to provide an effective measure of synchronization.

Another important aspect of complex network analysis concerns the definition of new metrics that can characterize real complex systems dynamically and in a multidimensional way. In fact, most of the current graph metrics are defined on binary networks, and only few extensions have been introduced for generalized networks. However, real networks, including the brain, have heterogeneous links whose weights quantify the importance of connections. Such links should be considered to properly model complex processes and avoid overly penalizing simplifications [17]. In this thesis, an alternative weighted metric of centrality based on the concept of both node and link resilience is introduced. The importance of nodes and links is evaluated by taking into account the multidimensional relations between each node and the rest of the network in a dynamical percolation context.

Finally, the establishment of large sample size datasets and the increasing accumulation of published findings, need powerful and advanced tools to select network-based and image-based effective biomarkers for predicting severity disease, mental states, improving diagnosis and so on [18]. At this aim, a great variety of multivariate methods and machine learning algorithms have been applied to investigate brain complex networks. Traditional univariate methods treat the brain features as independent variables, thus ignoring the potential relationships that could exist among them. Conversely, multivariate methods consider multidimensional patterns that can potentially reveal more insights into the structural and functional architecture of the brain [19]. Machine learning methods are a special case of multivariate statistical methods. They allow not only to evaluate sets of features at the same time, but also to provide predictive models that can be used as diagnostic tools. In this work, several aspects related to the application of machine learning algorithms on neuroimaging data are highlighted. In particular, this thesis covers topics related to the problem of feature selection, the proper choice of the predictive model for different contexts, the comparison between different models and the strategies for validating the obtained results.

Structure of the thesis

The rest of the thesis is therefore organized as follows:

- Chapter 2 provides background knowledge both on the formalism and tools of complex networks analysis together with the recent advances in this field;
- Chapter 3 concerns the proposal of a new synchronization metric in the phase-space domain. The results presented in this chapter have been published in [20];
- In Chapter 4 the full multidimensional phase-space framework is exposed. Preliminary results of the framework have been presented in [21, 22];
- Chapter 5 shows a new resilience centrality metric for identifying the most persistent nodes of a complex network. Some results presented in this chapter have been also published in [23].
- Chapter 6 shows the results achieved during two international challenges on the application of multidimensional methods for features selection in classification of individuals with brain lesions and cognitive decline. This discussion was necessary in order to bring down the proposed methods in a real context. The results and the methods presented in this chapter have been published in [24, 25].
- Chapter 7 concludes the thesis and depicts future developments of the research conducted so far.

Chapter 2

State of the Art

2.1 From Brain to Networks

The human brain is composed by billions of neurons connected by trillions of synapses [26]. Ideally, all possible combinations of the connections among these basic elements should be considered to describe the static and dynamic architecture of the brain. However, if on the one side this description is not computationally feasible, on the other side it is important to bear in mind that cognitive phenomena are expressions emerging from the large-scale behavior of neuronal populations [27]. Network modeling and analysis uses brain observation methods and effective mathematical tools to make these behaviors easy-to-interpret and understand.

2.1.1 Neuroimaging and physiological recordings

Noninvasive neuroimaging techniques are currently the most promising methods for mapping the human brain.

Structural magnetic resonance imaging (sMRI) and diffusion tensor imaging (DTI) allow anatomical mapping of brain regions and their structural connections at high spatial resolution (order of millimeter). Structural MRI provides a comprehensive description of the integrity of the brain. MRI signal varies across tissue types because of different distributions of cell bodies (e.g., neurons, glial cells and myelinated axons) and such differences are visualized in volumetric MRI scan sequences [28]. Structural measurements of volume, thickness, and surface area of specific regional gray (GM) and white-matter (WM) structures are used to examine the anatomy and pathology of the brain as well as to infer structural connectivity [5, 7]

Diffusion tensor imaging measures the water diffusion along the WM fibers and can thus provide useful information regarding their integrity and direction[29]. The spatial orientation of the fibers within each voxel of the brain is related to the maximum value of diffusion anisotropy so the trajectories of axonal fibers can be reconstructed through tractography algorithms[30]. These algorithms aim at estimating the presence of WM pathways by using the distribution of diffusion anisotropy and can include both deterministic and probabilistic approaches [31]. In addition, several invariants can be derived from the diffusion tensor. As an example, high values of fractional anisotropy (FA) and low values of mean diffusivity (MD) are able to identify healthy axons since in non-pathological conditions, the water diffusion along an axon is constrained almost completely to one direction [32].

Functional magnetic resonance imaging (fMRI) and noninvasive electrophysiological recordings such as electroencephalography (EEG) and magnetoencephalography (MEG) , are the techniques most commonly used to investigate brain activity. MEG assesses electrical activity in the human brain, based upon measurement of changes in magnetic field above the scalp induced by synchronized neural current flow [33], while EEG measures voltage fluctuations resulting from ionic current within the neurons [34]. Both methods provide recordings that directly reflect neural activity with high temporal resolution, but their spatial resolution is limited by the number of electrodes or sensors. A great variety of signal processing techniques have been developed to analyze the time and spectral content of EEG and MEG recordings, especially for recognition of activity patterns in studies of brain disorders [35].

Functional magnetic resonance imaging measures the blood oxygen level-dependent (BOLD) signal which is related to the magnetic susceptibility of the blood caused by a change in oxygenation level. fMRI provides an indirect measurement of neuronal activity as the BOLD signal is determined by the interactions of different physiological quantities such as oxygenation level, volume and blood flow. This technique offers a great spatial resolution (at millimeter-scale), but its time resolution is limited by the slow BOLD response (order of seconds) [36].

2.1.2 Brain Connectivity

Brain connectivity can be defined on different time and spatial scales in several manners that reflect the neuroimaging and neural recording techniques [2]. Generally, three categories of connectivity are recognized:

- *Structural connectivity* describes anatomical links among neural elements. This kind of connectivity is considered stable on shorter time scales (from seconds to minutes), but may change over longer time scales (from hours to days).
- *Functional connectivity* is derived from EEG, MEG or fMRI time series and attempts to describe dynamic interactions among neural elements. It is highly non-stationary, as it is modulated by external task demands and intrinsic physiological fluctuations.
- *Effective connectivity* describes causal interactions among neural elements unveiling directed effects from time series. Like functional connectivity, it is highly time dependent and non-stationary.

2.1.3 Network modeling

Brain networks are efficiently modeled by graphs. The mathematical framework of graph theory requires the identification of nodes and edges, i.e., the basic elements of a graph. Consequently, brain networks can be derived from brain imaging and recordings by following some steps [8] which are also summarized in Figure 2.1. Briefly, the connectivity matrix that represents the associations among the nodes, can be thresholded to remove weak connections yielding to a sparse matrix, or can be analyzed in its dense form. The analysis of the connectivity matrix involves several graph metrics that reflect different properties of the network. Finally, a statistical framework can be adopted to describe such properties with respect to population of random networks (i.e., the null models) or to compare clinical populations for diagnostic purposes. The following subsections are focused on the construction of the networks. Graph analysis methods are addressed in Section 2.1.4.

1. **Nodes**

   The first step consists in defying the nodes of the network. Brain anatomical parcellation schemes are commonly used to define a partition of

brain. Anatomical atlas such as Anatomical Automatic Labeling [37], Harvard-Oxford probabilistic atlas, etc., are the most diffused in neuroscience studies. These partitioning methods define networks of moderate resolution (approximately 100 nodes) with regions of variable volumes.

Large scale networks can be obtained by considering each voxel of the brain as a node. This method leads to very high-resolution networks (about 10^4 nodes), whereby local information can be retrieved with high spatial accuracy [38]. However, the analysis of such networks, requires extensive preprocessing to filter out the large amount of noise and data redundancy.

Another approach to defining nodes in brain networks involves results from preexisting task-evoked fMRI studies to identify a set of fixed regions of interest (ROIs) with coherent activation patterns [39]. Nodes defined using meta-analysis methods are invariably, modeled by spheres typically of 3–6 mm radii, but their application is limited by the availability of imaging studies used to identify functionally coherent ROIs, so they cannot be generalized for any other analysis [40].

In physiological recordings, sensors and electrodes naturally define the nodes of the network. Hence, the resolution of the network is fixed, but the signal acquisition sites may not correspond to coherent anatomical or functional areas.

2. **Links**

Metrics of connectivity between pairs of nodes define the links of the network.

In structural connectivity, correlations in several morphometric features or some characteristics of the fiber tracts linking areas of the brain, are used to estimate connectivity matrices. In particular, in sMRI, structural connectivity is assessed by computing the correlations in the thickness or volume of gray matter between two cortical areas [41]. In DTI, the connectivity is defined by the number of the reconstructed axonal fibers linking two nodes, or by the average value of FA of the voxels within each fiber bound connecting two ROIs [42]. The connectivity matrices resulting from both the imaging techniques are weighted and undirected.

In functional connectivity analysis, statistical dependences between distributed neuronal units are commonly estimated by various measures such as correlation, covariance and spectral coherence between pairs of time series [43]. Pairwise direct associations obtained from statistical modeling and other time series analysis are used to infer effective connectivity [44]. It follows that the functional networks are weighed and undirected, while effective networks are weighed and direct since in effective connectivity causal interactions between the elements of the network are derived.

2.1.4 Network analysis

Graph metrics have been extensively used for the analysis of the brain networks [45, 6]. They quantify different topological aspects of the nodes mainly concerning their influence, integration and segregation of the network. Influence measures capture the role of nodes and edges with respect to their contribution to the information flow and integrity of the network; segregation refers to the division of the network into separate and specialized clusters, while the concept of integration is related to the degree of the global network interconnection. In the following, the most important metrics used in literature will be discussed, which cover only a subset of all the known graphs metrics. The reported metrics will be treated also in the next chapters and they refer to the generalized case of weighted and undirected networks.

- *Degree*

  In an undirected network $G(V,E)$, V and E being the set of nodes and set of links respectively, the degree k_i of a node v_i is simply the number of nodes attached to v_i:

  $$k_i = \sum_{j=1}^{N} a_{ij} \tag{2.1}$$

  where N is the number of the nodes of the network and $A = \{a_{ij}\}$ is the adjacency matrix, with $a_{ij} = 1$ if nodes v_i and v_j are connected and 0 otherwise. Degree represents the simplest centrality index as it assigns more importance to more connected nodes which have more influence over their neighbors.

- *Strength*

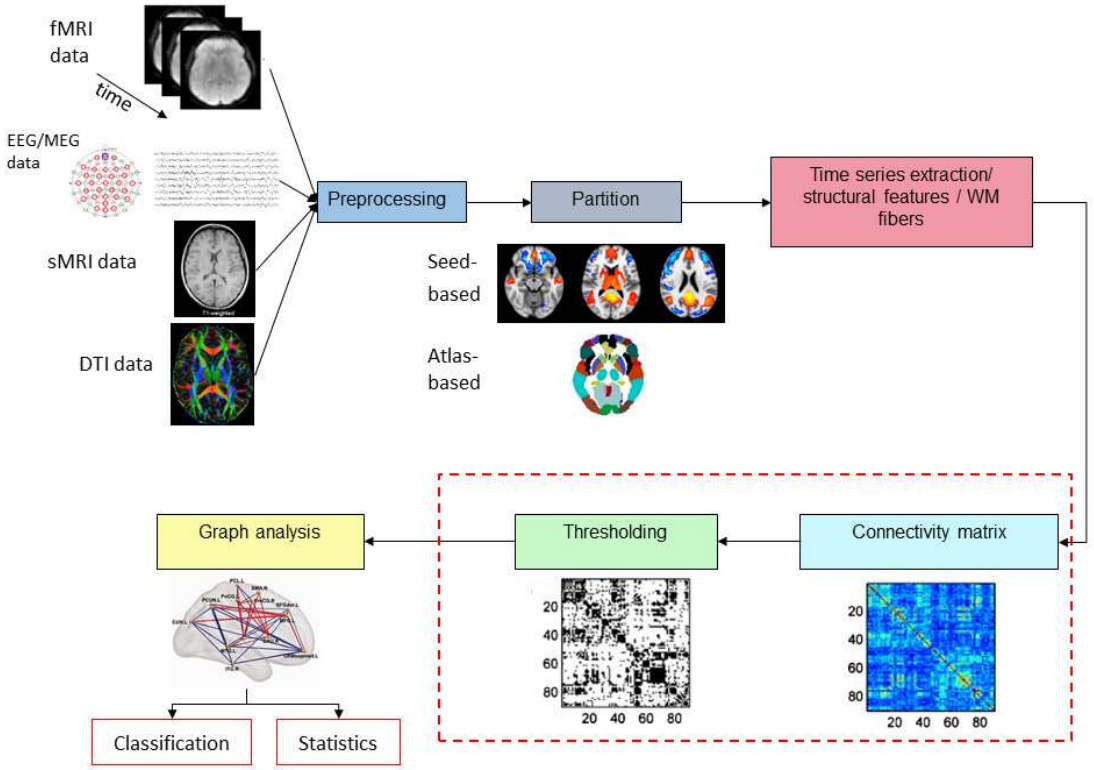

Fig. 2.1 Pipeline for brain networks modeling and analysis. After image/signal preprocessing, nodes are extracted according to a parcellation scheme (e.g. atlas-based or seed-based) or to location of sensors (for EEG/MEG). The connectivity matrix is assessed by measuring the statistical interaction between the time series of brain nodes (for functional connectivity) or correlations in the structural features/presence of WM fibers (for structural connectivity). The connectivity matrix can be thresholded and binarized or can be considered in its weight form. Graph metrics are used to quantify topological features of the brain. These features can be input to machine learning algorithms to classify diseases or particular conditions or to statistical analysis to find significant differences between clinical populations.

The importance of a node can be assigned by integrating the information about both its structural connectivity and the weights of its edges. To this aim, the strength of a node v_i is defined as the sum of the weights of the links associated to v_i:

$$s_i = \sum_{j=1}^{N} w_{ij} \tag{2.2}$$

where $W = \{w_{ij}\}$ is the weighted adjacency matrix, with $w_{ij} > 0$ if v_i and v_j are connected and $w_{ij} = 0$ if they are not connected.

- *Closeness Centrality*

  The centrality of a node can also be related to its position in the network with respect to the paths of information flow. A path from v_i to v_j is a sequence of vertices and edges, such that each edge connects its preceding with its succeeding vertex. In weighted networks, a cost criterion should be specified in order to associate weights to distances. In a general context, link weights usually do not represent the costs of connections, but their strength, so the reciprocal of weights can be directly related to their distance paths without loss of generality [46]. Let $d_G(i,j)$ be the distance between vertices v_i and v_j, i.e. the shortest path among all the paths connecting v_i and v_j that can be computed for example by using Dijkstra's algorithm[47]. Closeness centrality quantifies the proximity of each node to the rest of the network and it is expressed as:

$$CC_i = \frac{1}{\sum_{j=1}^{N} d_G(i,j)} \tag{2.3}$$

  A high value of closeness means that a node is easily reached from all the other nodes with few steps.

- *Betweenness Centrality*

  Betweenness centrality is expressed as the fraction of the shortest paths that pass through each node or edge [48]:

$$BC_i = \sum_{i \neq j \neq t} \frac{\sigma_{jt}(i)}{\sigma_{jt}} \tag{2.4}$$

  where σ_{jt} denotes the number of shortest paths from v_j to v_t and $\sigma_{jt}(i)$ denotes the number of shortest paths from v_j to v_t that pass through v_i.

Betweenness highlights nodes that, upon removal, would affect efficient routing across the network.

- *Eigenvector Centrality*

  The eigenvector centrality is an iterative centrality in which the influence of a node is determined by the number and influence of its neighbors [49]:

$$EIG_i = \frac{1}{\lambda} \sum_{j=1}^{N} w_{ij} EIG_j \tag{2.5}$$

  Where λ is the largest eigenvalue of W. Power iteration methods may be used to find efficiently the dominant eigenvector [50].

- *Pagerank centrality*

  Pagerank algorithm [51] is a variant of eigenvector centrality and was developed by Google to rank websites. Pagerank assigns the importance (i.e., PR centrality) to each web page by random walking on the network resulting from the links among the pages. At first, each page has $PR = 1$; then each page spreads the PR value to its neighbors according to the link weights along the output connections. Finally, the importance of a page is determined by both criteria of quality and quantity of the pages linked to it. The PR value of a node v_i at the step t is defined as:

$$PR_i(t) = \sum_{j=1}^{N} \frac{w_{ij} PR_j(t-1)}{s_j} \tag{2.6}$$

  The iterations will stop if the steady state of the PR values of all the pages is reached.

- *Clustering Coefficient*

  The clustering coefficient measures the density of links connecting a node with its neighbors. If the neighbors of a node are also interconnected, they form a cluster. Hence, the simplest nontrivial subgraph of clustered elements of a network is a triangle of nodes. It is defined as:

$$C_i = \frac{2}{k_i(k_i-1)} \sum_{j,k} (w_{ij} w_{jk} w_{ki})^{1/3} \tag{2.7}$$

  where $\sum_{j,k} w_{ij} w_{jk} w_{ki}$ is sum of triangle intensities attached to the node v_i [52].

- *Modularity*

  A network can be composed by different communities of nodes which act as specialized substructures whose mutual interaction define a hierarchical organization of the network [53, 54]. Communities are defined by groups of nodes that are more strongly connected to each other than all other nodes of the network. Therefore, studying the modular architecture of a network might unfold features concerning both network integration and segregation.

  Most of the existing community detection algorithms attempt to find optimal partitions of a network in a divisive fashion manner, i.e., by starting with a single cluster of all the nodes and refining divisions that delineate cohesive subsets of observations [8]. In order to assess the quality of a partition, these algorithms use a modularity index that compare the intra-module connectivity with that expected by chance, as defined by a network in which edges are randomly placed between nodes. At this aim, a null model is established to estimate the number of edges that can be expected to connect nodes within the same community by chance. So, the index of modularity is expressed as the difference between the actually within-module density of connections and that which is expected in the corresponding null model [55]:

$$Q = \frac{1}{2E} \sum_{ij} (w_{ij} - e_{ij}) \delta(m_i, m_j), \tag{2.8}$$

  where $E = \frac{1}{2} \sum_{ij} w_{ij}$ is the total weight of the links of the network, $e_{ij} = s_i s_j / 2E$ is weight of the edges linking nodes in the same community expected by chance and $\delta(m_i, m_j)$ is taken to include only edges between nodes within the same module. The index Q ranges between -1 and 1: $Q > 0$ when the intra-module connectivity of the network is higher than that expected by chance; $Q = 0$ when the actual intra-module connectivity does not differ from that of the null model; $Q < 0$ a modular structure has not been identified in the network.

  Since the optimal partition of a network corresponds to the maximum value of Q, the community detection algorithms implement optimization procedures. Indeed, identifying the best partition should ideally require the examination of all possible network partitions, but this is unreasonable as the network size increases. Instead, a great variety of the widely-used

community detection algorithms involve heuristic approaches to find a partition with near-optimal value of Q [56].

2.2 Statistics and Machine Learning in Neuroscience

Topological features of brain networks can be used as reliable markers for characterizing cognitive states, aging and diseases. In this light, statistical techniques to infer significant differences among clinical populations have been specifically developed [57]. Statistical analysis of the human brain connectivity principally involves mass univariate hypothesis testing about local level properties (i.e., nodal or/and at edge-level) to identify the specific regions or connections that are different between groups of healthy controls and patients. Although, on the one hand, performing the same hypothesis simultaneously on many elements within the brain allows an accurate localization of the areas significantly altered or most affected by the disease, on the other hand, it also leads to a multiple comparisons problem. The number of comparisons can be reduced through a priori assumptions limiting the analysis to a subset of areas. Alternatively, the problem of multiple comparisons can be tackled with statistical procedures such as false discovery rate (FDR) [58] or more recent correction techniques which take into account spatial correlation of brain areas [59].

In recent years, large efforts have been done to apply machine learning tools in neuroscience studies. This approach treats the graph metrics as vector components of an embedded space that represents the graph. Machine learning offers predictive models that can automatically extract complex patterns among multiple elements from large neuroimaging dataset in data-driven manner and with relatively few assumptions and utilize these patterns for classification or prediction [60]. In addition, machine learning techniques might successfully address some issues related to diagnostic and clinical purposes [61]. In contrast to mass univariate analysis, multivariate predictive models simultaneously evaluate sets of features to discriminate patients from controls. This has two direct consequences:

a Multivariate patterns, i. e., specific combination of features, may result better and more accurate biomarkers for specific diseases and disorders. In fact, it is possible that the univariate methods may detect overlaps between the two populations with respect to characteristics concerning individual areas of the brain. On the other hand, multivariate techniques

may have greater sensitivity when testing different configurations of the feature space [62]. Indeed, statistically significant single features may not yield high classification accuracy and vice versa [19, 63].

b Statistical approaches based on null hypothesis testing aim at finding in-sample statistical differences while classification provides information for each individual subject as the goal of classification algorithms is to predict whether a single subject (i.e., an unseen or out-of-sample example) belongs to one of the groups under investigation [19].

2.3 The Multidimensional Brain

The increasing availability of neurological data and the rapid development of improved network analysis techniques has led to many advances in human brain mapping. Many studies have explored the brain at various levels of details, confirming its multi-scale nature [64]. In particular, the brain has shown multiple spatial scales ranging from individual cells and synapses to large-scale fiber tracts and brain regions; it can be defined over temporal scales with precision ranging from milliseconds to the entire lifespan and can be explored at different topological scales ranging from individual nodes to the whole network. Current network modeling techniques have successfully captured phenomenological aspects of the brain focusing on single level of details, e.g., by identifying characteristic network topologies for healthy and disease-affected populations, by highlighting several areas important for the global efficiency of the brain during some cognitive mechanisms and at rest and so on. However, neuroimaging and physiological acquisition techniques offer different temporal resolutions that allow observing a cognitive phenomenon at distinct time scales and with multiple frequency bands. Moreover, each technique measures a different aspect of neural dynamics so combining these information could provide a better understanding of the "multidimensional" brain.

In multimodal imaging studies, two or more methods are used to collect data from the same individual. The data are then jointly analyzed to capture the cross-information in the existing data and important relationships that cannot be detected by using a single modality. For example, such kind of analysis is often exploited to understand how brain structure is coupled with brain functions, how human behavior and cognition are driven by functional or structural aspects of physiology and how different neural or metabolic signals are interrelated. Data-

fusion techniques are adopted to properly combine multimodal information in asymmetric way (e.g, when DTI is constrained by sMRI or fMRI data) or in symmetric mode when all the modalities are equally treated with the same external constraints. In symmetric data fusion, each modality is preprocessed to extract representative features such as frequency fluctuations maps from resting state functional data, FA maps from DTI, segmented GM from sMRI. Then, relationships among features of the different modalities are assessed and used to infer properties at group level [65].

The interactions between structural and functional connectivity have been also modeled by means of multilayer networks. A multilayer network is an extension of the network concept that enables multivariate connectivity data to be represented through compact tensorial structures [66]. Each layer of the tensor is a connectivity matrix that encodes a specific kind of connectivity among its nodes. Formally, the component of a multilayer network of L layers and N nodes is indicated by $M_{j\beta}^{i\alpha}$ and it expresses the connectivity between node i in layer α and node j in layer β. Although, in principle, any interlayer connection is allowed between the nodes, in neuroscience applications generally the multivariate model includes only connections between replica nodes (i.e., $M_{j\beta}^{i\alpha} = 0$ for any $i \neq j$ and $\alpha \neq \beta$, $M_{i\beta}^{i\alpha} \neq 0$ for $\alpha \neq \beta$) [66]. In a recent work, fMRI and DTI data have been used to construct a 2-layer network, whereby each layer encodes a specific modality. A statistical framework has been exploited to analyze the joint topological motifs of the multilayer brain architecture. The results indicate a nontrivial coupling between functional brain dynamics at rest and the underlying anatomical network [67].

The mathematical framework of multilayer networks extends some concepts of complex networks [68] and offers a series of metrics to comprehensively analyze the different interactions between brain components at multiple scales [66]. As a matter of fact, multilayer analysis has also been applied to examine the temporal and frequency dynamics of the brain.

As already stated, both functional and structural connectivity are not static but instead fluctuate over timescales ranging from milliseconds to years. These fluctuations have been extensively examined both in rest conditions and in the presence of specific tasks, to such an extent that the term "chronnectome" has been specifically defined to indicate a connectivity analysis model to investigate nodal activity and time-varying connectivity patterns [69]. Time series data collected from multiple brain regions or electrodes are windowed in time and functional connectivity is inferred between the ROIs for each time window. A

multilayer network is finally built where each layer represents the connectivity pattern for a specific time window. This approach presents some weaknesses such as the appropriate selection of the window length, as well as the temporal overlapping that could avoid spurious fluctuations and the proper definition of weights to assign to links connecting replica nodes between adjacent layers [66]. The multilayer formulation of dynamic connectivity nevertheless enables the application of multilayer community detection algorithms which could solve some of the problems that would otherwise arise in applying community detection at each layer individually. Indeed these algorithms have some advantages: they perform modularity maximization over the whole multidimensional structure, resolving potential ambiguities on tracking a given community over time and allowing the definition of new metrics to quantify the flexibility and stability of community formation across layers [64]. Such new metrics have been successfully used to study the reconfiguration of functional organization during learning [70], aging [71] and increased executive functions [72].

Another approach for creating a multilayer network from brain activity consists in decomposing the signal into several frequency bands for each ROI and assessing statistical correlation between couple of regions for each of these frequency bands. Interlayer links can be established among replica nodes with weights inferred from data [73] or can correspond to correlation between couple of signals across layers [74]. Multilayer frequency analysis has revealed new insights into the functional interaction of brain areas at different frequencies. For example, multilayer hubs have proven to be effective in discriminating schizophrenic patients from healthy subjects [73] and in revealing loss of nodal centrality in subjects affected by Alzheimer's disease [75]. These findings also confirm two important aspects concerning functional connectivity: (i) some frequency components usually filtered out are actually important to determine the interactions among brain regions; (ii) the multivariate analysis of all frequency bands is able to highlight salient topological properties of the brain, which are not detectable by univariate approaches.

2.4 Summary

In this chapter, the main steps needed to provide a complex network representation of the human brain have been explained. In addition, some recent advances in the study of connectivity with multivariate models that consider the multi-scale interaction of the different brain components have been illustrated.

The network analysis techniques here described will be widely used in the following chapters.

Chapter 3

Synchronization in phase-space

3.1 A new synchronization index

Over the past few years, there has been an increasing interest in inferring connectivity properties from fMRI data. Functional connectivity analysis aims at assessing the strength of functional coupling between the signal responses in distinct brain areas [43]. According to the complex network framework, the anatomical regions of interest are the nodes of the network, connected by edges resulting from the adopted interregional interaction metrics. Pairwise fMRI time series connections are usually estimated through zero-lag correlation metrics, leading to a weighted network whose links quantify the statistical similarity between pairs of regions. Different preprocessing techniques and strategies are also applied in order to extract only relevant information from the functional network, e.g., by considering only a range of weights or by applying several thresholds to filter out weak connections [76]. Functional connectivity studies have revealed interesting insights on normal functional brain organization such as property of small-worldness [77], modularity and presence of hub nodes [78], as well as the existence of critical alterations of low-frequency neural activity patterns in pathological conditions [79]. Among the proposed strategies, some techniques are more established than others, even if there is still no agreement on which ones are the most effective or appropriate.

A number of important questions regarding the identification of networks has to be addressed before considering any analysis technique. Recent studies have demonstrated that different edge definitions could affect the topological properties of brain networks obtaining variable findings [80, 81]. Thus, properties like time resolution of the physiological time series under investigation, the

effect of the observational noise, and the presence of nonlinear effects should been taken into account for selecting measures for edge definition. The low temporal resolution of fMRI data limits the number of methods that can be used to assess the statistical interactions between the time series. Linear correlation metrics, including Pearson's correlation and partial correlation, have been used in simulation environment and resting state studies, showing good performances in estimating functional connections in both cases [81, 82]. On the other hand, nonlinear phenomena in the human brain have been explored at various scales, revealing complex coupling mechanisms in both resting state and task-based neural activity [83, 14]. Most of the functional connectivity studies are focused on configurations of intrinsic connectivity networks (ICNs) and therefore did not assess complex connectivity patterns that can arise in the presence of a cognitive task. Indeed, even if a steady intrinsic network architecture has been found at rest and across a large number of tasks and conditions, task-evoked changes of functional connectivity have been also documented, proving the existence of task-specific network configurations [84]. Exploring topological changes in functional networks when the neural activity is modulated by a cognitive task could improve the understanding of some important mechanisms of human cognition, e.g., the dynamic balancing of specialization and integration of brain regions for supporting different cognitive loads [43] and the trade-off between connection cost and topological efficiency in information processing [85]. Assessing functional interactions during external tasks should require metrics that (i) are sensitive to nonlinear coupling between time series and (ii) are more robust with respect to noise.

In this chapter, a novel approach for quantifying functional coupling between fMRI time series and constructing functional brain networks is presented. A phase-space framework is used to map pairs of signals in their reconstructed phase space, i.e. a topological representation of their behavior under all possible initial conditions [13]. This method assumes that each signal represents a projection of a higher-dimensional dynamical system evolving in time, whose trajectories are embedded into a manifold, i.e., a region of its phase space. Cross recurrence plots (CRPs) [86] are then employed to reduce the dimensionality of the phase space and compare the trajectories of the interacting systems. A synchronization metric is finally extracted from the CRP to assess the coupling behavior of the time series.

The proposed metric and the Pearson's correlation coefficient are applied to the fMRI data of a cohort of healthy subjects acquired during performance a working memory task to construct weighted networks.

At macroscopic level, functional related brain regions exhibit similar BOLD responses. These groups of regions form dense communities that reflect the functional organization of the brain and whose properties can be linked to the topological features of the task-evoked network configuration [87, 88]. The analysis carried out in this thesis aims at investigating some properties of the modular structure of task-evoked functional networks obtained with the Pearson's correlation metric and the proposed synchronization index in order to understand which index can better highlight the functional organization of distinct sub-systems involved in the specific working memory task. Therefore, a modularity algorithm is used to determine the community structure of each functional network. The within-group similarity of communities is evaluated and exploited to verify whether the metrics are sufficiently robust against noise and effective to reveal correlation even in presence of external stimuli. The rationale underlying this choice is that community structure of a group of healthy subject is expected to be highly consistent in presence of the same task.

3.2 Data

3.2.1 Subjects

50 healthy subjects (age: $mean = 25$, standard deviation $SD = 6$; 24 females) were included in this study. All of them were evaluated using the Non-Patient Structured Clinical Interview for DSM-IV [89] to exclude any psychiatric condition. Other exclusion criteria were: a significant history of drug or alcohol abuse, active drug abuse in the previous year, experience of a head trauma with loss of consciousness and any other significant medical condition. Socio-economic status (Hollingshead Four Factor Index, [90]), handedness (Edinburgh Inventory) [91] and total IQ (WAIS-R [92]) were also measured (see Table 3.1). The present study was approved by the local ethics committee (Comitato Etico Locale Indipendente Azienda Ospedaliera "Ospedale Policlinico Consorziale" Bari). Written informed consent was obtained by all participants after a complete description of the procedures, in accordance with the Helsinki Declaration.

Table 3.1 Demographic data of the healthy cohort (mean $\pm$ standard deviation).

Demographic Data	
Age (years)	25 ± 6
Gender (M/F)	$26/24$
Handedness	0.60 ± 0.55
Socio-economic status	39 ± 17
IQ	114 ± 4

3.2.2 fMRI Task

Participants performed the N-Back working memory task, in which a sequence of stimuli is presented and the subject has to remember the stimulus from "N" steps earlier. The stimuli consisted of numbers (1-4) presented in random sequence and displayed at the points of a diamond-shaped box. The control condition (0-back) simply required the subjects to identify the current stimulus. In the working memory condition, the task required the collection of a stimulus seen two stimuli earlier (2-Back). The task was organized in a block design, consisting of eight alternating 0-back and 2-back conditions, each lasting 30 seconds. Each 30 sec. block includes 14 n-back trials with an inter-stimuli interval of 2000 ms. Each run lasted 4 minutes and 8 seconds, from which dummy scans were acquired and discarded, obtaining 120 volumes.

3.2.3 fMRI Data

Echo planar imaging blood oxygenation level dependent fMRI data were acquired on a GE Signa 3T scanner (GE Healthcare) equipped with a standard quadrature head coil. A gradient-echo planar imaging sequence (repetition time, 2000 ms; echo time, 30 ms; thickness, 4 mm; gap, 1 mm; flip angle, 90°; field of view, 24 cm; and matrix, 64×64) was used to acquire images while the subjects performed the tasks.

Images were pre-processed using Statistical Parametric Mapping 8 software (SPM8; http://www.fil.ion.ucl.ac.uk/spm). Images were realigned to the first volume in the time series to correct for head motion (< 2 mm translation, $< 1°$ rotation), re-sampled to a 2 mm isotropic voxel size, spatially normalized into a standard stereotactic space (Montreal Neurological Institute template) using a 12 parameter nonlinear warping and smoothed to minimize noise and residual differences in gyral anatomy with a Gaussian filter, set at 6 mm full-width at half-maximum.

3.3 Algorithms

3.3.1 Network construction

The brain volume of each subject was divided in 246 non-overlapping anatomical regions of interest according to the Brainnetome Atlas [93]. Thirty regions from the most ventral part of the brain not acquired during scans were discarded and are not included in the following analysis. For each of the 216 remaining ROIs, a single time series was extracted by averaging the fMRI time series over all the voxels within the ROI. The time series were high-pass filtered (cutoff frequency $1/128s$). For each subject, functional connectivity between all pairwise combinations of ROI time series was assessed:

- by calculating their Pearson's correlation coefficient;
- by computing their CRP and then by calculating their synchronization index (SYNC) as described in the following subsection.

Finally, for each subject, two undirected weighted networks were identified, whose edges resulted from:

1. the signed pairwise Pearson's correlation coefficients;
2. the SYNC indexes.

3.3.2 Synchronization index

A state of a system is defined by the values of the variables that describe it at a given time. When such system evolves in time, the sequence of all its states forms a trajectory in the phase space, i.e., a multidimensional space whose dimension depends on the number of the variables of the system. Starting from different initial conditions, a real physical dissipative system tends to evolve in similar ways, such that its trajectories converge in a region of the phase space called attractor which represents the steady-state behavior of the system [13].

In experimental contexts, where the time series $\{u_i\}_{i=1}^{N}$ obtained from the sampling of a single observable variable, is available, it is possible to reconstruct the phase space of the system under investigation by means of the Takens's Theorem [94]. Accordingly, a state in the reconstructed phase space is given by a m-dimensional time delay embedded vector obtained from time delayed versions of the output signals as:

$$\vec{x}_i = \left(u_i, u_{i+\tau}, \ldots, u_{i+(m-1)\tau}\right) \tag{3.1}$$

where m is the embedding dimension end τ is the time delay.

Both parameters have to be properly selected to avoid redundancy in the phase space. The dimension m of the reconstructed phase space should be large enough to preserve the properties of the dynamical system ($m \geq 2D+1$, where D is the correlation dimension of the original phase space). The correct time delay τ should be chosen by determining when the samples of the time series are independent enough to be useful as coordinates of the time delayed vectors. For the estimation of the embedding parameters m and τ several techniques have been proposed. As an example, the first local minimum of average mutual information algorithm [95] can be used to select the proper time delay. The minimum embedding dimension is usually estimated through the false nearest-neighbors (FNN) algorithm [96].

The trajectories of two distinct systems with the same embedding parameters can be compared in a CRP [86], a matrix whose entries include information on the degree of closeness of each state of the first system with each state of the second system. In detail, for two systems with trajectories respectively $\vec{x}_i$ $(i = 1, ..., N)$ and $\vec{y}_j$ $(j = 1, ..., N)$, the CRP is defined as:

$$CR_{i,j}(\varepsilon) = \Theta\left(\varepsilon - ||\vec{x}_i - \vec{y}_j||\right) \tag{3.2}$$

where Θ is the Heaviside function, ε is a threshold for closeness, N is the number of considered states for each system and $||\cdot||$ a norm function. A generic entry $CR_{i,j}$ in the resulting $N \times N$ array is set to one if the distance between the points $\vec{x}_i$ and $\vec{y}_j$ is smaller than the threshold ε or to zero elsewhere.

The value of the parameter ε must be estimated carefully, as it influences the creation of structures in the plot. The selection of an appropriate value for the threshold ε can be made by taking into account the influence of the observational noise that could affect the experimental measures and the minimum distance between the trajectories of the two systems. In general, choosing ε equal to few percent of the maximum phase space diameter, could ensure a sufficient number of structures in the cross recurrence plot [97], while the appearance of artifacts could be avoided by considering the signal to noise ratio for the underlying physical systems [98].

A CRP exhibits characteristic patterns that show local time relationships of the segments of the trajectories of the two interacting systems. Typical structures

include single dots, diagonal lines and vertical and horizontal lines. Diagonal lines occur when the evolution of the states is similar at different times and their lengths are related to the periods during which the two systems move in similar ways remaining close to each other [99]. A CRP can also exhibit the main diagonal known as line of synchronization (LOS) . The presence of LOS implies the identity of the states of the two systems in the same time intervals, i.e. the (i,i) states, so its structure can be analyzed to extract information about the synchronization of the two time series [100]. In particular, the presence of LOS suggests that the two time series are fully synchronized, while discontinuities appear when the two signals do not have the same frequency and the same phase. Hence, the *synchronization time (SYNC)* has been defined as a metric to quantify the mean period during which the two systems are synchronized in order to reflect the dynamical synchronization behavior of the series throughout the observation period. *SYNC* is proportional to the ratio of the sum of the lengths of the subsegments l_j along the LOS to the total number of samples N:

$$SYNC = \frac{1}{N} \frac{\sum_{j=1}^{N_d} l_j}{N_d} \tag{3.3}$$

where N_d is the total number of subsegments.

For a visual reference see Figure 3.1. In Figure 3.1A two fMRI unsynchronized time series are compared and in Figure 3.1B are shown two fully synchronized fMRI time series. It is worth noting that in the first case there are discontinuities of LOS, while in the second case the LOS is continuous. Their SYNC values are respectively 0.05 and 1.

3.3.3 Modularity detection

Several community detection methods have been proposed to find an optimum partition of the nodes into non-overlapped communities, i.e. clusters of nodes that are more densely connected to each other than to other nodes in the network [101–103]. All these methods aim at maximizing a modularity metric that evaluates the quality of a partition by comparing the density of connections within a community to that expected in a random network. Here, the Louvain algorithm [103] has been used to find communities of ROIs in the two functional networks obtaining two partitions for each subject. The Louvain method is divided in two phases that are repeated iteratively. The first step favors local optimizations of modularity, while during the second step the communities

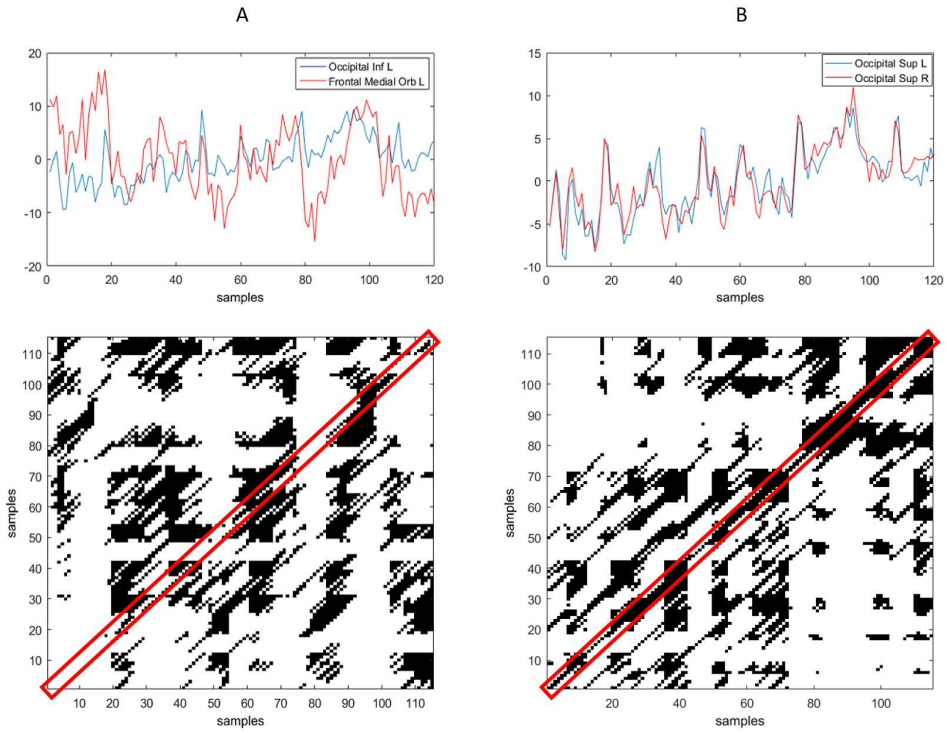

Fig. 3.1 Pairs of fMRI time series and their CRPs for A) Occipital Inferior L and Frontal Medial Orbital L (SYNC=0.05); B) Occipital Superior L and Occipital Superior R (SYNC=1).

found in the first step define a new coarse-grained network to be evaluated. This algorithm was chosen because it is fast and seems to be less affected by the resolution limit problem (i.e. the capability to detect modules smaller than a certain size) thanks to its multi-level nature. This method optimizes the modularity function defined as:

$$Q = \frac{1}{2m} \sum_{i,j} \left[A_{i,j} - \frac{k_i k_j}{2m} \right] \delta(c_i, c_j) \tag{3.4}$$

where $A_{i,j}$ is the link between nodes i and j, k_i is the sum of the weights of the links attached to node i, c_i is the community assigned to the node i, m is the sum of all of the links of the networks and δ is the δ function.

3.3.4 Statistical analysis of modularity

A statistical framework was adopted in order to compare the partitions of all the subjects for each functional network [104].

The normalized mutual information (NMI) [105] was used to assess the similarity between a couple of community partitions. For two networks with partitions respectively A and B, it is defined as:

$$NMI(A,B) = 2\frac{I(A,B)}{[H(A)+H(B)]} \tag{3.5}$$

where $I(A,B)$ is the mutual information between the two partitions, $H(A)$ and $H(B)$ are the entropy of A and B. This metric ranges between zero (if A and B are completely independent) and one (if A and B are identical).

The statistical relevance of the within-group community structure similarity was evaluated through a permutation test. First, a randomly rewired version of each functional network was generated preserving weights, density and degree sequence, resulting in two groups of networks: the actual and its randomized matching network. Then, the NMI was calculated between all the possible pairs of network partitions within each group. A null distribution was generated by randomizing group labels 10000 times and by calculating the the permuted within-group mean NMI at each permutation. Finally, a p-value was assigned as the number of times that the permuted within-group mean-similarity was greater than the actual within-group similarity, divided by the number of permutations.

In order to inspect the consistency of node assignments to specific functional communities, further analyses on the networks were carried out. Since the labels of modules are arbitrarily assigned by the community detection algorithm at each iteration, it is necessary to match the partition values across the subjects for visualizing the group level community structure. This problem can be overcome by finding a template partition as a reference and by reassigning the labels of communities to match the template, while preserving the distinctions between different modules in each partition [104]. In this algorithm, the partitions of each network for both metrics were matched to the most representative network partition of the group, i.e. the median determined by pairwise NMI. Once the labels of partitions are reassigned, it is possible to assess the within group consistency of each ROI in community membership by counting the number of occurrences with which a ROI appears with a particular label.

3.4 Results

3.4.1 CRP parameters

A subset of 5000 BOLD time series from the whole dataset were randomly selected and the FNN algorithm was applied for estimating the embedding dimension and the first local minimum of the averaged mutual information for selecting the proper time delay. The following results were obtained: $m = 5.2 \pm 0.75$ and $\tau = 1.4 \pm 0.66$, so the embedding parameters were set to $m = 6$ and $\tau = 1$. Following the criteria reported in [97] and [98], the range $[1.2 - 1.8]$ were identified for the threshold ε. The analysis was carried out with the average value of the range, setting $\varepsilon = 1.5$.

3.4.2 Statistical analysis of modularity

Permutation tests reveal significant differences of modularity structures between all the functional networks and their randomly rewired versions ($p = 0$ for both the couples), indicating different modular decompositions compared to the null models. However, as shown in Figure 3.2a, the Pearson's networks, exhibit within-group NMI values much lower than those obtained by means of the SYNC metric (see Table 3.2 for mean, median and interquartile range quantities). The nonparametric Wilcoxon rank sum test confirmed significant differences between NMI values of SYNC and those of the Pearson's metric (p-value $p = 3.04\dot{1}0^{-87}$, $\alpha = 0.05$). The range of NMI values of SYNC networks are also comparable to those found among control healthy subjects in resting studies at different threshold values of network density [104]. These results suggest that the functional networks constructed with the SYNC metric share more modularity structures than the Pearson's networks and exhibit also a higher signal-to-noise ratio.

Table 3.2 Mean; median (interquartile range) quantities of NMI and Q distributions for the metrics Synchronization and Pearson's correlation.

Distributions	NMI	Q
Synchronization	0.24;0.23 (0.11)	0.17;0.17 (0.04)
Pearson	0.15;0.14 (0.15)	0.11;0.11 (0.07)

In addition, the modularity index Q was evaluated. This index ranges between 0 and 1 and measures the density of links inside communities as compared to links between communities. As shown in Figure 3.2b, the two

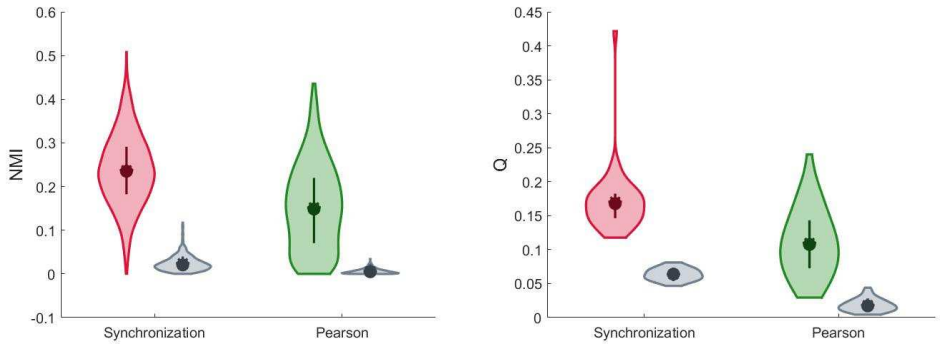

(a) (b)

Fig. 3.2 Violin plots of a) within-group NMI distributions and b) Q distributions for Synchronization and Pearson's correlation connectivity metrics with their randomized matching networks (in gray).

distributions are significantly different from their random versions (permutation tests: p=0 for both pairings) and the modularity index of the networks obtained with the SYNC metric is higher than that of the Pearson's networks (p-value resulting from the nonparametric Wilcoxon rank sum test $p = 3.52 \cdot 10^{-8}$, $\alpha = 0.05$).

3.4.3 Comparison of modular partitions in SYNC and Pearson's networks

Since connectivity measures were computed on a time series derived from a working memory task, it was expected to find modules related to working memory performance involving the fronto-parietal network [106] to motor activity related with the 0-back task [107], and to the default mode network, which is deactived when performing the task [108]. Figure 3.3 shows the five modules detected by the Louvain algorithm at group level. The first module includes areas critical for visuo-spatial memory and closely resembles the classical fronto-parietal network. In contrast, the second module includes more medial regions, with nodes belonging both to the anterior and the posterior default mode networks [109, 110]. The third module overlaps widely with the sensory-motor network, including pre- and post-central nodes but also areas of the temporal lobe involved in auditory perception. Interestingly, the fourth and fifth module map almost exclusively to subcortical regions, including the dorsal basal ganglia and the thalamus with the ventral striatum, respectively.

These regions are involved in working memory performance [111, 112], but it is intriguing to notice that the technique here employed parsed the connectivity of cortical and subcortical regions based on the time series of activations, yielding anatomic information just based on functional activity patterns. Figure 3.4 shows the two communities identified at group level for the Pearson's networks. The first module comprises most of the ROIs mapped in the first community of the SYNC networks, while the rest of the ROIs are included in the second module.

The consistency of the assignment of brain regions to functional modules for the SYNC networks is shown in Figure 3.5. As it can been seen, all the ROIs within the fronto-parietal network are the most consistent among the subjects; in contrast, some nodes from the medial temporal lobes, insular gyrus and globus pallidus are assigned less uniformly to the same community across the subjects. These findings are in line with the crucial involvement of the frontal parietal network in working memory processing [113]. As this map resembles closely an activity group map, these findings highlight that the connectivity assessment developed is sensitive to the functional role of the modules identified. Overall, the network parsing obtained by the novel technique reveals a pattern of coupling between brain regions consistent with known models of activation and deactivation during task performance. In Figure 3.6 is shown the within group consistency of each ROI in community membership for Pearson's networks. Although the overall consistency seems generally higher due to the lower number of communities (two versus five), a direct comparison with the SYNC networks is possible only for the first module. The one-sided hypothesis Wilcoxon rank sum test confirmed a greater consistency of the ROIs within the first module for the SYNC matrices (median values of consistency: $m_{sync} = 85.5$, $m_{pearson} = 82$, $p = 0.0096$, $\alpha = 0.05$) proving a better identification of the fronto-parietal network across the subjects in such matrices.

3.5 Discussion

In the current study, a modularity analysis is applied to networks defined with both the proposed SYNC index and the Pearson's correlation coefficient in order to investigate the task-related functional organization of the brain. Modularity is implicitly related to significant self-regulating mechanisms of the human brain: efficient dense within module processing and sparse fast integration among

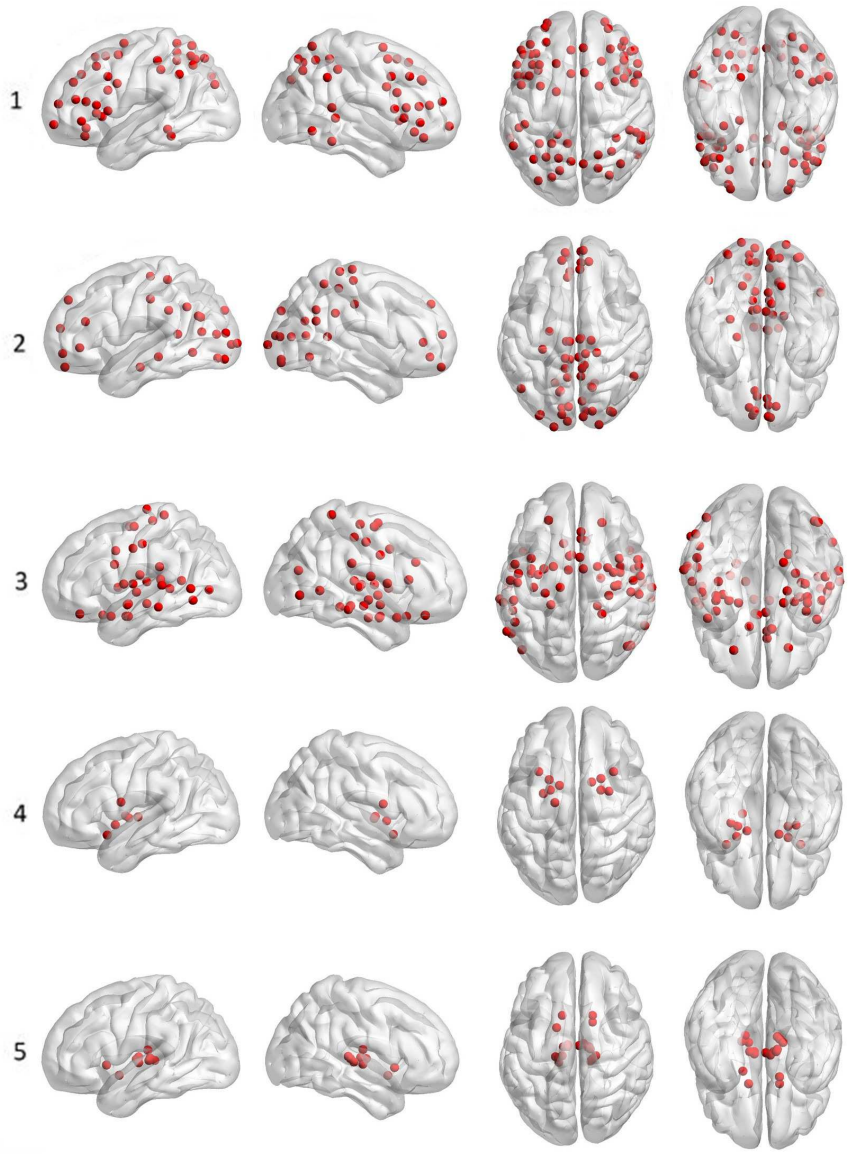

Fig. 3.3 The five group level functional communities detected in SYNC networks. In each row, a single community is shown in four brain views (left side, right side, top side and bottom side).

sub-systems reduce noise propagation and latency [114]. Thus, this feature is strictly connected to critical functional organization between brain systems that are specialized to carry out different tasks: modularity is expected to be greater for optimal system organizations, while decreased modularity implies that there are less intra-modular edges than inter-modular edges [3]. A low level of modularity would not be compatible with a fast adaptation of the human brain in response to external stimuli. Indeed, lack of highly specialized modules may not allow a rapid execution of complex cognitive task [3, 115]. Consistently, a

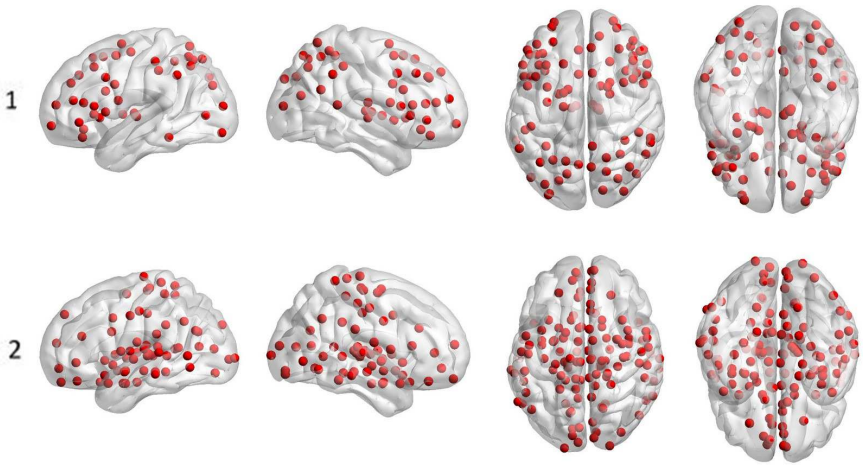

Fig. 3.4 The two group level functional communities detected in Pearson's networks. In each row, a single community is shown in four brain views (left side, right side, top side and bottom side).

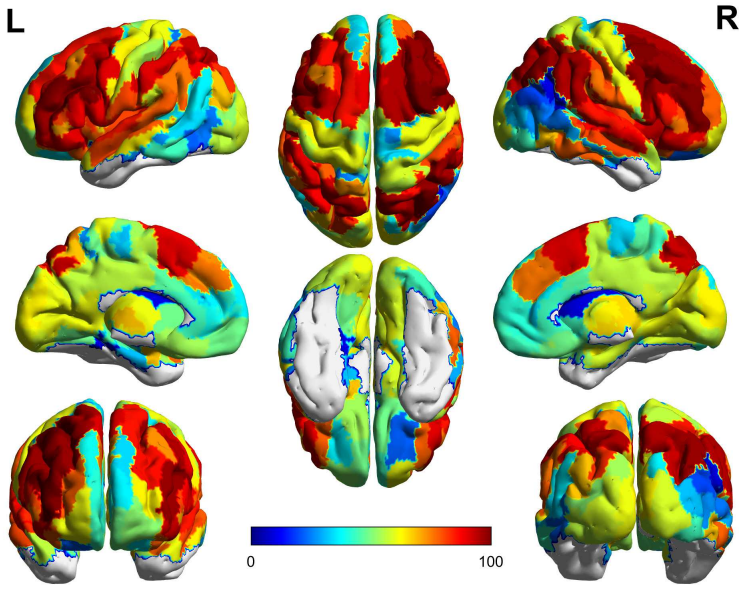

Fig. 3.5 Consistency of the assignment of brain regions to modules measured as the frequency of occurrence of the node with a specific label (in percent) for SYNC networks.

decreased modularity has been associated with brain disorders characterized by abnormal cognitive processing and has been found as a marker of abnormal brain network development [116–118]. Moreover, there is evidence that, while the adaptation speed of the functional organization of the brain is not critical among healthy individuals that perform a specific task, modularity is stable across time, suggesting the existence of latent specific task-related modular

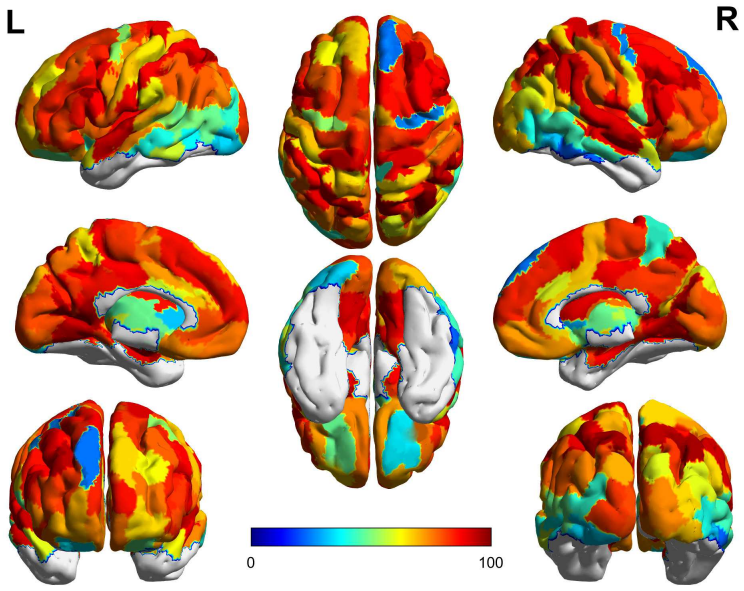

Fig. 3.6 Consistency of the assignment of brain regions to modules measured as the frequency of occurrence of the node with a specific label (in percent) for Pearson's networks.

configurations [70, 87]. The statistical analysis of modularity reveals that a greater structure homogeneity and a higher number of functional communities activated during the working memory task seem to be better identified in SYNC networks, while the Pearson's correlation does not reflect such features expected in a healthy population. In detail, the SYNC networks showed both higher NMI and Q values thus indicating that the extracted modular partitions are more similar to each other across the population and exhibit a clearer division into communities. Indeed the modularity index Q statistically quantifies the goodness of a hard partition as its value is related to the difference between the within-module interactions and the between-module interactions [72]. Furthermore, the consistency analysis in which the partitions of each subject is compared with the median partition of the population, points out two results: (i) both networks show at the group level a similar first community that resembles the fronto-parietal network, but in the SYNC networks other modules that map to systems engaged during working memory performance are detected; (ii) the statistical comparison of the ROIs within the first module highlight a greater consistency of such task-related regions in SYNC networks. These findings suggest that a problem of community resolution is evident in Pearson's networks, whereas all the regions not included in the first module, are identified in a single community without distinction among sensory-motor network, default mode network and

subcortical areas and that even the fronto-parietal network is identified more weakly across the population.

In this framework, the same community detection algorithm was applied to both kinds of networks. Since the algorithm generates a node partition of a connectivity matrix, some properties of the index used to identify the network such as sensitivity to noise and to complex interaction mechanisms occurring among the brain regions, could affect the degree of partition of the network into communities. Several brain connectivity metrics have been proposed as alternatives to Pearson's correlation coefficient. Coherence and partial coherence analysis were applied to fMRI data to extend linear metrics of zero-lag correlation. These spectral measures estimate the linear time-invariant relationship between time series by using phase and magnitude information for all the time lags [80]. Both coherence and partial coherence were proved effective in overcoming an important limitation of the zero-lag correlation, i.e., its sensitivity to the shape of the regional haemodynamic response function that could results in spurious correlations of the underlying neural activity. In the last two decades, there has been a growing interest in developing new connectivity metrics sensitive to both linear and nonlinear interactions in human brain. In fact, the spatiotemporal nonlinearity was shown to be an important feature of the BOLD signal that should be considered to properly characterize the complex interactions between brain regions. In [119] a phase space multivariate approach was adopted to investigate the nonlinear properties of resting state fMRI data. The dynamics of the signals were reconstructed by using the time-delay embedding of some principal components of the fMRI data and the correlation dimension and the spatiotemporal Lyapunov exponents were calculated to assess the nonlinear fractal property and the chaotic dynamic behavior of the signals. A surrogate data test confirmed an inherent deterministic nonlinear behavior in fMRI fluctuations. Other methods for exploring the dynamic behavior of physiological signals have been proposed. Recurrence plots and recurrence quantitative analysis of the structures therein contained were used to examine the recurrence properties of dynamic systems [99]. As an example, in [120] RQA was employed as a univariate data-driven technique to quantify recurrent patterns in fMRI data. This technique involves the projection of each time series in the phase space from which a recurrence plot is obtained. Several numerical descriptors are then used to quantify recurrent patterns in each time series. This method has been developed as an alternative to general linear model and probabilistic independent component analysis in activation studies.

The underlying idea is that single-voxel signals become more regular in response to a stimulus, so RQA can detect the most active voxels without any model assumption. Recurrence plots and RQA were proved successful in analysing very noisy and nonstationary signals. These methods offer a set of metrics able to capture comprehensively the dynamic behavior of a system in the phase space. Some studies confirmed their effectiveness also for the analysis of EEG and MEG data, particularly for detecting functional anomalies in several diseases [15, 121–123]. Cross recurrence plots are bivariate extensions of the recurrence plots, that consist in two-dimensional matrices showing the interactions of pairs of signals in the phase space. The proposed index, extracted from the CRP, represents an intuitively interpretable generalized dynamic synchronization metric that could be used to extend the set of known RQA measures.

3.6 Summary

In this Chapter, a new synchronization-based metric is proposed to assess functional connectivity in human brain. The metric is a generalized synchronization measure that takes into account both the amplitude and phase coupling between pairs of fMRI series. This method differs from the correlation measures used in the literature, as it is more sensitive to nonlinear coupling phenomena between time series and it is more robust against the physiological noise. In order to probe these latter two aspects, a modularity analysis of task-related fMRI networks of a cohort of healthy subjects built with the new proposed metric was performed. The aim was to verify whether the new metric was able to return networks whose functional modules were coherent with the actual organization of the brain regions during the task-based activity.

Here, unthresholded complete connectivity matrices were considered to test the effectiveness of the synchronization against noise and spurious correlations. Indeed unthresholded networks have lower signal-to-noise ratio as the most important links do not stand out among all the weights. By comparing the networks constructed by means of the proposed metric with those obtained through the Pearson's coefficient, it seems that the synchronization metric better reflects the task-related network structure for number of detected communities, for the functional organization of the ROIs and for greater consistency of communities across the subjects.

Chapter 4

A multidimensional phase-space approach

4.1 Cross Recurrence Quantitative Analysis

In Chapter 3, an efficient way to explore the dynamic behavior of the trajectories of interacting systems in phase space has been described. Besides the proposed synchronization metric, several complex metrics exist to perform a formal quantification of graphical patterns of RPs and CRPs that have been proven to be useful in a great variety of context [124, 125]. RQA is a model-free analysis that includes a set of indices, each related to specific complex phenomena occurring in phase space. Hence, its application to brain signal analysis could reveal changing dynamics, critical events and distinctive features of cognitive states and diseases.

In this chapter, a framework based on both CRPs and graph analysis aimed at capturing dynamic changes of functional connectivity and providing straightforward markers of the dynamic states in brain activity to characterize pathological conditions in a clinical context is presented. The principal idea underlying this analysis is that if each RQA metric is representative of a dynamic phenomenon in the phase space, a multivariate model that uses simultaneously all the measurements extracted from the CRP, could describe more completely the dynamic behavior of the interacting systems. The fMRI data of a cohort of subjects including normal controls and schizophrenic patients acquired during a simple executive condition and a working memory task, were used to verify whether the new markers could reflect different cognitive loads and detect differences between the groups of subjects.

4.2 Data

4.2.1 Subjects

127 healthy subjects (age: *mean* = 26, standard deviation *SD* = 7; 61 females) and and 127 subjects suffering from schizophrenia (age: *mean* = 31, standard deviation *SD* = 7; 47 females) were included in this study. Control subjects were evaluated using the Non-Patient Structured Clinical Interview for DSM-IV [89] to exclude any psychiatric condition. Other exclusion criteria were: a significant history of drug or alcohol abuse, active drug abuse in the previous year, experience of a head trauma with loss of consciousness and any other significant medical condition. The present study was approved by the local ethics committee (Comitato Etico Locale Indipendente Azienda Ospedaliera "Ospedale Policlinico Consorziale" Bari). Written informed consent was obtained by all participants after a complete description of the procedures, in accordance with the Helsinki Declaration.

4.2.2 fMRI task and data

Participants performed both the 2-Back working memory task, and 0-back task as described in Section 3.2.2. The 0-back task was organized in a block design, consisting of eight alternating 0-back and resting conditions, each lasting 30 seconds. fMRI data were preprocessed as described in Section 3.2.3.

4.3 The general framework

The general framework is shown in Figure 4.1. Each step is described in the following sections.

4.3.1 Multi-recurrence layers construction

The brain volume of each subject was divided in 120 non-overlapping anatomical regions of interest according to the AAL Atlas [37]. Sixteen regions from the most ventral part of the brain not acquired during scans were discarded and are not included in the following analysis. For each of the 100 remaining ROIs, a single time series was extracted by averaging the fMRI time series over all the voxels within the ROI. The time series were high-pass filtered (cutoff frequency

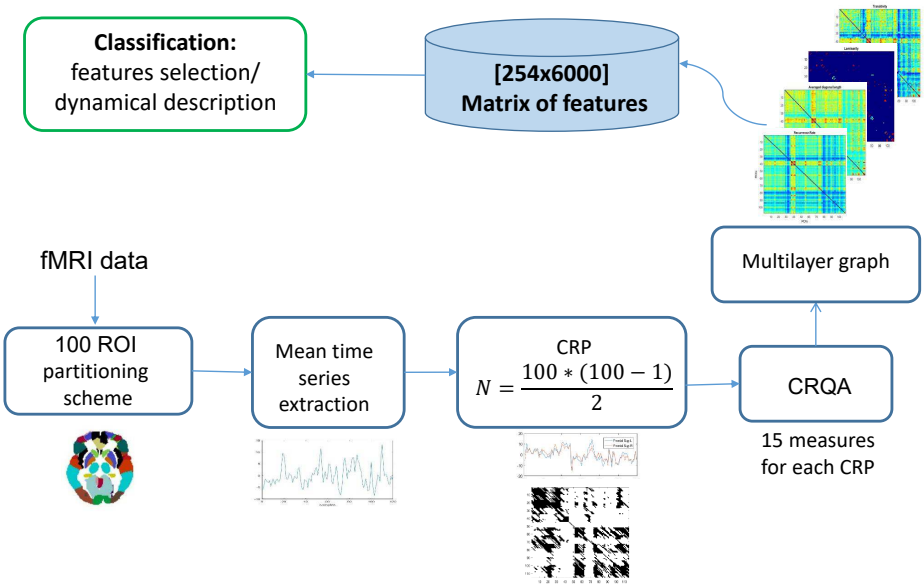

Fig. 4.1 Multi-recurrence dynamic framework.

$1/128s$). For each subject, functional connectivity between all pairwise combinations of ROI time series was assessed by computing their CRP and then by calculating the 15 RQA metrics as described in the following subsection resulting in 15 connectivity matrices. A tensor structure with 15 undirected weighted networks as layers is finally composed of all the 15 connectivity matrices. Strength, betweenness, clustering coefficient and pagerank centrality have been extracted from each layer and for each node of the network, resulting in a 254×6000 matrix, in which each feature is labelled as: *rqa layer - graph metric - roi* according to the layer from which it belongs, the graph metric and the node (ROI) of the network.

4.3.2 RQA metrics

As already mentioned in the previous chapter, the graphical patterns of a CRP are related to similarities and differences between the dynamic evolutions of the couple of systems under investigation. Single, isolated recurrence points indicate rare states that can appear due to noise. Diagonal lines occur when the evolution of the states is similar at different times. Vertical and horizontal black lines mark time periods in which the sequence of states change very slowly or

do not change at all, while vertical and horizontal white bands result from states which occur rarely.

The analytical evaluation of the geometric structures of the CRPs involves a set of complex measures, mostly based on the distribution of the lengths of the diagonal and vertical/horizontal lines in the plot [126, 99].

In this thesis, five major classes of measures defined as follows are considered:

1. Recurrence density - based measures. The simplest measure is the *recurrence rate* (RR) , a generalization of the cross correlation sum:

$$RR = \frac{1}{N^2} \sum_{i,j=1}^{N} CR_{i,j} \tag{4.1}$$

2. Measures based on the distribution $P(l)$ of lengths l of the diagonal lines. Among these:

   - the *determinism* (DET) is the ratio of the recurrence points that form diagonal structures to all points:

$$DET = \frac{\sum_{l=l_{min}}^{N} lP(l)}{\sum_{l=1}^{N} lP(l)} \tag{4.2}$$

   - The *average diagonal line length* (ADL) is the average time in which two segments of the trajectory move close together:

$$ADL = \frac{\sum_{l=l_{min}}^{N} lP(l)}{\sum_{l=1}^{N} P(l)} \tag{4.3}$$

   - The *length of the longest diagonal line* (LLD) found in the CRP is related to maximal time period in which the two systems are synchronized:

$$LLD = \left(\{l_i\}_{i=1}^{N_l}\right), \tag{4.4}$$

     where N_l is the total number of diagonal lines.

   - The *entropy of diagonal length* (EDL) shows the complexity of the diagonal lines in a CRP. It is the Shannon entropy of the probability

$p(l)$ to find a diagonal line of length l in the plot:

$$EDL = -\sum_{l=l_{min}}^{N} p(l)\ln p(l) \tag{4.5}$$

3. Measures based on the distribution $P(v)$ of vertical line lengths v. This distribution is used to quantify laminar phases during which the states of the systems change very slowly.

   - The ratio of recurrence points forming vertical structures to all recurrence points of the CRP is called *laminarity* (LAM) :

   $$LAM = \frac{\sum_{v=v_{min}}^{N} vP(v)}{\sum_{l=1}^{N} vP(v)} \tag{4.6}$$

   where N_v is the total number of diagonal lines.

   - The *average length of vertical lines* (TT) is the trapping time and represents the average time in which the systems are trapped into a specific state:

   $$TT = \frac{\sum_{v=v_{min}}^{N} vP(v)}{\sum_{v=1}^{N} P(v)} \tag{4.7}$$

   - The *length of the longest vertical line* (LLV) is analogous to *LLD* for the vertical lines:

   $$LLV = \left(\{v_l\}_{l=1}^{N_v}\right) \tag{4.8}$$

   - From a CRP it is possible to extrapolate the *recurrence times*. Let's consider the recurrence points of the ith row $\left\{CR_{i,j}\right\}_{j=1}^{N}$ which correspond to the set of points of the trajectory which fall into the ε-neighborhood of an arbitrary chosen point at i. The recurrence times between these recurrence points (*recurrence times of first type*) are:

   $$\{RT1_k = j_{k+1} - j_k\}_{k\in\mathbb{N}} \tag{4.9}$$

   Removing all consecutive recurrence points with $RT1_k = 1$ to avoid tangential motion the *recurrence times of second type* are:

   $$\left\{RT2_k = j'_{k+1} - j'_k\right\}_{k\in\mathbb{N}} \tag{4.10}$$

where the set of the remaining recurrence points is used. It turns out that $RT2$ measures the time distance between the beginning of subsequent recurrence structures in the CRP along the vertical direction and it can be considered as an estimate of the average of the lengths of white vertical lines in a column of the plot.

- The *normalized entropy of the recurrence time distribution (RPDE)* of the time series $P(t)$ is defined as:

$$RPDE = -(lnT_{max})^{-1} \sum_{t=1}^{T_{max}} P(t) lnP(t) \tag{4.11}$$

where T_{max} is the largest recurrence value.

4. Recurrence network - based measures. A CRP can be interpreted as the adjacency matrix of a graph $G(V,E)$, whose links E connect the set of vertices V that represent neighbor points in phase space. Topological properties of recurrence networks have been related to statistical properties of the phase space density, revealing further complex dynamical aspects of time series. In particular, some network-based metrics have been associated with invariant characteristics of phase space, i.e., independent from a particular embedding [127].

    - The *transitivity (TRANS)* of a CRP is defined as the ratio of the number of close triangles λ_G to the number of subgraphs with 2 edges and 3 vertices τ_G in the network:

$$TRANS = \frac{3\lambda_G}{\tau_G} \tag{4.12}$$

    It can be seen as a quantitative measure of the geometric structural complexity of the trajectories in phase space [128].

5. LOS - based measures. In addition to the SYNC metric, other two metrics were defined to quantify the temporal synchronization behavior of the two systems. In detail:

- *Hard Synchronization (HARD SYNC)*, a binary response variable that gives information about the presence/absence of the LOS:

$$HARD\ SYNC = \begin{cases} 1, & \text{if } CR_{i,i} = 1, \forall i = 1, \ldots, N \\ 0, & \text{otherwise} \end{cases} \tag{4.13}$$

- The *entropy of LOS (ENTR LOS)* is the Shannon entropy of the probability $p(d)$ to find a subsegment of length d along the LOS and is an index of the complexity of the synchronization periods of the two time series:

$$ENTR\ LOS = -\sum_{d=1}^{N} p(d) \ln p(d) \tag{4.14}$$

4.3.3 The statistical framework

A statistical framework was developed in order to select only the most significant features among the 6000 for the binary classification problem. As stated in Chapter 2, mass univariate hypothesis tests detect the cross-group differences by comparing each feature individually across the two populations. This technique is effective in describing the most important differences between two classes but has some limitations. The aim of the analysis is to identify the subset of features that maximally discriminates between the two classes, in order to both verify the presence of particular dynamic phenomena that characterize the two populations, and to build a model able to predict if a new subject belongs to one of the two classes. Hence, a multivariate machine learning approach has been integrated with some statistical techniques to ensure the stability of the performance values achieved by the model. Briefly, a Support Vector Machine (SVM) classifier was used to identify multivariate patterns of multi-recurrence connectivity related to the diagnostic groups. The 70% of the data were used as training set for training the model. This set was bootstrapped 200 times to perform a robust feature selection.The best subset in terms of classification performances was selected to train a final model which was tested on an independent test composed by the remaining 30% of the data. The main steps of the framework are shown in Figure 4.2 and are described in the following sections more in detail.

Feature Selection

Feature selection techniques are powerful tools that attempts to:

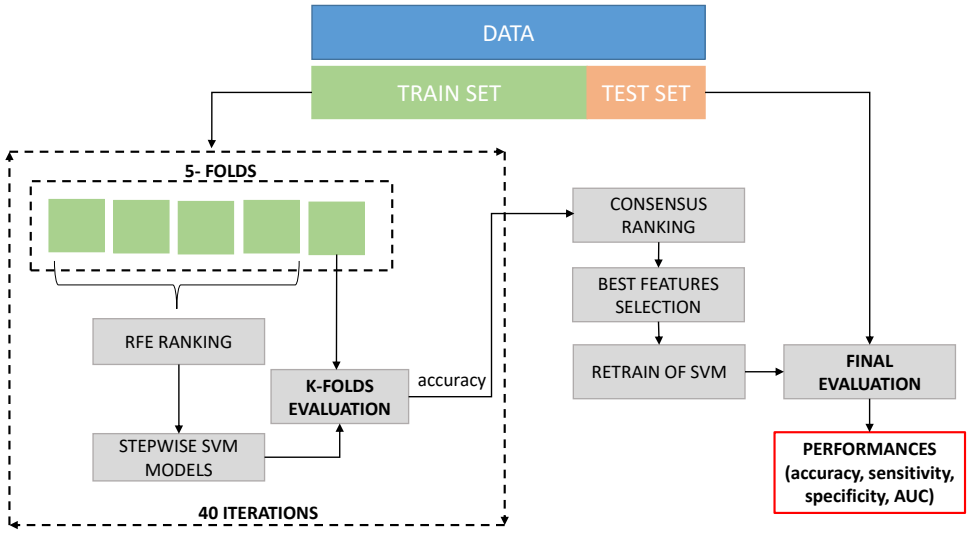

Fig. 4.2 Statistical framework to select the most discriminative features for both the experiments. A nested feature selection was performed on the training set in each round of the k-fold validation. Then 200 stepwise SVM models were trained by progressive increasing the training set size. A consensus ranking procedure was used to select the most stable features with the highest accuracy. At the end, a final model was tested on an independent test.

- removing irrelevant, noisy and redundant features, with the aim to avoid overfitting and improving classification performance;
- improving the computational complexity of the learning algorithm;
- providing a deeper insight into the data, highlighting which features are most informative for classification.

Feature selection algorithms are divided into three categories: filters, wrappers and embedded methods [129]. Filters evaluate each feature without interaction with classifiers by using several criteria related to correlations among features or amount of shared information. Wrappers find a feature subset that has the minimum cross-validation error on the training data, treating the classifier as a black box. Searching methods such as sequential forward selection and simulate annealing are examples of wrappers. Embedded methods incorporate variable selection as part of the training process.

In this thesis, Support Vector Machine-Recursive Feature Elimination (SVM-RFE) , which integrates in a single consistent framework both feature selection and pattern classification, was selected to perform feature selection. SVM-RFE is an embedded method, introduced by Guyon et al. [130] in the context of gene selection for cancer classification: gene redundancy was automatically eliminated and better gene subsets were obtained compared to state-of-the-art methods.

The main intuition of SVMs is to find a separating hyperplane with the largest possible margin on either side [131]. A particularity of the algorithm is that the weights w_i of the decision function $D(x)$ are a function of only a small subset of the training examples, called "support vectors". Given the training examples $\{x_1, x_2, \ldots, x_n\}$ and class labels $\{y_1, y_2, \ldots, y_n\}$, the following cost function is minimized over α_k:

$$J = \frac{1}{2} \sum_{hk} y_h y_k \alpha_h \alpha_k (x_h \cdot x_k + \lambda \delta_{hk}) - \sum_k \alpha_k \tag{4.15}$$

with $0 \leq \alpha_k \leq C$ and $\sum_k \alpha_k y_k = 0$. λ and C are positive constants ensuring that the problem has a solution in case the data are not linearly separable; δ_{hk} is the Kronecker symbol. The resulting decision function is:

$$D(x) = w \cdot x + b \tag{4.16}$$

where $w = \sum_k \alpha_k y_k x_k$ and $b = \langle y_k - w \cdot x_k \rangle_k$. The weight vector w is a linear combination of the training examples. Most weights α_k are zero. The training examples with non-zero weights are the support vectors.

Recursive feature elimination, in its broad sense:

1. train the classifier;
2. compute a ranking criterion for all features;
3. remove the feature with smallest ranking criterion, as it has the least effect on classification.

This process is iteratively computed until all the features have been removed. SVM-RFE is intimately related to the SVM model, as the ranking criterion for feature k is the square of the k-th element of w: $J(k) = w_k^2$. In particular, in this work, the SVM-RFE with correlation bias reduction, as proposed in [132], has been adopted. In the original formulation of SVM-RFE, one problem is not addressed: when some of the features are highly correlated, the assessing criteria of these features will be influenced, so their importance will be underestimated. The authors called this phenomenon “correlation bias”. When a subset of features is removed in one iteration of RFE, a group of correlated features may be removed entirely. This may happen either because the features are truly irrelevant, or because their ranking criteria have been incorrectly underestimated. In both conditions, the method proposed in [132] moves representative feature of the group back to the surviving feature list. In this way, the group can be evaluated again in the next iteration without the influence of the correlation bias. The group representative can be chosen as the feature with the highest criterion in this iteration. Therefore, this strategy does not change the candidate feature set or the ranking criterion, but monitors and corrects the potentially wrong decisions due to the correlation bias.

The output of SVM-RFE is a list of ranked features. Feature selection can be achieved by choosing a group of k_{opt} top-ranked features. Since k_{opt} is not known a priori, the RFE algorithm was performed in each fold of a cross-validation procedure. In this way, a nested feature selection was obtained since the ranking of the features is blind to the test set. This approach was chosen in order to avoid the "double dipping" problem. Indeed, performing the feature selection on the whole dataset could introduce bias in the final classification model. The dangerous effects of the double dipping have been widely described and result essentially in overestimating the values of accuracy

and area under the ROC curve (AUC) [133, 134] . In some neuroimaging studies different recommendations have been provided to avoid the bias introduced by this procedure [60, 135, 136].

In particular, here 40 re-sampling of a 5-fold cross-validation were executed producing 200 bootstraps of the train set. In each iteration, 4-folds of the original training set were input to RFE and then stepwise SVM models were trained for ranked subsets of increasing size (i.e., the top 10, 60 , 110 , and so on up to 6000 ranked features). Each stepwise model was tested on the left fold and the performances of each model were stored for successive evaluations.

Stability of the features

Some measures are usually employed to assess the predictive power of a classifier. Given the output statistics of a classifier in terms of true positives (TP) , true negatives (TN) , false positives (FP) and false negatives (FN) :

1. accuracy (ACC) is the proportion of true results (both true positives and true negatives) among the total number samples:

$$ACC = \frac{TP+TN}{TP+FP+TN+FN} \tag{4.17}$$

2. sensitivity or true positive rate (TPR) measures the proportion of positives that are correctly identified as samples of the positive class:

$$TPR = \frac{TP}{TP+FN} \tag{4.18}$$

3. specificity or true negative rate (TNR) is the proportion of negatives that are correctly identified as as samples of the negative class:

$$TNR = \frac{TN}{TN+FP} \tag{4.19}$$

4. the ROC curve of a classifier is created by plotting sensitivity against specificity at various threshold settings. Then the area under the ROC curve is equal to the probability that the classifier will rank a randomly chosen positive instance higher than a randomly chosen negative one:

$$AUC = \int_{-\infty}^{+\infty} TPR(T)(-TNR'(T))dT \tag{4.20}$$

Here, the number of features k_{opt} to be selected was chosen as the one yielding the highest accuracy of all the stepwise models. Since, in principle, the features of each subset corresponding to the top k_{opt} elements of each model can be different from each other, a consensus ranking algorithm was used to select the most common features across all the 200 models. To determine the stability of the selected subset of features, a null distribution of the performances was obtained by permuting class labels 200 times. The null distribution was compared with the actual distribution of the ACC values to determine whether the final SVM model outperformed the random model. Finally, all the performances of the final SVM model were computed.

4.4 Results

Figure 4.3 shows the mean values with standard errors of the accuracy of all the 200 stepwise SVMs models. The maximum values are 82.58 ± 0.78 for the 2-back experiment and 74.11 ± 0.97 for the 0-back experiment both for $k_{opt} = 210$.

Hence the top 210 features of the 200 models were selected for the stability analysis. Firstly, the final set of stable k_{opt} features were selected through the consensus ranking algorithm. Then, the null classifier distribution, created by permuting 200 times the labels of the subjects, was compared with the actual distribution of the ACC values by using Wilcoxon's rank sum test, resulting in $p < 0.001$ with $\alpha = 0.05$. Therefore, the models trained with the top k_{opt} features significantly outperformed the null models. The final classification performances on the independent test are reported in Table 4.1.

Since the multilayer recurrence model implicitly defines hierarchical features, it is possible to calculate global statistics, i.e., defined on a single hierarchical level of the features independently of the others, or local statistics, i.e., by selecting a sequence of the hierarchical levels (see Figure 4.4 for a visual reference example). In this chapter only global statistics are shown.

Here, the frequency of occurrence of the names of the layers across the features' labels are used to rank the layers at global level. Similarly, the occurrence frequency of the name of each graph metric across the k_{opt} features' labels are employed to rank the graph metrics.

The ranking of the layers are shown in Figure 4.4. Synchronization metrics (both HARD SYNC and SYNC) are among the top ranked layers for both the experiments (rates: 21.43% - 9.52% and 20.48% - 14.29% for the 2-back and

0-back, respectively). Other layers with rather high frequencies of occurrence across the features are LLV (10.95%) and EDL (9.05%) for the 2-back experiment and RT2 (15.71%) and LLD (12.86%). Conversely, ADL (1.90% - 0.48% for 2-back - 0-back), TT (2.38% - 0.48%) and RR (3.81% - 2.86%) are the layers least frequent across the selected features.

The ranking of the graph metrics are shown in Figure 4.6. In both the experiments the pagerank centrality is the most important metric, in the 2-back task, follow: betweenness (20%), strength (16.2%) and clustering (13.8%). In the 0-back task strength and clustering are comparable (22.86% and 20.95% respectively), while betweenness(14.76%) is the least important.

In order to select only the most significant ROIs among the features discriminating the two groups of subjects, another approach was adopted. For each ROI_i the following step were performed:

1. all the features with the ROI_i in the labels are removed;
2. 10000 permutations of the diagnosis labels (i.e., control and schizophrenic) are performed and the binary classification is performed for each permutation;
3. the average decrease accuracy is compared with the actual classification accuracy to obtain a p-value.

In Figure 4.8 is shown the slice view of the most significant ROIs for the 2-back task. Table 4.2 also reports the same regions with MNI coordinates and p-values. Figure 4.7 and Table 4.3 show the most significant ROIs and relative p-values for 0-back task.

Table 4.1 Performances of the classification of the final SVM on the independent test set.

Experiment	ACC (%)	TPR (%)	TNR (%)	AUC (%)
NC 02 - SZ 02	81.17 ± 0.19	82.77 ± 0.40	79.57 ± 0.36	88.60 ± 0.16
NC 0B - SZ 0B	74.89 ± 0.18	80.28 ± 0.49	69.51 ± 0.45	83.60 ± 0.18

4.5 Discussion

Schizophrenia is a severe psychiatric disease with clinical symptoms of thought disorders, loss of initiative, hallucinations, delusions, and in some cases cognitive dysfunctions involving sensory processing, cognition and working memory.

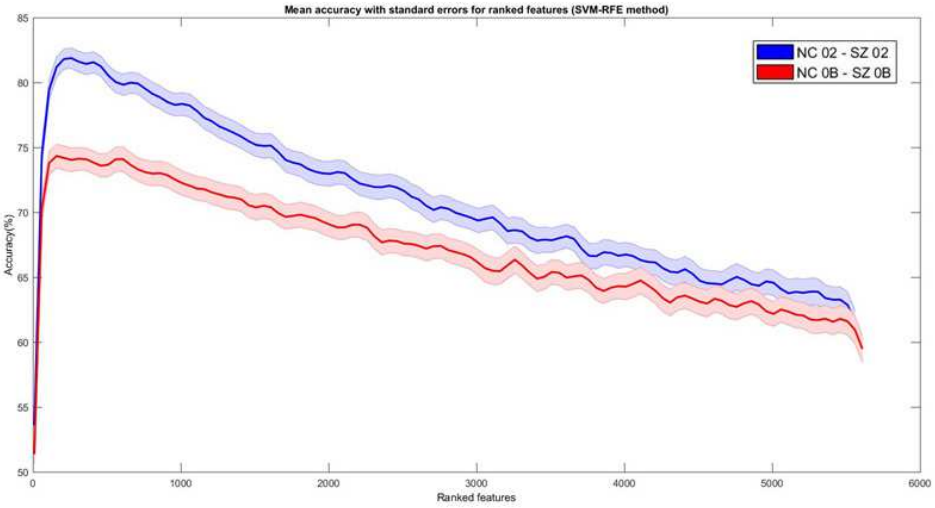

Fig. 4.3 Mean ACC values and standard errors of the stepwise SVMs obtained for ranked subsets of the features for both the experiments.

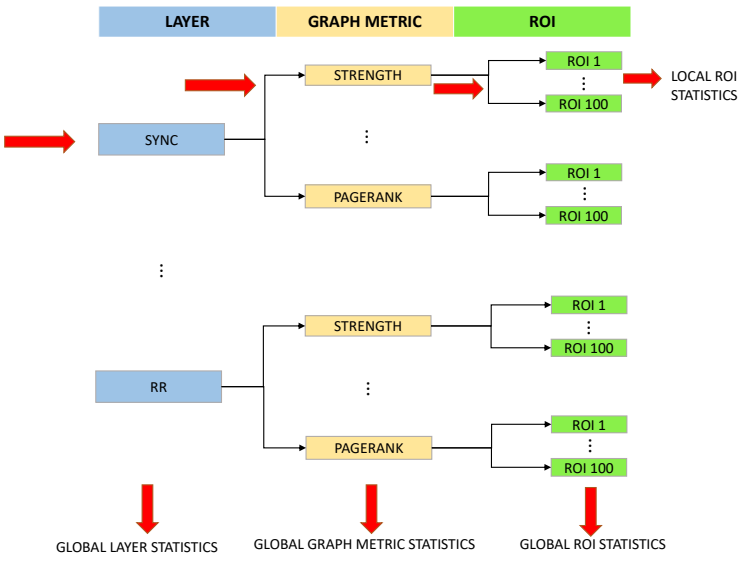

Fig. 4.4 Examples of features' statistics. The global statistics consider each layer of the hierarchy individually, while for local statics on the ROIs, a single layer of the multi-recurrence structure and a single graph metric must be selected.

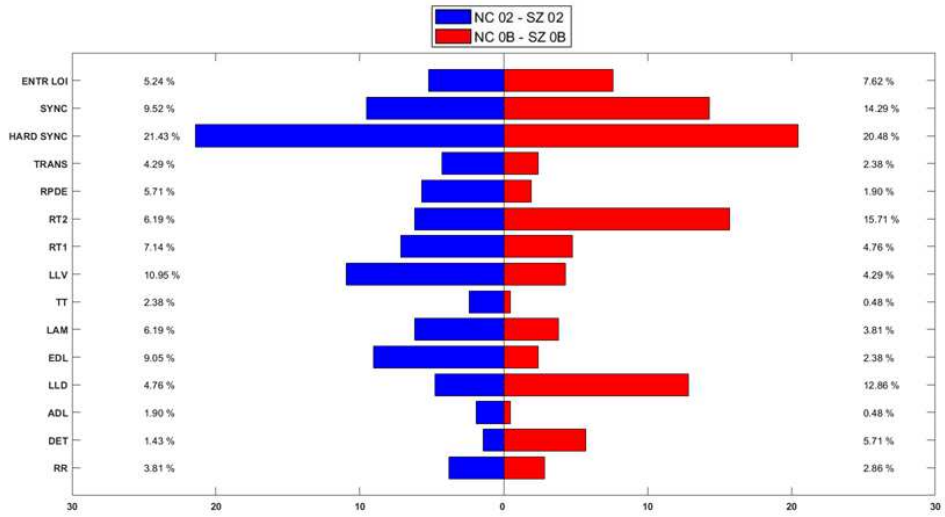

Fig. 4.5 Ranking of the multi-recurrence layers derived from the frequency of occurrence of the stable features according to the layer from which they belong for both the experiments.

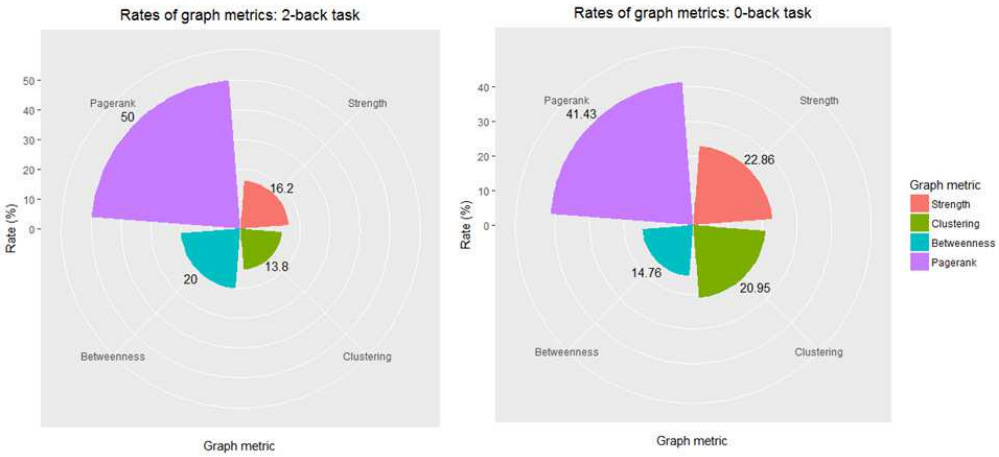

Fig. 4.6 Ranking of the multi-recurrence graph metrics derived from the frequency of occurrence of the stable features according to the graph metrics for both the experiments.

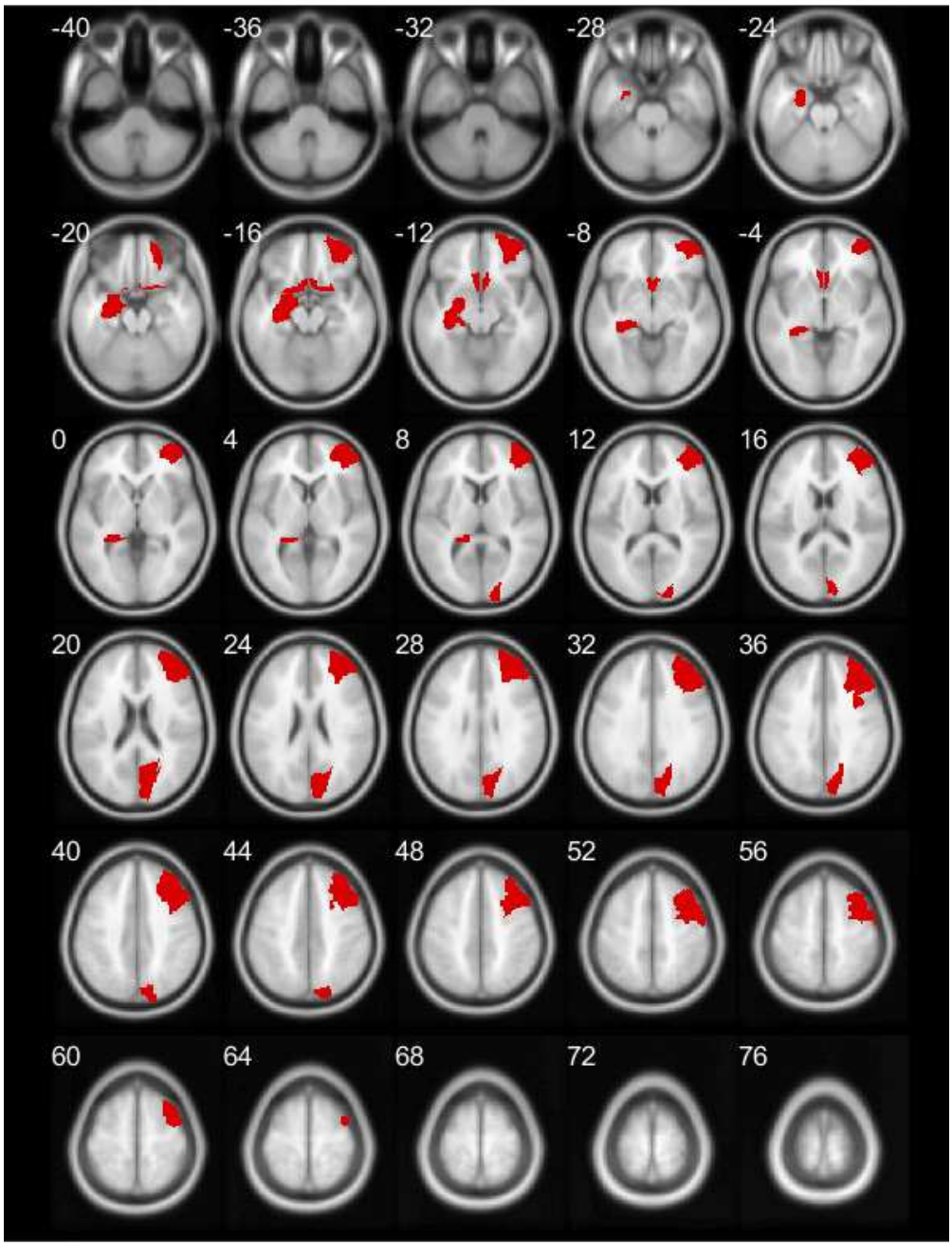

Fig. 4.7 Slice view of the most significant ROIs for the classification of the control/schizophrenic subjects during the 0-back task.

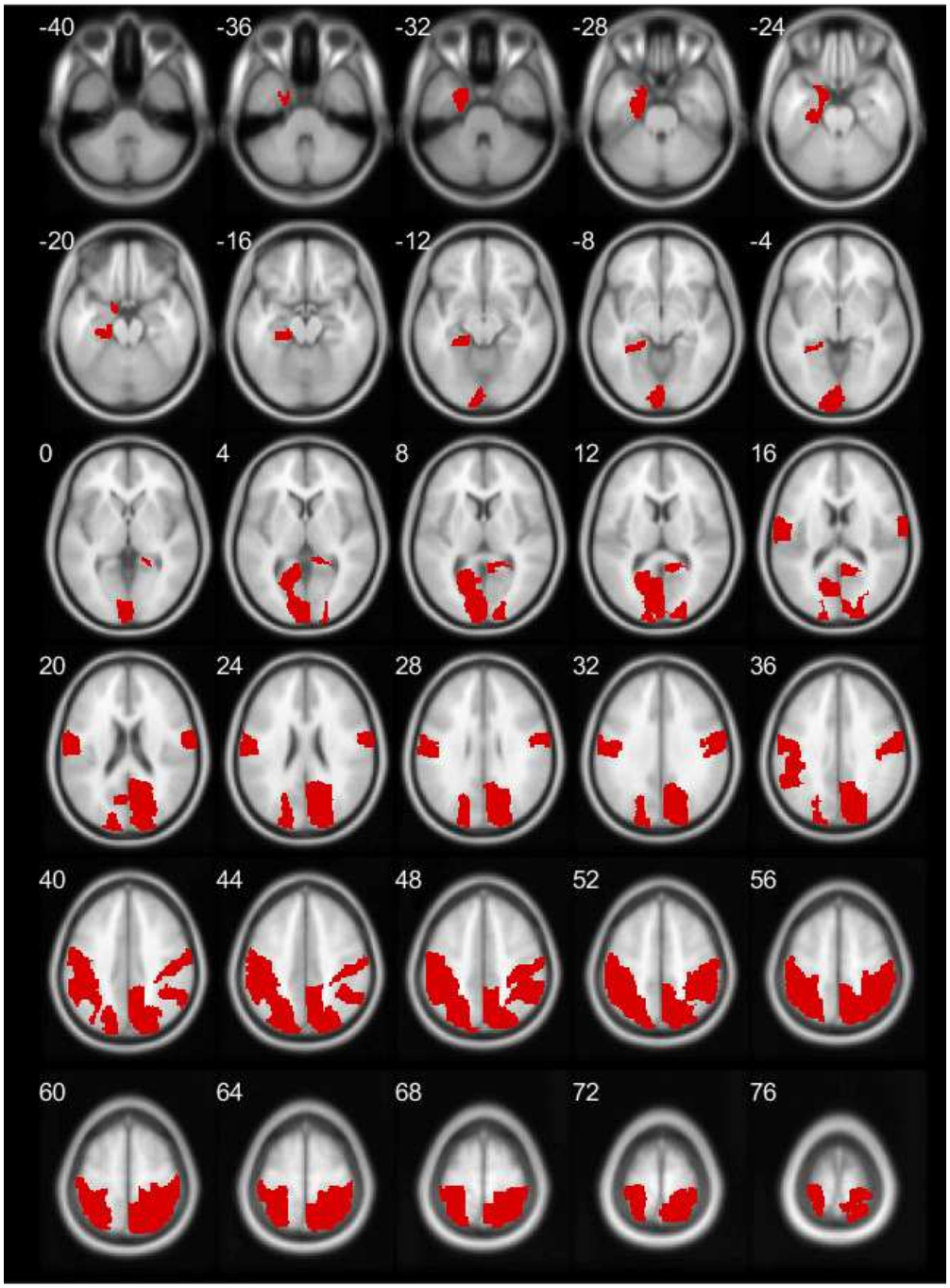

Fig. 4.8 Slice view of the most significant ROIs for the classification of the control/schizophrenic subjects during the 2-back task.

Table 4.2 Significant ROIs with MNI coordinates and p-values for 2-back task

ROI	MNI coordinate			p-value
	x	y	z	
ParaHippocampal L	−21	−16	−21	0.003
Calcarine L	−7	−79	6	0.02
Cuneus R	14	−79	28	<0.001
Occipital Sup L	−17	−84	28	<0.001
Occipital Sup R	24	−81	31	0.001
Postcentral L	−42	−23	49	0.04
Postcentral R	41	−25	53	0.002
Parietal Inf L	−43	−46	47	<0.001
Parietal Inf R	46	−46	50	0.002
Parietal Sup L	−23	−60	59	<0.001
Parietal Sup R	26	−59	62	0.02
Precuneus R	10	−56	44	0.005

Table 4.3 Significant ROIs with MNI coordinates and p-values for 0-back task

ROI	MNI coordinate			p-value
	x	y	z	
Frontal Mid R	38	33	34	0.02
Frontal Mid Orb R	−31	50	−10	0.02
Olf L	−8	15	−11	0.005
Olf R	10	16	−11	<0.001
Hippocampus	−25	−21	−10	0.005
Amygdala	−23	−1	−17	<0.001
Cuneus R	14	−79	28	0.02

The term "schizophrenia" was coined by the psychiatrist Bleuler to describe the characteristic "split" of consciousness of the disease [137]. Later, this aspect was widely investigated, looking for the physiological processes underlying the illness. Most of studies focused on functional and anatomical anomalies of brain regions, identified particular ROIs involved in cognitive dysfunctions, but the exact mechanism of disruption of normal functions is not yet fully explained.

Other studies have also considered an aberrant communication mechanism among the brain areas, defining a new hypothesis of functional disconnection underlying the disease [138]. Functional connectivity studies on whole-brain activity or specific seed-based analysis have shown alterations in brain systems such as fronto-temporal networks, cingulo-opercular circuits (implicated in salience processing), default mode network and fronto-parietal networks (involved in high cognitive functions). In addition, several studies have also associated the disease with abnormal configurations of hub regions [139]. Most connectivity studies refer to resting state data, aimed at assessing intrinsic functional brain connectivity. Tak-based study have been mainly addressed the detection of communities during several tasks and their functional reorganization over time. Although the results of the analysis are not directly comparable with these studies, Figure 4.8 clearly highlights working-memory related areas as discriminant features during the 2-back task (also reported in Table 4.2), while visual-processing related area are among the ROIs detected as relevant during the 0-back experiment (shown in Figure 4.7 and Table 4.3). It is interesting to note that the hippocampal and parahippocampal area resulted significant in both tasks. Recent findings have uncovered new insights into the relation existing between hippocampal formation and dorsolateral prefrontal cortex and their implication in schizophrenia. In detail, it has been hypothesized that the pathophysiology of the disorder might involve an alteration of functional interactions between medial temporal and prefrontal areas. A study involving both 0-back and 2-back tasks have shown that an inappropriate reciprocal modulatory interaction between prefrontal areas and hippocampus could be related to schizophrenia manifestation [140].

Another interesting aspect concerns the layers of the multi-recurrence structure most significant for the classification between schizophrenic subjects and controls. Metrics that assess averaged quantities such as TT, ADL, DET and RR, are the least frequent among all the levels, so the two populations do not show any significant differences with respect to these metrics. In contrast, among the most frequent levels, there are: LLD and RT2 for the 0-back task and LLV and

EDL for the 2-back task. These findings seem to suggest that the two groups of subjects have similar dynamic behaviors over the entire observation time interval, but differ over the maximum time intervals in which couple of regions are synchronized (or desynchronized as in the case of RT2). This is also confirmed by the two synchronization-related metrics (HARD SYNC and SYNC). Indeed the HARD SYNC is the most frequent layer for both the experiments. HARD SYNC emphasizes the concept of synchronization expressed by the SYNC as it is a binary metric that indicates the connectivity between a pair of ROIs only in case of perfect synchronization between the two areas (i. e., in case of the presence of the LOS) and it assigns a zero value otherwise. Although in a different context, altered oscillatory activity has been found associated with several neuropsychiatric disorders, including schizophrenia. Findings from noninvasive studies using EEG/MEG that demonstrate impaired amplitude and synchrony of neural oscillations at low- and high-frequency ranges in patients with schizophrenia have been also reported [141]. Consequently, disruptions in neural synchronization may represent the functional relationship of disordered connectivity of cortical networks underlying the fragmentation of behavior in schizophrenia [142]. In this work, a multidimensional evaluation of the features is performed: since classifiers have been used to select the most discriminating subset of features, the analysis does not identify statistical differences between the individual features detected as significant in the classification problem. However, the results obtained may be the starting point for further investigations to identify areas with significant synchronization differences.

Finally, the classification results indicate high margins of accuracy compared to those known in literature. In a recent review [19], the main results related to the classification of subjects suffering from schizophrenia with fMRI features are provided. Even though most of them refer to different tasks (such as OAD tasks) or resting state, it is worth noting that, apart from some studies with a very small number of samples, the maximum accuracy value is on average 80%.

4.6 Summary

In this chapter, a framework based on both CRPs and graph analysis to fully describe dynamic functional connectivity is presented. The framework was used to classify two clinical population: a group of control subjects and a pathological group of schizophrenics performing an executive task and a working memory task. fMRI data of each subject were partitioned into ROIs and fMRI time

series were extracted from each ROI of the volume. Couple of signals were mapped into their phase-space and a set of cross recurrence metrics were derived from the CRP of the interacting systems. They were used to construct a multi-layer recurrence structure from which topological features were extracted and treated as complex features for the classification problem. Results show that performances slightly outperformed those obtained in the literature. In addition, the regions resulting significant for the classification resemble task-related and disease-related ROIs.

Chapter 5

A new resilience index

5.1 A resilience perspective of centrality

Besides the brain networks, many other biological, social and technological phenomena can be modeled as complex interactions among constituent parts [143]. The investigation of these networks through different graph metrics has highlighted important features such as small average shortest path length and large clustering, identifying a wide variety of small-world type behaviors [144] or the presence of many hubs in some kinds of networks with power law degree distributions [145].

The topology of a network defines a network structure on which physical processes dynamically evolve. Even though the topological analysis of these networks has revealed important properties about their organization, real complex networks are implicitly weighted. Indeed, the heterogeneity of the interactions among the nodes can be encoded by assigning weights to the links of the network. Weighted networks have turned to be particularly important to model systems where the intensity of the relations between the nodes is critical.

Several graph metrics that are able to characterize the statistical properties of weighted networks combining both topology and weight distributions have been proposed [17]. As seen in Chapter 2, among these metrics, the most important are:

- degree;
- strength;
- betweenness;

- closeness;
- eigenvector centrality.

These indices evaluate the importance of a node according to several factors: degree and strength are local measures of centrality which simply considers respectively the number and the weights of links connecting to each node; closeness and betweenness centrality are global centrality measures that take into account the distance from a node to all the other nodes of the network; the eigenvector centrality is a self-referential measure of "influence" of a node so that the centrality of a node depends on the centrality of its neighbors.

Although these measures allow to quantify the centrality, cohesiveness and influence of a node in a complete and heterogeneous way, they do not consider the dynamic evolution of the network. More recently, the concept of "importance" of a node has also been related to the idea of structural robustness amongst failures (i.e., resilience) in a network percolation context [146, 147].

Percolation theory provides both analytical and methodological tools to characterize the global connectivity of complex networks during phase transitions [148, 149]. Several models describing percolation processes are available, however all of them assume a network structure whereby either nodes or edges are deleted with a certain probability p randomly or with a targeted procedure. A connectivity phase persists when a single connected giant component exists, and it disappears when the network collapses into disconnected clusters.

The resilience of the network can be measured as the variation of the size of the giant component during the percolation transition between the two extreme connected and disconnected phases and by the percolation threshold p_c, i.e., the critical probability at which the giant component forms and below which the network is composed of isolated clusters [150]. Other approaches have been proposed to assess the degree of fragmentation of a network when a finite number of links are removed. Basically, different centrality metrics are evaluated meanwhile links are gradually removed from the network. In [151] a pointwise version of the vulnerability index introduced by Latora and Marchiori [152] is presented together with a fluctuation index to describe the hierarchical properties of both regular and random networks. In details, the vulnerability of a node is measured as relative drop of efficiency after removal of the node and all links connecting it with other nodes of the network. In [153], powers of the links' betweenness are combined to define a multi-scale version of the vulnerability of a network. Mishkovski and co-workers suggested the normalized average edge

betweenness to assess the structural robustness of the network when a number of nodes and/or links are removed [154], while a more detailed definition of percolation centrality considers the proportion of shortest paths between a pair of nodes, where the source node is percolated [155]. This latter definition implies a dynamic growth model in which, for each temporal instant, a target node can assume a specific percolation state (total, absent or partial).

5.2 The proposed resilience index

Here a new resilience index is proposed to capture the importance of both nodes and links of a complex network. Specifically, a multidimensional approach is adopted to quantifies the importance of nodes and links in relation to their survival rate for progressive removal of links in the network. The computation of the resilience index requires the following steps which are also shown in Figure 5.1:

1. given the adjacency matrix W of the network, in which the entry (i, j) indicates the weight of the link between the node i and j (w_{ij}), the range of all the weights is divided into L levels. In this step, L percolation levels are identified;

2. the matrix W is incrementally thresholded by removing all the links whose weight is below the threshold at each of the L levels;

3. a multilayer matrix T is defined where the entry (i, j, l) represents the weight of the link between the nodes i and j at the l^{th} level of percolation;

4. the connectivity pattern of the node i for the l^{th} level of percolation is defined as:
$$P_{i,l} = T_{i,j,l} \qquad j = 1, \ldots, N. \tag{5.1}$$

5. the similarity between connectivity patterns of each couple of nodes at each level of percolation is expressed as their cosine similarity:
$$D_{ij,l} = \frac{P_{i,l} \cdot P_{j,l}}{\|P_{i,l}\|_2 \|P_{j,l}\|_2}. \tag{5.2}$$

6. $D_{ij,l} \neq 0$ for a certain degree of similarity between the connectivity patterns of the nodes i and j and it is set $D_{ij,l} = 0$ if the node i or the node j becomes disconnected. Similarly, $D_{ii,l} = 1$ if the node i is connected

at least with another node of the network and $D_{ii,l} = 0$ if it becomes completely isolated from the rest of the network. The resilience index of the link (RI_{link}) between the nodes i and j is defined as the area under the curve $D_{ij} = D_{ij,l}$, $l = 1, \ldots, L$:

$$RI_{ij} = \int_0^L D_{ij,l}\, dl \tag{5.3}$$

Likewise, the resilience index of the node (RI_{node}) i is expressed as:

$$RI_i = \int_0^L D_{ii,l}\, dl \tag{5.4}$$

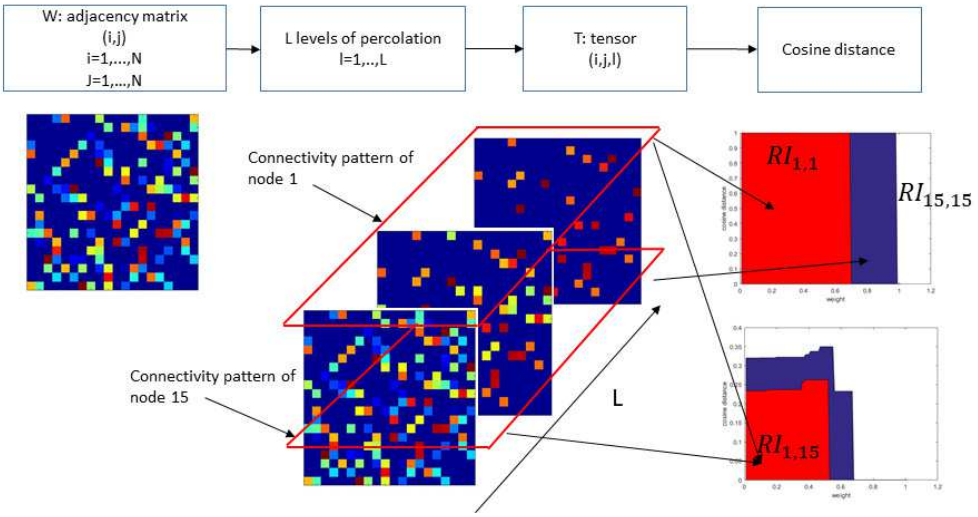

Fig. 5.1 Steps required to assess the resilience index. The adjacency matrix is percolated into L levels and a tensor T is composed of the matrices resulting from each percolation level. The cosine distance between couple of connectivity patterns of the nodes is computed to assess a percolation curve. Finally the resilience index is expressed as the area under the curve.

5.3 Experiments

Many real networks exhibit a scale-free degree distribution which is characterized by the two important mechanisms of growth and preferential attachment [17, 156, 157]. The former means that the number of nodes in the network increases over time, while the latter expresses that nodes with higher degree

have more probability to grab new links. Then, in a scale-free topology, most of the nodes are weakly connected and only few strongly connected nodes are the critical hubs of the network. Synthetic scale-free networks can be generated by using the Barabási-Albert (B-A) algorithm [158]. Accordingly, the resulting networks have a power law degree distribution $P(k) \sim k^{-\gamma}$ with $1 \leq \gamma \leq 3$. However, although the topological properties can highlight many interesting aspects of such real networks, it has been showed that a number of systems with scale-free topology also present broad distributions of weights and non-trivial correlations between weights and topology structure[17, 159]. Hence, the heterogeneity of the weight distributions should be considered to investigate the complex features of real scale-free networks[55]. In this work, weighted undirected networks with scale-free topology are simulated to test the capability of the proposed resilience index to detect the most important nodes and links of the networks. Different weight distributions are considered in order to take into account the heterogeneity of link strength in a real scenario. Other centrality metrics known in the literature are compared to show their correlation with the proposed index.

5.3.1 A scale free example

The B-A algorithm was used to generate two synthetic scale-free networks with the same power law degree distribution $P(k) \sim k^{-\gamma}$ with $\gamma = 2$. In particular, in order to represent two different kinds of weight-topology correlations, the weight of the link $w_{i,j}$ between nodes i and j was assigned as:

1. $w_{i,j} = k_i k_j$, to simulate a power law weight distribution setting a full weight-topology correlation.

2. $w_{i,j} \sim \mathscr{U}(0, 1)$, where a random uniform distribution of numbers in the range $[0, 1]$ is introduced to remove the correlation between weights and topology structure.

The reference scale-free network composed by $N = 100$ nodes and the two aforementioned realizations of the weight distributions are shown in Figure 5.2. As it can be seen, the most significant link in the power law case is established between the the two hubs of the network.

For each of the two networks were computed:

- the following node centrality metrics: degree (K); strength (S); betweenness (BC); closeness (CC); eigenvector centrality (EIG);

- the edge betweenness (EB) as link metric.

Then, a correlation analysis was carried out to:

- investigate the presence of possible correlations between the proposed index and the all the other centrality metrics;
- examine the ranking mechanism of each nodal centrality metric with respect to the two weight distributions. To this end, Pearson's correlation coefficient was computed for the two weight distributions for each nodal metric. The correlation coefficient has a range $-1 \leq r \leq 1$, where the coefficient has value 1 for perfect ranking, value -1 for anti-correlation (i.e., one ranking is the reverse of the other) and value 0 for for two uncorrelated rankings.

5.3.2 A simulation study

Numerical simulations of 100 scale-free networks with the same parameters, were conducted to generalize the results. In particular, for each of the 100 simulated network, the weights of the starting power-law distribution were progressively randomized until a completely random final configuration. The correlation analysis between the proposed index and each of the known metrics was carried out for each randomization interval of the weights, while the comparison of the node rankings was only performed between the initial and the final configuration for each nodal metric.

5.3.3 Results

The centrality metrics evaluated for each node of the two networks and are shown in Figure 5.3. Obviously, the degree function is the same for both networks because they have the same structural topology. Strength and eigenvector values are emphasized for both hub nodes of the network (nodes 1 and 4 as it can be noted in Figure 5.2) and for few other nodes with degree greater than that of the "leaf" nodes, i.e., those nodes with just one link. The values of betweenness are slight different only for the two hubs, so this metric seems to not take almost into account the distribution of the weights. On the other hand, some nodes with few connections exhibit high values of the resilience index for the random weight distribution, while its trend is closely correlated with that of the eigenvector centrality for the weight power law. The behavior of closeness

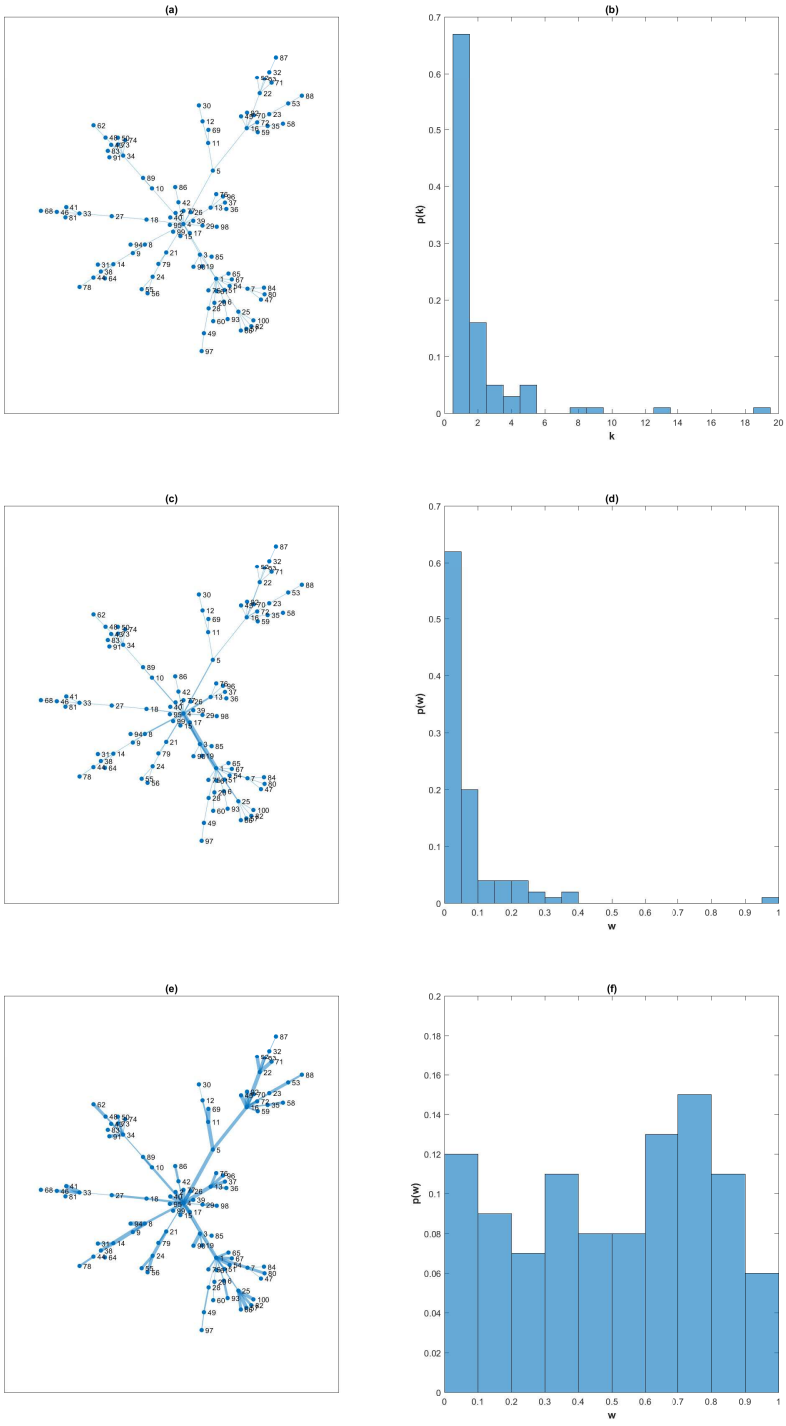

Fig. 5.2 A scale-free network topology composed by N = 100 nodes: (a) unweighted graph; (b) degree distribution; (c) power law weight graph; (d) power law weight distribution; (e) random uniform weight graph; (f) random uniform weight distribution. Line width of the links are proportional to their weight.

centrality is clearly different in the two networks, and it is considerably lower for all nodes of the network with random weight distribution. However, there is no apparent relationship between the centrality values and the role of nodes (hubs vs. leaf nodes).

The results of the correlation analysis between the proposed metric and the other centrality measures are listed in Table 5.1. High correlation values are observed for all centrality metrics except for the closeness centrality in the network with scale-free weight distribution; whereas there are low correlations (< 0.4) between the resilience index and degree, betweenness and eigenvector centrality respectively in the random weight distribution network. Strength and the proposed index seem to exhibit the highest value of correlation in the latter network, while closeness is negatively correlated, even if with low correlation index. Moreover, there is no correlation between the resilience index defined for the links and the edge betweenness for both weight distributions.

The rank correlation for each centrality metric is shown in Table 5.2. Strength, betweenness (both nodal and edge) and eigenvector centralities display significant high correlation values between the ranking of the nodes (and the links for EB) in the two weight distributions, whilst closeness and resilience index are significantly dissimilar in ranking nodes. Although with a higher correlation value, the RI_{link} metric confirms the same behavior of the RI_{node}.

Fig.5.4 shows the evolution of the correlation between the RI_{node} and the other nodal metrics and between RI_{link} and edge betweenness as a function of the percentage of randomization of the weights for the 100 simulated networks starting from a configuration with scale-free weight distribution. All nodal metrics except CC, are highly correlated with the resilience index RI_{node} for low randomized of the weights and then correlation values decrease until they converge around the median value $r_m = 0.3$ for K, BC and EIG and $r_m = 0.5$ for S. The closeness centrality exhibits a median correlation value $r_m = 0.24$ at the scale-free weight distribution, decreasing to negative correlation values with median $r_m = -0.3$. RI_{link} and EB are almost uncorrelated for all percentages of randomization.

The rank correlation analysis on simulated networks highlights that both resilience metrics score the nodes and links of the two extreme network configurations with different importance scales. Indeed, as shown in Figure 5.5, they have the lowest correlation values; in contrast, both the betweenness metrics are insensitive to the distribution of weights, showing very high correlation between the ranking mechanisms in the two cases. S and EIG also have significantly

Table 5.1 Correlation between the resilience index and the other centrality metrics ($p < 0.0001$).

Network	K	S	BC	CC	EIG	EB
Power law	0.88	0.93	0.85	0.23	0.98	-0.0069
Uniform	0.32	0.50	0.29	-0.19	0.38	-0.0171

higher correlation values (respectively median $r_m = 0.9$ and $r_m = 0.8$), while CC exhibits lower values (median $r_m = 0.57$), confirming a different ranking of the nodes belonging to the two weight distributions.

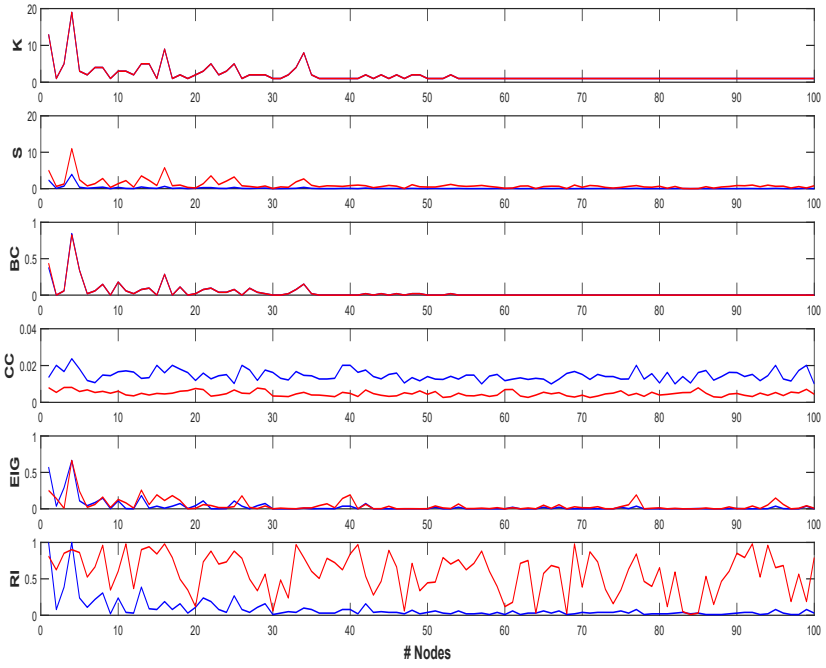

Fig. 5.3 Values of the centrality metrics (degree, strength, betweenness, closeness, eigenvector and resilience index) for each of the 100 nodes for the network with the power law weight distribution (blue) and that with the random uniform weight distribution (red) shown in Figure 5.2.

5.3.4 Discussion

The statistical analysis carried out highlights an interesting phenomenon: when the topology and the weight distribution are correlated, the proposed metric

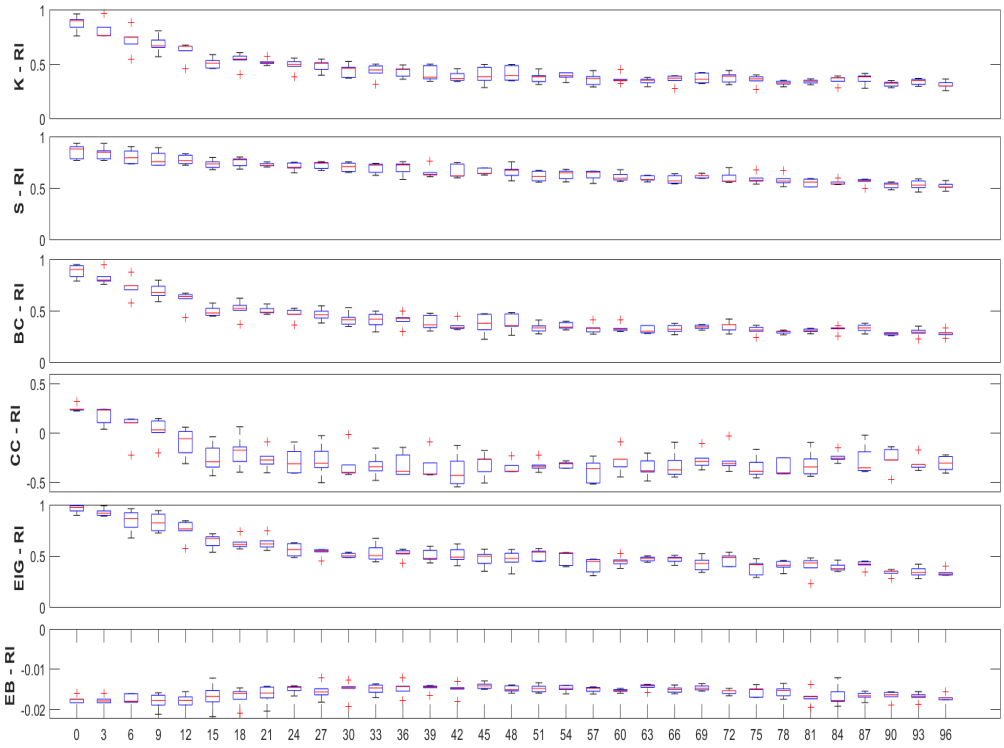

Fig. 5.4 Boxplots of correlation between the proposed index and each of the nodal centrality metrics for progressive randomization of the weights for the 100 simulated scale-free networks.

Table 5.2 Correlation coefficient (r) with p-value (p) resulting from correlation between the rankings of the two weight distributions for each centrality metric.

	S	BC	CC	EIG	EB	RI_{node}	RI_{link}
r	0.87	0.99	0.18	0.98	0.98	0.28	0.45
p	<0.0001	<0.0001	0.007	0.38	<0.0001	0.003	<0.0001

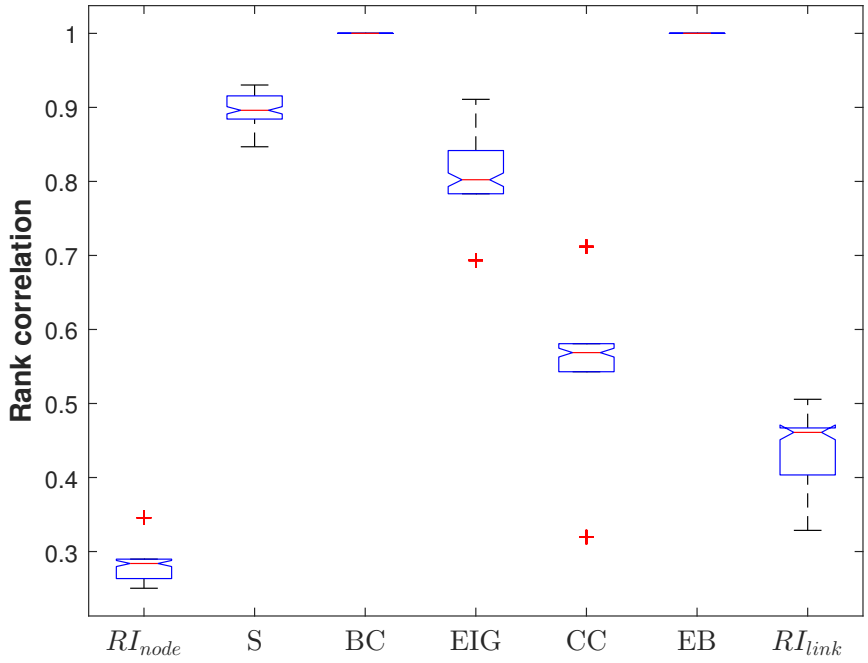

Fig. 5.5 Boxplots of correlation between node rankings (for the metrics: RI_{node}, S, BC, EIG and CC) and link rankings (for the metrics: EB and RI_{link}) of the initial configuration (i.e., with power-law weight distribution)and the final configuration (i.e., random uniform weight distribution) for the 100 simulated scale-free networks.

is not different from the others and resilient nodes are also central (and vice versa). However, when this correlation is removed, the proposed index is able to provide more information about the position of a node in relation to the network. The resilience index considers complete connectivity patterns of each node with the rest of the network at varying degrees of percolation. For this reason, even leaf nodes strongly connected to a particularly resilient node can also be resilient nodes. This aspect is clearly visible in the scale free networks with random weight distribution where weights are not assigned according to the underlying topological structure and even a peripheral node may have a strong connection with a hub node.

Real scale free networks with variable weight distributions have been identified and examined [146, 159, 55, 17]. In particular, criteria for both model and classify networks in which the connectivity of the node doesn't affect the weights of the links and networks in which the connectivity strongly influence them have been reported [160]. Several measures to characterize weighed networks have been proposed, but they have not been tested in this context so far. It is certainly true that identifying important nodes is not trivial. First of all, because there is no universal method for quantifying the importance of a node. The definition of centrality varies according to the context in which a specific metric is applied. In [161] some factors to evaluate each centrality metric are suggested: radial (e.g., degree, closeness, and eigenvector centrality) and medial measures (e.g.,betweenness centrality) are defined according to the information flow through the network and number of walks. A centrality metric should identify the role of the node in relation to the global characteristics of the network and not simply on the basis of the topology. The results of the rank correlation analysis show that some metrics assign very similar scores in the two situations. It is worth nothing the case of the betweenness centrality according to which the two networks seem to be completely similar. This finding could be due to the fact that some indices take into account only local information of a node. The proposed metric differs from all other centrality definitions since multidimensional patterns of connectivity are considered for its computation. It is also important to note that the resilience index should not be considered more effective than the other metrics just because it is able to better discriminate the two types of considered weight distribution, but that integrating the information provided by the other metrics with that of the proposed index could lead to new centrality metrics and reach a higher accuracy.

5.4 Summary

In this chapter a novel metric is proposed to quantify the importance of nodes in weighted networks in relation to their resilience. The proposed index takes into account the complete connectivity patterns of each node with all the other nodes in the network and it is not correlated with other centrality metrics in heterogeneous weight distributions. More effective metrics of centrality could be defined by integrating such new index with known centrality measures.

Chapter 6

Neuroscience: a Science of Challenges

Machine learning techniques have been greatly improved also thanks to international competitions. During such competitions, only the labels of a training set are usually disclosed. The test set remains unlabeled and participants have to develop an optimized predictive model on the training set. The final predictive model is tested on the unlabeled set and the predicted labels are submitted for evaluations. For a few years now, machine learning challenges have been spreading in the field of neuroscience, attracting more and more participants, even those not very experienced in this research domain. Such challenges can result very useful in assessing the unbiased power of brain data for detecting brain states and disorders since the models of different participants can be compared and the most discriminating features can be assessed from several points of view. The next sections will illustrate the machine learning algorithms developed to classify different diseases in the context of two international challenges.

6.1 mTOP Challenge

6.1.1 Traumatic Brain Injury

The purpose of the mTOP challenge was to predict outcomes for two categories of subjects suffering from mild Traumatic Brain Injury (TBI) and a group of normal controls (NC) .

A traumatic brain injury occurs when an external force causes a focused and sudden impact upon the head. The effects following a brain trauma may be

structural and morphological damages whose locations depends on the impact and secondary events due to changes in intracranial pressure and cerebrospinal fluid.

Complex network frameworks have been widely used to describe the topological brain organization and to distinguish Alzheimer's disease from control subjects [162]. Several findings suggested that topological measures could accurately detect patterns of mild impairment, emphasizing differences that structural measurements seem to less efficiently outline. Unlike a neurodegenerative disease, TBI does not have any connection with the genetic makeup of an individual. However, taking into account the different structural implications, it is reasonable to assume that a traumatic injury can affect the integrity of the brain connectivity and, therefore, that the identification of TBI outcomes can be improved by investigating the network organization of the brain. So, even if in a different context, in this challenge some connectivity measurements, such as strength or clustering coefficient, were evaluated to identify the category-I patients and then, once this diagnostic class was excluded, category-II patients were diagnosed with respect of normal controls using structural measurements.

6.1.2 Dataset

In mTOP challenge, a MRI dataset of 27 subjects including 15 labeled subjects divided into three classes (5 subjects per group) was provided. For each subject, raw T1-weighted and DWI scans were available; besides preprocessed data were also provided, including T1 scans rigidly normalized to the MNI152 template, the gross segmentations of white matter, gray matter and cerebrospinal fluid, the mean diffusivity (MD) map and the fractional anisotropy (FA) map.

The model was focused on the analysis of T1 scans, MD and FA maps. In fact, the rationale underlying this choice was that the information content provided from these three images is not redundant, since they are three different, complementary descriptions of the brain morphology and its connectivity. T1 captures morphological changes, MD measurements are sensitive to the cerebral spinal fluid (CSF), while the values of FA to white matter pathways [163].

6.1.3 Algorithm

The proposed approach consists of four main steps shown in Figure 6.1:

1. Each brain, for each considered imaging modality (T1, FA and MD), is parceled in a collection of patches representing the nodes of a network; edges of each network are the absolute pairwise Pearson's correlation between the supervoxels, thus resulting in an undirected weighted network;
2. from each network a number of statistical graph features are collected;
3. a k-nearest neighbors ($k-nn$) machine learning classification is used to differentiate the category-I patients from remaining subjects.
4. structural feature extraction is performed with FreeSurfer on NC and category-II patients;
5. k-nn machine learning classification is used for NC and category-II patients discrimination.

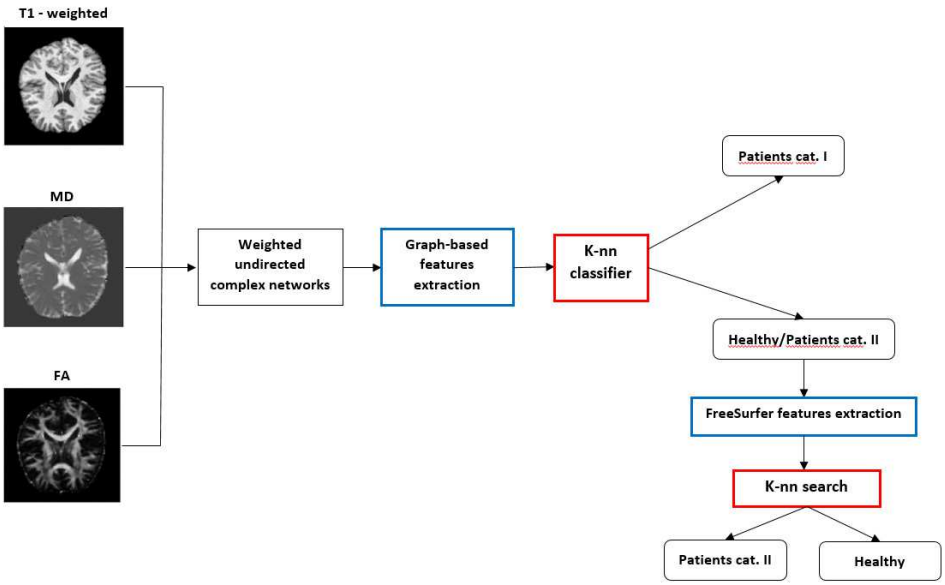

Fig. 6.1 A schematic overview of the proposed framework is presented.

Complex network construction

Once MRI scans had been co-registered, they were segmented in rectangular boxes, *supervoxels*. Firstly, brain hemispheres were separated, then each hemisphere was covered with an equal number of supervoxels. Using the brain mask of the template all supervoxels overlapping with the mask for less than 10%

were discarded. As scans had been spatially normalized it was reasonable to assume that:

1. within each brain the corresponding supervoxels included roughly the same regions;

2. gray level distributions of corresponding supervoxels should remain substantially unchanged unless heavy morphological variations.

Supervoxels were chosen to not represent pre-defined anatomical areas. In contrast to region of interest approaches, therefore, they do not rely on the segmentation accuracy of the anatomical regions. Moreover, as they collect the information related to thousands of voxels they are robust to typical artifacts of voxel-based morphometry approaches.

The supervoxel size D was chosen considering that supervoxels too small could be considerably affected by registration noise; on the contrary, extremely large supervoxels could conceal subtle differences making it harder to differentiate the groups. To investigate how the size of the supervoxel affected the accuracy of the analysis, D was varied from a minimum of 2000 to a maximum of 4000 voxels.

The proposed framework naturally introduces a graph description. The presented case in shown in Figure 6.2.

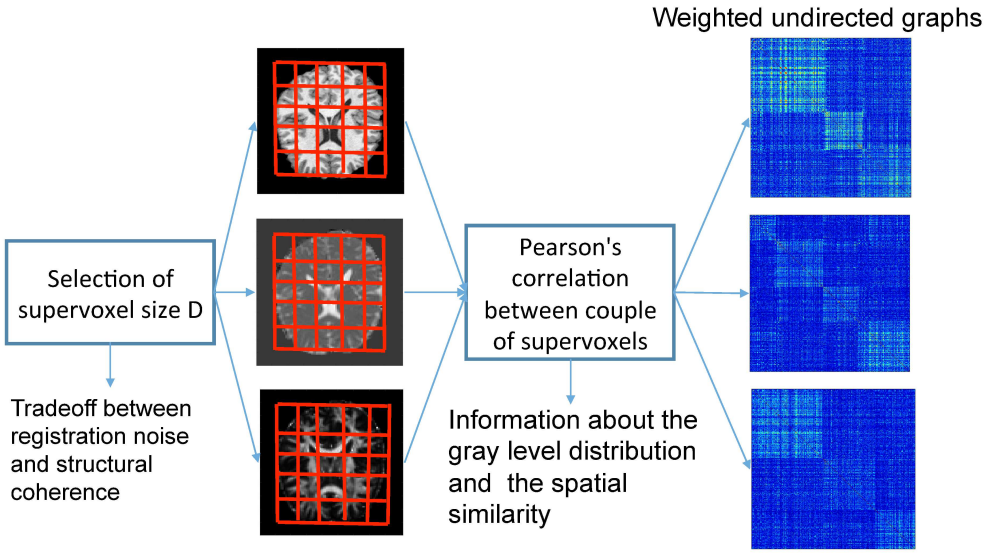

Fig. 6.2 Complex networks construction.

The supervoxels were considered nodes of a network whose connections represented the grade of similarity between them. Pearson's correlation r was the chosen metric:

$$r = \frac{D\sum_{j=1}^{D} x_j y_j - (\sum_{j=1}^{D} x_j)(\sum_{j=1}^{D} y_j)}{\sqrt{[D\sum_{j=1}^{D} x_j^2 - (\sum_{j=1}^{D} x_j)^2][D\sum_{j=1}^{D} y_j^2 - (\sum_{j=1}^{D} y_j)^2]}} \tag{6.1}$$

where the sums are extended to all D voxels within a supervoxel; x_j and y_j are the intensity of the j-th voxel. This choice has the fundamental advantage of combining not only the information deriving from the gray level distribution similarity between two supervoxels, but also their spatial similarity.

For each modality (T1, FA, MD) a weighted undirected complex network was built whose connections had been calculated through the absolute value of the Pearson's correlation coefficient between pairs of supervoxels.

Graph features

For each node i of a network, the following local topological metrics were computed:

- *strength*:
- the *clustering coefficient*

Moreover, *the characteristic path length* was used to characterize the overall efficiency of the network.

The Newman's spectral community detection algorithm [164] was used to partition each network into non-overlapping communities of nodes in order to reflect their modular organization. Therefore some features based on the detected communities were extracted to describe the role of each node in relation to each community and to objectively outline the strength of the connections between and within the modules. In particular the following metrics were considered:

- *the participation coefficient* of each node [165]:

$$P_i = 1 - \sum_{s=1}^{N_M} \left(\frac{\kappa_{is}}{k_i}\right)^2 \tag{6.2}$$

  where κ_{is} is the number of links from node i to nodes in module s, k_i is the degree of node i and N_M is the number of communities. It is an index of

the degree of participation of a node to the network communities since its value is close to 1 if the connections of the node are uniformly distributed among all the modules or 0 if all the connections are confined within a module.

- Defined the inter-community strength of a community l as the sum of the weights of links connecting the community l with all the other communities:

$$S_{INTER,l} = \sum_{\substack{m=1 \\ m \neq l}}^{N_M} W_{lm} \tag{6.3}$$

we used its average value over all the communities to measure the *inter-community strength* of the network.

- At the same manner, defined the intra-community strength of a community l with N_l nodes as the sum of the weights of links within it:

$$S_{INTRA,l} = \sum_{i=1}^{N_l} \sum_{j=i+1}^{N_l} w_{ij} \tag{6.4}$$

its average value is used to quantify the global *intra-community strength*.

For each subject and each modality, median, standard deviation, range and interquartile range of the distributions of strength, clustering coefficient and participation coefficient were calculated resulting in a 27×45 feature matrix used for $k-nn$ prediction.

k - Nearest Neighbors

The working principle of a $k-nn$ algorithm is the following: it identifies an established number (k) of closest training examples to a query point and assigns it the label of the class that has the most instances in the set of nearest neighbors of the point. The metric used to evaluate distances between points is cosine.

This technique offers some advantages over other unsupervised classification methods:

- it is a non-parametric instance-based learning method: it does not build a model so it might be more suitable in some particularly complex classification problems;

- it also works even in the presence of a small number of training examples. In this case, an unsupervised algorithm such as k-means or k-medoids, which makes decisions mainly based on the distance of a a query point from a centroid or medoid of a class, could introduce a significant bias in the presence of outliers.

In this challenge, a $k-nn$ classifier was used with a one-class discrimination logic in order to identify the category-I subjects against all the other subjects in a semi-unsupervised manner. For this purpose, given the matrix of the graph-based features, the $k-nn$ algorithm performed an exhaustive search to calculate the distance between the feature vectors of the subjects with unknown labels and those relating to the subjects of the category-I. This search provided a ranking of the subjects among which the closest ones were selected.

Structural feature extraction

The analysis was performed using volumetric and cortical thickness features computed with FreeSurfer [166]. FreeSurfer [1] is an image analysis software commonly adopted for the analysis and visualization of structural and functional neuroimaging data developed by the Laboratory for Computational Neuroimaging at the Athinoula A. Martinos Center for Biomedical Imaging. In particular, FreeSurfer tool v5.1 was employed in the cortical reconstruction to estimate the volumetric features in MRI. Specifically, only 180 features provided by the recon-all freesurfer command were extracted. To name a few: Left-Latera-Ventricle, Right-Latera-Ventricle, Left-Inf-Lat-Vent, Right-Inf-Lat-Vent, Left Hippocampus, Right Hippocampus, and many more.

The technical details of these procedures are described in prior publications [166–177]. Briefly, this processing includes motion correction and averaging [178] of multiple volumetric T1 weighted images (when more than one is available), removal of non-brain tissue using a hybrid watershed/surface deformation procedure [176], automated Talairach transformation, segmentation of the subcortical white matter and deep gray matter volumetric structures (including hippocampus, amygdala, caudate, putamen, ventricles) [166, 170] intensity normalization [179], tessellation of the gray matter white matter boundary, automated topology correction [169, 180], and surface deformation following intensity gradients to optimally place the gray/white and gray/cerebrospinal fluid borders at the location where the greatest shift in intensity defines the

[1] freesurfer.nmr.mgh.harvard.edu

transition to the other tissue class [167, 168, 177]. Once the cortical models are complete, a number of deformable procedures can be performed for further data processing and analysis including surface inflation [167], registration to a spherical atlas which utilized individual cortical folding patterns to match cortical geometry across subjects [172], parcellation of the cerebral cortex into units based on gyral and sulcal structure [173, 181], and creation of a variety of surface-based data including maps of curvature and sulcal depth. This method uses both intensity and continuity information from the entire three-dimensional MR volume in segmentation and deformation procedures to produce representations of cortical thickness, calculated as the closest distance from the gray/white boundary to the gray/CSF boundary at each vertex on the tessellated surface [168]. The maps are created using spatial intensity gradients across tissue classes and are therefore not simply reliant on absolute signal intensity. The maps produced are not restricted to the voxel resolution of the original data thus are capable of detecting submillimeter differences between groups. Procedures for the measurement of cortical thickness have been validated against histological analysis [182] and manual measurements [183, 184]. Freesurfer morphometric procedures have been demonstrated to show good test-retest reliability across scanner manufacturers and across field strengths [174, 185].

6.1.4 NC/Category-II patients discrimination

In the final step, the features extracted with FreeSurfer Tool were taken into account to distinguish controls from category-II subjects. Among all the features, those with high correlation values ($r > 0.9$) and those with low variance values (less than 0.2) were not considered. Starting from the two known sets, the $k-nn$ algorithm built two kd-trees to identify the subjects belonging from each group.

6.1.5 Results of the Challenge and discussion

During the challenge, a framework to perform semi-unsupervised outcome prediction for two categories of Mild TBI was presented. In particular, a two-steps classification pipeline was adopted to emphasize the differences between the healthy control group and the two patient groups.

In the first step, a complex network approach was applied to construct graphs from available scans and to extract the topological features used to identify category-I patients amongst all subjects. The mathematical model underlying the graph theory was chosen because it provides a direct description of the

structural properties of a network. Furthermore, a multimodal analysis was carried out to reflect the heterogeneity of injury patterns that can affect the patient cohorts. More specifically, bearing in mind that an early detection of changes in white matter tracts and in distribution of cerebrospinal fluid could improve significantly diagnoses and prognoses in case of diffuse axonal injury, contusions, edema and hemorrhages [186], MD and FA maps were considered as well as T1-weighted images. From each graph relating to each modality, topological features able to capture different relational aspects of the network elements, were computed. Besides the metrics commonly used to quantify the strength of the topological connections and the total efficiency of the network (i.e., strength and characteristic path length), a special focus was addressed to measures that reflect the modular organization of the interacting elements. So other measures such as the clustering coefficient, the participation coefficient, the intra-community and inter-community strength, were introduced with the aim of assessing the degree of weakening of the structural connections caused by injuries and the resulting configuration changes. Finally, second-level statistical features were extracted from the distributions of such metrics in order to provide a general description of all the sample images. Indeed, in principle, traumatic injuries could affect several brain regions causing extensive damage or they could be focal, compromising a specific functional area.

In the second step, the discrimination between controls and category-II patients were done by means of a k-nn classifier. At this stage, FreeSurfer volumetric and cortical thickness features proved to be effective in detecting morphological differences between the two groups of subjects. However, given the small number of examples for the two classes (five known labels for each group), dimensionality reduction of the the feature set was performed with minimum variance and maximum correlation criteria. As a matter of fact, a binary k-nn classifier relies on building two distance-trees, by calculating the distances between the training examples of each of the two groups and the unlabeled instances and subsequent by ranking these unknown instances. If the adopted distance metric is affected by noise due to the presence of low-significance features, the computation of the actual distance among the examples and the instances could be compromised, causing worse performances [187]. In fact, a dimension of the feature space much greater than the number of samples, would cause a problem of data sparsity, making inconsistent the computation of the distance between couple of points in the metric space.

In the context of the mTOP Challenge 2016, as winner, the performances of the proposed method have proven to be higher than those of other approaches based on Convolutional Network and Deep Learning. This framework has good generalization properties as is not constrained by the knowledge of the areas involved in the traumatic injury. However, future developments may require a greater number of training examples in order to validate the obtained results and improve the classification accuracy.

6.2 Automated diagnosis of Mild Cognitive Impairment

6.2.1 Diagnosis of Dementia

Alzheimer's disease (AD) is the most common form of dementia, but a reliable *in vivo* diagnosis is not at sight, yet. In recent years, novel strategies of analysis have been proposed to tackle this issue; in particular, several studies have addressed the challenging task of measuring the atrophy of specific regions, such as the hippocampus [188, 189], and eventually distinguishing healthy controls (HC) from patients suffering from AD and its prodromal stage: mild cognitive impairment (MCI) [190, 191].

A number of works have already established the effectiveness of neuroimaging techniques in outlining structural differences between AD patients and controls; nonetheless, these studies are difficult to compare and their findings hard to generalize as the adopted algorithms are different as the data. These are the main motivations for international challenges [192, 193], with transparent procedures and data sharing policies, to investigate algorithms and classification strategies.

In particular, MCI condition remains elusive, especially because only a fraction of subjects with MCI turns into AD patients (cMCI), whereas another fraction do not convert into AD (MCI). Some works suggested to address the classification of MCI and cMCI classes learning their models on mixed cohorts including all available classes: HC, AD, cMCI and MCI [194, 195]. Another option is to learn a classification model directly using a mixed cohort of MCI and cMCI subjects. The main drawback of these approaches is that MCI is highly heterogeneous as it can include subjects affected by different or multiple pathological conditions; besides, cMCI and MCI classes can hardly

be considered independent. Other studies have therefore suggested a different approach, learning the classification model on mixed cohort of HC and AD subjects and then predicting the conversion or not of MCI subjects [196, 197].

In this challenge, the aim was principally evaluating both strategies on the data shared by the challenge and, consequently, transparently investigating differences and similarities. In particular, a pure machine learning approach, exploiting a Random Forest (RF) for feature selection and a Deep Neural Network (DNN) for classification, using a mixed cohort including all the four classes HC, AD, MCI and cMCI, was compared with a fuzzy approach learned on a mixed cohort including only HC and AD subjects. The latter approach used the hippocampal volume to segregate the different classes and determine a proper set of features for each classification task.

Recent works demonstrated that models trained with HC and AD subjects can also be effective when attempting to distinguish MCI and cMCI. In fact, the differences among MCI and cMCI subjects are significantly subtler than those among AD and HC, thus a classification model learned on these latter two classes can achieve more accurate results [197–199].

Several classification studies have investigated the early diagnosis of AD, the characterization of MCI and, eventually, its conversion into AD; structural MRI features have been mostly adopted. Nevertheless, an international competition assessing different algorithms on the same training and test sets have not been performed yet. Accordingly, a novel international challenge was performed and hosted on the Kaggle platform[1] in order to assess existing and novel classification algorithms with a common framework of analysis and a shared base of knowledge.

The results of this work were publicly released on the Kaggle platform which hosted the competition of 19 international participating teams. The predictions were submitted within the Bari Medical Physics Group (BMPG) team flag.

6.2.2 Data and Algorithms

International Challenge for Automated Prediction of MCI from MRI Data

The adoption of machine learning techniques for the analysis of neuroimaging data has deeply influenced recent neuroscience studies, specifically concerning AD and its prodromal phase (MCI). In fact, machine learning can support the

[1] https://inclass.kaggle.com/c/mci-prediction

estimation of disease risk along with the estimation of therapy success or the effects of genotype-phenotype associations.

Recent studies exist about the early diagnosis of AD or the conversion of MCI subjects into AD. However, it is worth noting that an international competition among existing algorithms assessing the use of structural MRI markers has never been performed on the same training and test sets.

Accordingly, a set of T1-weighted MRI scans for patients of four categories, stable AD, MCI, MCI who converted to AD and healthy controls were analyzed using FreeSurfer v.5.3. The obtained features were released on Kaggle platform to allow research team from all around the world to compare their algorithms within an established framework and using the same data.

The participants were allowed to download specific training and test sets, in order to make results from different algorithms comparable, and submit their solutions in a text format. Kaggle tools allowed the visualization of intermediate scores by public/private leaderboard in terms of classification accuracy.

Challenge Data

Data were obtained from the ADNI database (adni.loni.usc.edu). The challenge organizers prepared a training set $\mathscr{D}_{train}$ consisting of 240 subjects, equally composed of 60 AD patients, 60 HC, 60 cMCI and 60 MCI subjects.

An anonymous id-code for identification, diagnosis, gender, age and baseline Mini Mental State Examination total score were provided for each subject; in addition, subcortical volumes, cortical thickness, cortical volume, cortical surface area, cortical thickness standard deviation, cortical curvature and hippocampal subfields' volumes resulted by FreeSurfer analysis along with several other structural measures accounting for an overall feature representation of $N = 431$ variables. Thus, $\mathscr{D}_{train}$ was represented as a matrix with 240 rows and 431 columns. An analogous test set $\mathscr{D}_{test}$, including 500 observations was provided by the organizing committee, except for the diagnosis: so that $\mathscr{D}_{test}$ was represented as a matrix with 500 rows and 430 columns. The $\mathscr{D}_{test}$ set included 340 simulated samples and 160 real subjects.

For what concerns the sampling, a three-fold procedure was adopted by the challenge organizers: (i) the whole cohort was downloaded from ADNI and randomly divided in training and test; (ii) the test sample was used to calculate the probability density function (pdf) of the features, accordingly the simulated data were obtained inverting the pdf previously calculated; (iii) finally, each simulated data was randomly labeled with a clinical status.

The size of both training and test sets were established from the challenge organizers, a random collection of 100 subjects for each clinical class was selected to keep these classes balanced and considering that MCI subjects are difficult to recruit. Further data could have been downloaded from ADNI, however only data provided by the challenge organizers were used in order to keep the results comparable with those obtained by other teams.

Challenge data was firstly cleaned; zero variance features were identified and removed. Besides, the presence of highly correlated features were investigated . In fact, 26 features (more than 90% of the total) resulted correlated. To further reduce the feature representation, linear combinations among the features were investigated and removed them from the data. After removing these variables, the resulting $\mathscr{D}_{train}$ matrix representation consisted of 242 features. Finally, training data was centered and scaled, in order to standardize the features with null average and unitary variance. The same operations were performed for the $\mathscr{D}_{test}$.

Feature selection

A Random Forest classifier [200] was employed to evaluate the feature importance in terms of mean decrease of accuracy. Random Forests are an ensemble of tree classifiers which can provide a direct multi-class model.

A standard configuration was adopted with 500 trees and 20 features (as prescribed in [200]) randomly selected at each split. A total number of 100 5-fold cross-validation rounds were performed and for each round only the 20 most important features were selected. This parameter was chosen observing that no significant improvement occurred in training classification accuracy using more features.

As expected, hippocampal volumes were found among the best performing features. Other AD related features such as the the cerebrospinal fluid volume, the lateral ventricle volume and the enthorinal cortex thickness were selected. Interestingly, right hippocampus rank resulted higher than the left one; in addition the best performing feature was by far the baseline MMSE, see Figure 6.3 for an overview.

Structural measures of both right and left hemispheres were selected; their number was almost equal showing no manifest asymmetry. In fact, the selected left hemisphere measures were 9 against 10 from the right. The selected features were then used to train a Deep Neural Network.

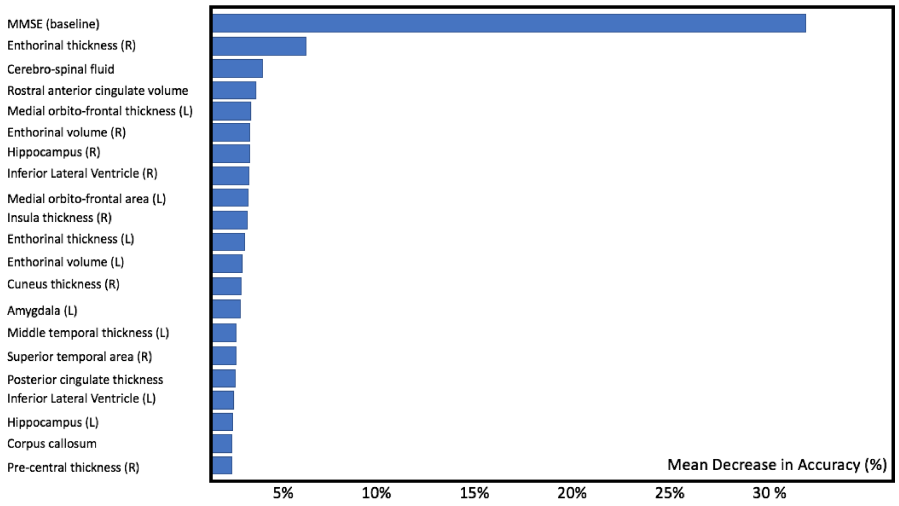

Fig. 6.3 The feature importance measured in term of mean decrease in classification accuracy with a Random Forest classifier. When appropriate, the left (L) or the right (R) hemisphere is reported.

Deep Neural Networks

A deep neural network (DNN) is a neural network with more than two hidden layers of neurons [201, 202]. In particular, a feedforward DNN, which learned to map the feature representation of each patient in the four aforementioned classes, was chosen for this Challenge. Each unit within a layer computes a weighted sum of the inputs from the previous layer, then its result becomes the argument of a nonlinear transformation (relu or tanh), then it feeds the subsequent layers until the final layer is reached and a final score is computed. In particular, a softmax nonlinear function was used to obtain the final score [203], see Figure 6.4 for a representation.

DNNs have shown promising results in several applications ranging from image classification to natural language applications [201, 202]. More recently, they showed excellent results for the development of computer-aided detection applications [204–206].

The optimal size of a training set depends in general on several factors, especially on how separate are the classes to be investigated. In particular, when the performance on the training set remains stable whatever configuration of learning is considered, an option to be considered is that gathering more data would not be helpful. In order to improve the learning algorithm, the size of the model was increased by adding more hidden units to each layer, as well as tuning the learning rate hyperparameter. Specifically, after several cross-

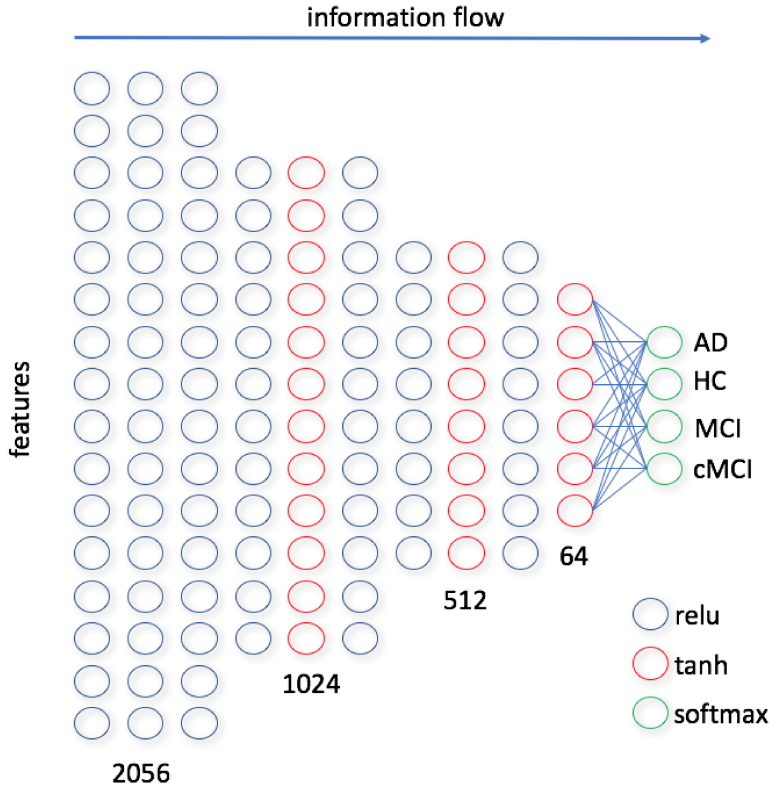

Fig. 6.4 The optimal network configuration was obtained in cross-validation. The number of neurons within each layer decreases according to the flow of information from features to output labels.

validation analysis the best DNN configuration was determined with 11 layers and a decreasing number of neurons: any further increase in the number of layers or neurons did not yield any improvement. The input layer consisted of 2056 units while the last one just included 4 (one for each class); a mixed optimal configuration of activation functions (relu and tanh) was determined with a cross-validation analysis [207]. The DNN loss function was the categorical cross entropy; it was minimized with the Adam optimizer [208].

For better robustness, the network weights were randomly initialized from a uniform distribution, thus resulting in different models. 30 different initializations were performed. The classification scores from each model were then averaged to obtain a final prediction, each test subject was assigned the class with the resulting higher score.

Fuzzy classes of hippocampal volume

Hippocampal atrophy is a well known biomarker for AD progression state [209, 210]. In a previous work, the use of homogeneous classes of subjects were proposed to perform different feature selection on MRI data [191]. The highly variable nature of the hippocampal morphology suggested the use of a fuzzy logic to generalize the definition of set by redefining the concept of membership. Specifically, let X be a space of points, with a generic element of X denoted by x. A fuzzy set $A \in X$ is characterized by a membership function $f_A(x)$ that associates with each point in X a real number in the interval $[0,1]$, with the values of $f_A(x)$ representing the grade of membership of x in A. Thus, the nearer the value of $f_A(x)$ to unity, the higher the grade of membership of x in A [211]. The core of the fuzzy set A is the subset of values of x that belong to the class A with maximum degree.

A statistically consistent subdivision of the training cohort was found in three fuzzy classes according to the subject's left hippocampal volume. Firstly, a classification of training subjects was performed and looking at Receiving Operating Characteristic (ROC) curve the optimal threshold value t separating HC and AD classes was selected. Thus, the fuzzy set $\mathscr{L}$ including subjects with the left hippocampal volume V satisfying the relationship $V \leq t$ was defined; analogously, the fuzzy set $\mathscr{H}$ was defined when $V \geq t$. These two sets were mutually exclusive. However, there are subjects belonging to $\mathscr{H}$ which are AD and HC subjects in $\mathscr{L}$. To take this effect into account, a third fuzzy set $\mathscr{M}$ was taken into account. The median values l_1 and l_2 of left hippocampal volumes of AD ad HC subjects, respectively, were computed;

the median value of left hippocampal volumes of HC subjects was l_2. These values satisfied the inequality $l_1 \leq t \leq l_2$ so that a third fuzzy set was suitably introduced including subjects whose left hippocampal volume satisfied $l_1 \leq V \leq l_2$. Within each fuzzy set, the probability for a subject to belong to a specific class was reasonably different; for example, subjects belonging to the $\mathscr{L}$ set were more likely to be AD, having a small hippocampal volume, than HC. Thus, a specific feature selection was performed for each set in order to obtain a more adherent representation of its population. In particular, a Kruskal-Wallis test was performed and only those structural features exceeding the 5% significance were used to learn the model.

Classification model

A schematic overview of the framework here adopted is presented in Figure 6.5. A standard RF classifier was trained for each set $\mathscr{L}$, $\mathscr{M}$ and $\mathscr{H}$, then the subject's membership to each set was assessed and finally the subject's classification score S was obtained by averaging the scores obtained from each model according to the membership.

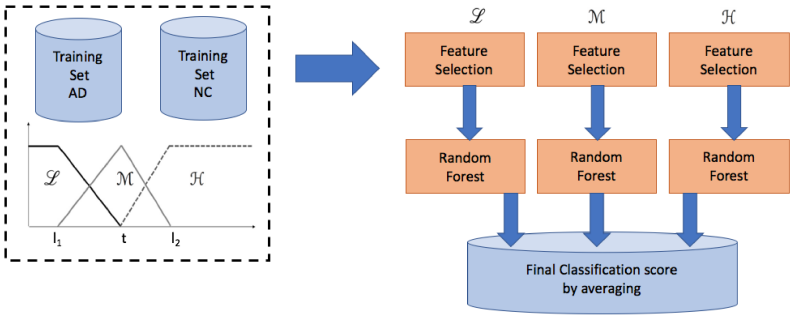

Fig. 6.5 A schematic overview of the proposed fuzzy approach. Once the fuzzy sets $\mathscr{L}$, $\mathscr{M}$ and $\mathscr{H}$ have been defined, feature selection is performed and a RF model is trained for each set. The final classification score is obtained by averaging the models' predictions.

Finally, four diagnostic groups were obtained with a Bayesian approach. Three thresholds t_1, t_2, and t_3 were computed, maximizing the training classification accuracy for the classification of HC, AD, cMCI, and MCI classes. Specifically, subjects with the final score $S \geq t_3$ were classified AD, if $S \leq t_1$ HC, if $t_1 \leq S \leq t_2$ MCI and if $t_2 \leq S \leq t_3$ cMCI.

In order to evaluate the performance of the model, a 10-fold cross-validation was used. Specifically, the overall accuracy and the multi-class definition for

recall and precision were evaluated. The overall accuracy was the number of correctly classified subjects (true positive, TP) by the sample size N:

$$acc = \frac{TP}{N} \tag{6.5}$$

Recall R_c of a class was the number of subjects belonging to the class correctly classified (TP_c) by the overall class size N_c:

$$R_c = \frac{TP_c}{N_c} \tag{6.6}$$

Analogously, precision P_c of a class was the number of correctly classified subjects (TP_c) divided by the number of predictions within that class $N_{p,c}$:

$$P_c = \frac{TP_c}{N_{p,c}} \tag{6.7}$$

For all reported results, average and standard deviations were computed when possible.

6.2.3 Results

Public and Private Leaderboards

The performance of all challenge competitors was publicly released in terms of classification accuracy; each one of the 19 participating teams could make a submission once a day. The Public Leaderboard kept record of the team name, the classification score, the number of entries and the best submission time, along with the ranking position. The BMPG best submission was obtained with the DNN model; the organizing committee adopted the previously defined accuracy metric, see Eq. 6.5, to evaluate the submissions. In particular, the BMPG submission obtained a 38.8% accuracy, resulting the seventh performance of the roaster, see Table 6.1.

The leaderboard performance was computed on approximately 50% of test data. Thus, it provided just an estimation of test results. In this case, the BMPG best submission reached the seventh position.

After the deadline for challenge submissions, the organizing committee released the Private Leaderboard performance computed on the entire $\mathscr{D}_{test}$. The Private Leaderboard performance resulted overoptimistic, with a 4% loss in accuracy; in fact, the BMPG final result was 34.8%. It is worth noting

Table 6.1 BMPG accuracy was 38.8% and resulted among the top ten algorithms presented in the Public Leaderboard including half of testing subjects.

Placement	Team name	Score accuaracy
1	SiPBA-UGR	0.424
2	Salvatore C. - Castiglioni I.	0.416
3	Loris Nanni	0.412
4	Stavros Dimitriadis - Dimitris LIparas	0.412
5	Sorensen	0.408
6	GRAAL	0.396
7	**BMPG**	0.388
8	ChaseCowart	0.384
9	Jean-Baptiste SCHIRATTI	0.384
10	BrainE	0.384

that training performances exceeded 50% accuracy (for all presented models). Nevertheless, the BMPG prediction reached the third position, see Table 6.2.

Table 6.2 MPG submission ranked third in the Private Leaderboard including all of testing subjects. The BMPG submission obtained a 34.8% accuracy.

Placement	Team name	Score accuaracy
1	Stavros Dimitriadis - Dimitris LIparas	0.360
2	GRAAL	0.356
3	**BMPG**	0.348
4	BrainE	0.344
5	gogogo	0.336
6	DevinAnnaWilley	0.336
7	fengxy	0.332
8	BoyX	0.328
9	ChaseCowart	0.328
10	Jean-Baptiste SCHIRATTI	0.324

After the submission deadline, the organizing committee released the test labels so that it was possible to investigate in detail the classification performance especially the model accuracy on real subjects. Such evaluation was reported in the following section.

Model comparison

The classification performance on training was evaluated on 100 rounds of 10-fold cross validation; the results are summarized in Table 6.3. The DNN model resulted the one with higher overall accuracy $acc = 53.7 \pm 1.9\%$, while

for the fuzzy model $acc = 50.9 \pm 1.1\%$. In particular, the DNN model had higher recall values for HC, AD and cMCI, while the fuzzy model showed a slightly higher precision for all classes, except AD.

Table 6.3 Recall and precision for the DNN and Fuzzy models on training subjects (average and standard deviation computed in cross-validation). Best performances are reported in bold.

	DNN		**Fuzzy**	
	recall	precision	recall	precision
AD	**80.9± 3.2 %**	**79.3 ± 1.7%**	66.2 ± 2.4%	66.8 ± 1.1%
HC	**53.8 ± 3.4%**	53.4 ± 2.4%	47.7 ± 3.5%	**54.8 ± 2.0%**
MCI	35.9 ± 4.3%	36.4 ± 3.5%	**46.1 ± 1.5%**	**37.9 ± 1.4%**
cMCI	**44.8 ± 3.0%**	45.0 ± 3.0%	43.8 ± 1.2%	**47.5 ± 1.8%**

The classification performance on real test subjects confirmed the DNN as the best model. In fact, the DNN model acquired a 56.3% accuracy while the fuzzy reached 52.2% accuracy, see Figure 6.6 for a comprehensive review of the classification results. Besides, recall and precision of both models are reported in Table 6.4.

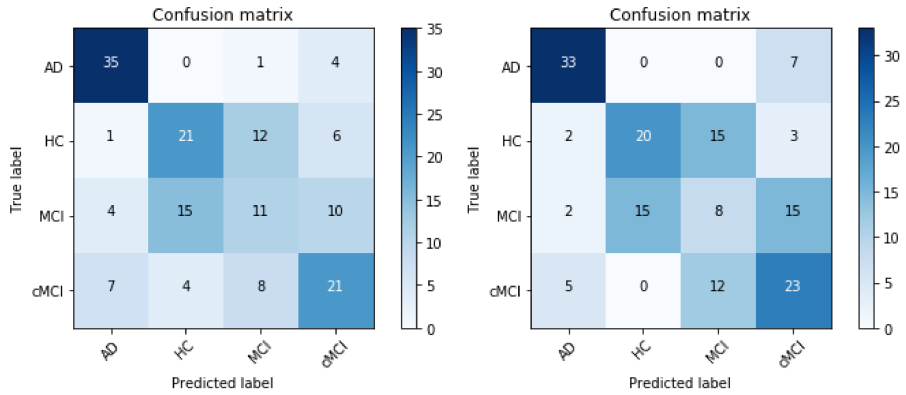

Fig. 6.6 The confusion matrices of the DNN best submission (left) and the fuzzy (right) models on real test subjects.

The DNN model resulted the one with higher recall for all classes, except cMCI; in this latter case, the fuzzy model had higher recall. For what concerned precision, the DNN model was the more precise with respect of MCI and cMCI while the fuzzy model was more precise with AD and HC.

Moreover, a direct comparison of predictions obtained by the two models was performed to evaluate their agreement, see Figure 6.7, on the 160 real test subjects. The two models agreed on 103 predictions, 64.3% of cases; a

Table 6.4 Recall and precision for the DNN, Fuzzy and RF models on real test subjects. Best performances are reported in bold.

	DNN		**Fuzzy**	
	recall	precision	recall	precision
AD	**87.5%**	74.5%	82.5%	**78.6%**
HC	**52.5%**	52.5%	50.0%	**55.9%**
MCI	**27.5%**	**34.3%**	20.0%	22.9%
cMCI	52.5%	**51.2%**	**57.5%**	47.9%

major difference was found for the MCI class with a agreement of 9.3%, to be compared with the best agreement of AD class which was 22.5%.

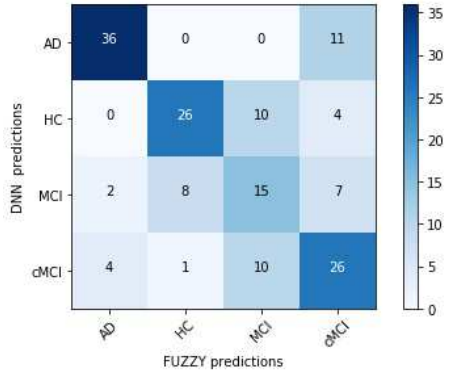

Fig. 6.7 The comparison matrix of DNN and fuzzy predictions on real test subjects. The overall agreement of predictions reached the 64.3%.

6.2.4 Discussion

This study confirms the effectiveness of DNN models for computer-aided detection systems. In fact, the classification results obtained by DNN allowed the BMPG group to obtain one of the most accurate prediction in the participants' roaster. Nevertheless, the multi-class classification accuracy is still far from reaching satisfactory results for clinical applicability. However, these findings compare well with state-of-the-art results; for example in [192] the best performing method reached a 63% accuracy for a three-class classification problem. Other works consider this as an intrinsically four-class classification problem [212], and, of course, in this case reported accuracies of 46.3% can reach lower values. Interestingly, classification accuracies reported in challenges is lower than those reported in literature.

From this perspective, this study also confirmed that the development of accurate algorithms for distinguishing MCI subjects who convert to AD from those who will not convert, is yet a challenging problem. The MMSE feature was by far the most informative one. This result suggests the need for further feature engineering studies to improve diagnostic accuracy. However, novel insight has been gained thanks to this competition. In particular, this study demonstrated that pure machine learning algorithms are generally those with higher recall but they can have poor precision.

The use of alternative approaches, such as the fuzzy logic for the present case, can in principle improve classification. In fact, the fuzzy approach adopted here was the most precise model when dealing with AD and HC. It was also observed that the two approaches had a relatively small overlap, with an agreement of 64.3%.

Another interesting aspect concerns the synthetic data. The organizing committee provided a test set including real subjects and simulated data. Moreover, the test performances obtained with all the three models on the entire test set were significantly lower than those obtaining during training. Specifically, for both models a $\sim 50\%$ accuracy was found while in test a significant decrease ($\sim 34\%$). On the contrary, when dealing with real subjects, test performances resulted in good agreement with training cross-validation accuracy: an important clue about the poor conformity of simulated data to real subjects.

6.3 Summary

In this chapter the results achieved during two international challenges for the classification of subjects with TBI and suffering from cognitive decline were presented. In both challenges, machine learning algorithms have proven to be effective in the selection of significant features for the outlined classification problems and in the accuracy of the results achieved.

Chapter 7

Conclusion and Future Works

In this thesis, some aspects regarding the multidimensional analysis of the human brain connectivity have been treated.

The first issue concerns the dynamic study of brain connectivity. Functional connectivity in human brain through functional magnetic resonance imaging is usually assessed by partitioning the whole brain volume into regions of interest and by computing statistical interactions between couple of fMRI time series. Usually the signal is windowed over time and the local connectivity, i.e., the one resulting from the single window, and its temporal evolution, i.e., its variation over overlapped windows, are examined to follow the functional organization of the brain during specific activities such as learning, memory tasks, or simply in resting state. This approach allows to track time variations, focusing on a single domain. In addition, it presents some problems related to the choice of optimal parameters for defining window lengths and spurious correlations. In this work, a phase-space framework is proposed as alternative to map pairs of signals belonging to ROIs, in their reconstructed phase space, in order to allow a topological representation of their behavior under all possible initial conditions. This method offers the opportunity to study a dynamic phenomenon starting from real observations and to detect its main properties. One of these properties is linked to the concept of synchronization. Studying a system in its phase space enables to assert generalized synchronization measures between time series. Here, a new generalized synchronization metric defined on cross recurrence plots, a two-dimensional projection of the phase space, is presented. Specifically, this step makes it possible to reduce the size of the phase space for any input size, retrieving only the information needed to effectively explore the dynamics of a system. The synchronization metric is then extracted from

the cross recurrence plot to assess the coupling behavior of the time series. The proposed metric is a generalized synchronization measure that takes into account both the amplitude and phase coupling between pairs of fMRI series. It differs from the correlation measures used in the literature, as it seems to be more sensitive to nonlinear coupling phenomena between time series and it is more robust against the physiological noise. The results achieved are promising with respect to the value of the novel proposed technique, even though they are not free of limitations. For example, since task-dependent time-series were considered, future studies would verify whether these results extend to resting state data. Another relevant point concerns the modularity properties used to perform the comparison between the SYNC metric and the Pearson's correlation index. Indeed, in the analysis both higher modularity and higher consistency of task-related communities were found in the SYNC matrices. These features are related to a greater homogeneity of the functional organization across the subjects in response to the same task and although they are compatible with behaviors expected in a healthy cohort, a more rigorous assessment of the sensitivity of the proposed synchronization metric should require further analysis. Future studies could employ alternative topological properties of SYNC networks and their correlation with task performance or behavioral data to uncover additional insights into the suitability of the SYNC index as a functional connectivity metric for fMRI time series. Then, this study has focused on an alternative method to define functional connectivity between pairs of BOLD time series. Generally, functional connectivity refers to a larger spectrum of neuroimaging techniques including EEG, MEG and NIRS. As discussed in Chapter 3 and 4, recurrence plots have been used to explore dynamical properties of EEG and MEG, providing interesting features on complex phenomena in human brain. Although the SYNC metric is extracted from cross recurrence plots, a separate and accurate analysis may be needed to assert the validity of the index in a broader context and extend its use to more functional imaging techniques.

Cross recurrence plots contain multiple information about the dynamic properties, so an extended multidimensional framework that exploits complete graphical patterns was developed in order to describe completely the functional interactions of couple of signals in the phase space. More specifically, a set of metrics is extracted from the CRP of each couple of signals to form a multi-layer connectivity matrix in which each layer is related to a specific complex phenomenon occurring in phase space. The proposed framework is used to

characterize functional abnormalities during both a WM task and executive task for individuals suffering from schizophrenia. Multi-layer networks are then topologically analyzed and graph-based centrality metrics are extracted from each functional layer. These metrics are treated as features in a classification problem to discriminate schizophrenic patients from healthy controls. Hence, machine-learning algorithms are used to identify markers of the dynamic states in brain activity to characterize pathological conditions in a clinical context. In this scenario, a statistical framework has been developed to make robust the selection of features and to select only those significantly related to anomalies. The main rationale of this choice is to offer to physicians a useful tool for diagnosis with high margins of accuracy. The cooperation between a multilayer framework with supervised classification algorithms has proven effective in revealing ROIs affected by the disease for both the analyzed experiments. This approach could be generalized for the study of different dynamic phenomena: in fact, on the one hand, a multidimensional representation of a phenomenon and on the other hand, the possibility of extrapolating the most significant information could turn to be a useful tool for investigating not only dynamics in brain, but also other physiological, natural, climatological, financial phenomena and so on. It is necessary to note that in the analysis, topological metrics have been extracted separately from each layer of the multilayer recurrence structure. The present exploratory approach can be significantly improved. For example, a reducibility analysis [213] could be performed to detect layers that can be aggregated. Indeed, although they are representative of different phenomena, some RQA metrics are dependent on each other so it may be possible to derive new layers of the multi-recurrence structure by appropriately combining pre-existing levels in order to obtain a final structure with non-redundant information. In addition, in future developments, multigraph metrics could be considered to effectively take into account the simultaneous presence of the multiple connectivity levels in phase space.

Another issue addressed in this work deals with the definition of a new metric of centrality in complex networks. The proposed resilience metric quantifies the importance of a node in relation to its survival rate for progressive removal of links in the network and can be useful for identifying the most persistent ROIs of the brain or in general nodes of a complex network. This metric is calculated considering multidimensional patterns of network connectivity and its comparison with other metrics known in literature also confirms the potentiality of a multivariate model. In fact, this metrics has proved more reliable than the

others in distinguishing the nodal ranking mechanism for networks with the same topology but different weight distribution. This results can be particularly useful in network inference, where it is required to use the partial information available about a network and try to reconstruct the most likely network, or an ensemble of likely networks, in the least biased way.

Finally, the last chapter shows the results achieved during two international challenges on the application of multidimensional methods for features selection in classification of individuals with brain lesions and cognitive decline. In this context, it was demonstrated that combining machine learning methods it is possible to develop new multimodal brain analysis tools and offer a valid diagnostic support for different brain states and pathologies. Again, the power of a multidimensional approach seems to indicate new and promising directions.

References

[1] Danielle S Bassett and Michael S Gazzaniga. Understanding complexity in the human brain. *Trends in cognitive sciences*, 15(5):200–209, 2011.

[2] Olaf Sporns. *Networks of the Brain*. MIT press, 2010.

[3] David Meunier, Renaud Lambiotte, and Edward T Bullmore. Modular and hierarchically modular organization of brain networks. *Frontiers in neuroscience*, 4:200, 2010.

[4] Olaf Sporns and Richard F Betzel. Modular brain networks. *Annual review of psychology*, 67:613–640, 2016.

[5] Olaf Sporns, Giulio Tononi, and Rolf Kötter. The human connectome: a structural description of the human brain. *PLoS computational biology*, 1(4):e42, 2005.

[6] Ed Bullmore and Olaf Sporns. Complex brain networks: graph theoretical analysis of structural and functional systems. *Nature reviews. Neuroscience*, 10(3):186, 2009.

[7] Olaf Sporns. The human connectome: a complex network. *Annals of the New York Academy of Sciences*, 1224(1):109–125, 2011.

[8] Alex Fornito, Andrew Zalesky, and Edward Bullmore. *Fundamentals of brain network analysis*. Academic Press, 2016.

[9] A Paul Alivisatos, Miyoung Chun, George M Church, Ralph J Greenspan, Michael L Roukes, and Rafael Yuste. The brain activity map project and the challenge of functional connectomics. *Neuron*, 74(6):970–974, 2012.

[10] Katrin Amunts, Christoph Ebell, Jeff Muller, Martin Telefont, Alois Knoll, and Thomas Lippert. The human brain project: creating a european research infrastructure to decode the human brain. *Neuron*, 92(3):574–581, 2016.

[11] Vasilis Z Marmarelis. *Nonlinear dynamic modeling of physiological systems*, volume 10. John Wiley & Sons, 2004.

[12] Mikhail I Rabinovich, Pablo Varona, Allen I Selverston, and Henry DI Abarbanel. Dynamical principles in neuroscience. *Reviews of modern physics*, 78(4):1213, 2006.

[13] Gregory L Baker and Jerry P Gollub. *Chaotic dynamics: an introduction*. Cambridge University Press, 1996.

[14] Ernesto Pereda, Rodrigo Quian Quiroga, and Joydeep Bhattacharya. Nonlinear multivariate analysis of neurophysiological signals. *Progress in neurobiology*, 77(1):1–37, 2005.

[15] Cornelis J Stam. Nonlinear dynamical analysis of eeg and meg: review of an emerging field. *Clinical neurophysiology*, 116(10):2266–2301, 2005.

[16] Tim Sauer, James A Yorke, and Martin Casdagli. Embedology. *Journal of statistical Physics*, 65(3):579–616, 1991.

[17] Alain Barrat, Marc Barthelemy, Romualdo Pastor-Satorras, and Alessandro Vespignani. The architecture of complex weighted networks. *Proceedings of the National Academy of Sciences of the United States of America*, 101(11):3747–3752, 2004.

[18] Mingrui Xia and Yong He. Functional connectomics from a "big data" perspective. *NeuroImage*, 2017.

[19] Mohammad R Arbabshirani, Sergey Plis, Jing Sui, and Vince D Calhoun. Single subject prediction of brain disorders in neuroimaging: Promises and pitfalls. *NeuroImage*, 145:137–165, 2017.

[20] Angela Lombardi, Sabina Tangaro, Roberto Bellotti, Alessandro Bertolino, Giuseppe Blasi, Giulio Pergola, Paolo Taurisano, and Cataldo Guaragnella. A novel synchronization-based approach for functional connectivity analysis. *Complexity*, 2017, 2017.

[21] Angela Lombardi, Pietro Guccione, Luigi Mascolo, Paolo Taurisano, Leonardo Fazio, and Giovanni Nico. Combining graph analysis and recurrence plot on fmri data. In *Medical Measurements and Applications (MeMeA), 2015 IEEE International Symposium on*, pages 18–23. IEEE, 2015.

[22] Angela Lombardi, Sabina Tangaro, Roberto Bellotti, Angelo Cardellicchio, Giuseppe Blasi, Paolo Taurisano, and Cataldo Guaragnella. Multidimensional complex measures for functional connectivity analysis. In *Sigmaphi 2017 - Book of Abstracts*, pages 68–69, 2017.

[23] Angela Lombardi, Sabina Tangaro, Roberto Bellotti, Angelo Cardellicchio, and Cataldo Guaragnella. Identification of "die hard" nodes in complex networks. In *WIVACE 2017 - Book of Abstracts*, pages 101–104. European Center for Living Technology, 2017.

[24] Roberto Bellotti, Angela Lombardi, Cataldo Guaragnella, Nicola Amoroso, Andrea Tateo, and Sabina Tangaro. Mild traumatic brain injury outcome prediction based on both graph and k-nn methods. In *International Workshop on Brainlesion: Glioma, Multiple Sclerosis, Stroke and Traumatic Brain Injuries*, pages 271–281. Springer, 2016.

[25] Nicola Amoroso, Domenico Diacono, Annarita Fanizzi, Marianna La Rocca, Alfonso Monaco, Angela Lombardi, Cataldo Guaragnella, Roberto Bellotti, and Sabina Tangaro. Deep learning reveals alzheimer's disease on-set in mci subjects: results from an international challenge. *Journal of Neuroscience Methods*, In minor revision.

[26] Suzana Herculano-Houzel. The human brain in numbers: a linearly scaled-up primate brain. *Frontiers in human neuroscience*, 3, 2009.

[27] Qawi K Telesford, Sean L Simpson, Jonathan H Burdette, Satoru Hayasaka, and Paul J Laurienti. The brain as a complex system: using network science as a tool for understanding the brain. *Brain connectivity*, 1(4):295–308, 2011.

[28] E Mark Haacke, Robert W Brown, Michael R Thompson, Ramesh Venkatesan, et al. *Magnetic resonance imaging: physical principles and sequence design*, volume 82. Wiley-Liss New York:, 1999.

[29] Peter J Basser, James Mattiello, and Denis LeBihan. Mr diffusion tensor spectroscopy and imaging. *Biophysical journal*, 66(1):259–267, 1994.

[30] Heidi Johansen-Berg and Timothy EJ Behrens. *Diffusion MRI: from quantitative measurement to in vivo neuroanatomy*. Academic Press, 2013.

[31] Jacques-Donald Tournier, Susumu Mori, and Alexander Leemans. Diffusion tensor imaging and beyond. *Magnetic resonance in medicine*, 65(6):1532–1556, 2011.

[32] Denis Le Bihan, Jean-François Mangin, Cyril Poupon, Chris A Clark, Sabina Pappata, Nicolas Molko, and Hughes Chabriat. Diffusion tensor imaging: concepts and applications. *Journal of magnetic resonance imaging*, 13(4):534–546, 2001.

[33] Matti Hämäläinen, Riitta Hari, Risto J Ilmoniemi, Jukka Knuutila, and Olli V Lounasmaa. Magnetoencephalography—theory, instrumentation, and applications to noninvasive studies of the working human brain. *Reviews of modern Physics*, 65(2):413, 1993.

[34] Ernst Niedermeyer and FH Lopes da Silva. *Electroencephalography: basic principles, clinical applications, and related fields*. Lippincott Williams & Wilkins, 2005.

[35] E Van Diessen, T Numan, E Van Dellen, AW Van Der Kooi, M Boersma, D Hofman, R Van Lutterveld, BW Van Dijk, ECW van Straaten, A Hillebrand, et al. Opportunities and methodological challenges in eeg and meg resting state functional brain network research. *Clinical Neurophysiology*, 126(8):1468–1481, 2015.

[36] Seiji Ogawa, Tso-Ming Lee, Alan R Kay, and David W Tank. Brain magnetic resonance imaging with contrast dependent on blood oxygenation. *Proceedings of the National Academy of Sciences*, 87(24):9868–9872, 1990.

[37] Nathalie Tzourio-Mazoyer, Brigitte Landeau, Dimitri Papathanassiou, Fabrice Crivello, Olivier Etard, Nicolas Delcroix, Bernard Mazoyer, and Marc Joliot. Automated anatomical labeling of activations in spm using a macroscopic anatomical parcellation of the mni mri single-subject brain. *Neuroimage*, 15(1):273–289, 2002.

[38] Victor M Eguiluz, Dante R Chialvo, Guillermo A Cecchi, Marwan Baliki, and A Vania Apkarian. Scale-free brain functional networks. *Physical review letters*, 94(1):018102, 2005.

[39] Jonathan D Power, Alexander L Cohen, Steven M Nelson, Gagan S Wig, Kelly Anne Barnes, Jessica A Church, Alecia C Vogel, Timothy O Laumann, Fran M Miezin, Bradley L Schlaggar, et al. Functional network organization of the human brain. *Neuron*, 72(4):665–678, 2011.

[40] Matthew L Stanley, Malaak N Moussa, Brielle M Paolini, Robert G Lyday, Jonathan H Burdette, and Paul J Laurienti. Defining nodes in complex brain networks. *Frontiers in computational neuroscience*, 7, 2013.

[41] Aaron Alexander-Bloch, Jay N Giedd, et al. Imaging structural covariance between human brain regions. *Nature Reviews. Neuroscience*, 14(5):322, 2013.

[42] Van J Wedeen, Patric Hagmann, Wen-Yih Isaac Tseng, Timothy G Reese, and Robert M Weisskoff. Mapping complex tissue architecture with diffusion spectrum magnetic resonance imaging. *Magnetic resonance in medicine*, 54(6):1377–1386, 2005.

[43] Karl J Friston. Functional and effective connectivity: a review. *Brain connectivity*, 1(1):13–36, 2011.

[44] KJ Friston, C Buechel, GR Fink, J Morris, E Rolls, and RJ Dolan. Psychophysiological and modulatory interactions in neuroimaging. *Neuroimage*, 6(3):218–229, 1997.

[45] Cornelis J Stam and Jaap C Reijneveld. Graph theoretical analysis of complex networks in the brain. *Nonlinear biomedical physics*, 1(1):3, 2007.

[46] Tore Opsahl, Filip Agneessens, and John Skvoretz. Node centrality in weighted networks: Generalizing degree and shortest paths. *Social networks*, 32(3):245–251, 2010.

[47] Ulrik Brandes. A faster algorithm for betweenness centrality. *Journal of mathematical sociology*, 25(2):163–177, 2001.

[48] Linton C Freeman. A set of measures of centrality based on betweenness. *Sociometry*, pages 35–41, 1977.

[49] Phillip Bonacich. Power and centrality: A family of measures. *American journal of sociology*, 92(5):1170–1182, 1987.

[50] Harold Hotelling. Simplified calculation of principal components. *Psychometrika*, 1(1):27–35, 1936.

[51] Sergey Brin and Lawrence Page. Reprint of: The anatomy of a large-scale hypertextual web search engine. *Computer networks*, 56(18):3825–3833, 2012.

[52] Jukka-Pekka Onnela, Jari Saramäki, János Kertész, and Kimmo Kaski. Intensity and coherence of motifs in weighted complex networks. *Physical Review E*, 71(6):065103, 2005.

[53] Mark EJ Newman. Assortative mixing in networks. *Physical review letters*, 89(20):208701, 2002.

[54] Santo Fortunato. Community detection in graphs. *Physics reports*, 486(3):75–174, 2010.

[55] Mark EJ Newman. Analysis of weighted networks. *Physical review E*, 70(5):056131, 2004.

[56] Andrea Lancichinetti and Santo Fortunato. Community detection algorithms: a comparative analysis. *Physical review E*, 80(5):056117, 2009.

[57] Andrew Zalesky, Luca Cocchi, Alex Fornito, Micah M Murray, and ED Bullmore. Connectivity differences in brain networks. *Neuroimage*, 60(2):1055–1062, 2012.

[58] Yoav Benjamini and Yosef Hochberg. Controlling the false discovery rate: a practical and powerful approach to multiple testing. *Journal of the royal statistical society. Series B (Methodological)*, pages 289–300, 1995.

[59] Andrew Zalesky, Alex Fornito, and Edward T Bullmore. Network-based statistic: identifying differences in brain networks. *Neuroimage*, 53(4):1197–1207, 2010.

[60] Francisco Pereira, Tom Mitchell, and Matthew Botvinick. Machine learning classifiers and fmri: a tutorial overview. *Neuroimage*, 45(1):S199–S209, 2009.

[61] Quentin JM Huys, Tiago V Maia, and Michael J Frank. Computational psychiatry as a bridge from neuroscience to clinical applications. *Nature neuroscience*, 19(3):404, 2016.

[62] Eleni Zarogianni, Thomas WJ Moorhead, and Stephen M Lawrie. Towards the identification of imaging biomarkers in schizophrenia, using multivariate pattern classification at a single-subject level. *NeuroImage: Clinical*, 3:279–289, 2013.

[63] Adeline Lo, Herman Chernoff, Tian Zheng, and Shaw-Hwa Lo. Why significant variables aren't automatically good predictors. *Proceedings of the National Academy of Sciences*, 112(45):13892–13897, 2015.

[64] Richard F Betzel and Danielle S Bassett. Multi-scale brain networks. *Neuroimage*, 2016.

[65] Vince D Calhoun and Jing Sui. Multimodal fusion of brain imaging data: A key to finding the missing link (s) in complex mental illness. *Biological psychiatry: cognitive neuroscience and neuroimaging*, 1(3):230–244, 2016.

[66] Manlio De Domenico. Multilayer modeling and analysis of human brain networks. *Giga Science*, 6(5):1–8, 2017.

[67] Federico Battiston, Vincenzo Nicosia, Mario Chavez, and Vito Latora. Multilayer motif analysis of brain networks. *Chaos: An Interdisciplinary Journal of Nonlinear Science*, 27(4):047404, 2017.

[68] Manlio De Domenico, Albert Solé-Ribalta, Emanuele Cozzo, Mikko Kivelä, Yamir Moreno, Mason A Porter, Sergio Gómez, and Alex Arenas. Mathematical formulation of multilayer networks. *Physical Review X*, 3(4):041022, 2013.

[69] Vince D Calhoun, Robyn Miller, Godfrey Pearlson, and Tulay Adalı. The chronnectome: time-varying connectivity networks as the next frontier in fmri data discovery. *Neuron*, 84(2):262–274, 2014.

[70] Danielle S Bassett, Nicholas F Wymbs, Mason A Porter, Peter J Mucha, Jean M Carlson, and Scott T Grafton. Dynamic reconfiguration of human brain networks during learning. *Proceedings of the National Academy of Sciences*, 108(18):7641–7646, 2011.

[71] Richard F Betzel, Bratislav Mišić, Ye He, Jeffrey Rumschlag, Xi-Nian Zuo, and Olaf Sporns. Functional brain modules reconfigure at multiple scales across the human lifespan. *arXiv preprint arXiv:1510.08045*, 2015.

[72] Urs Braun, Axel Schäfer, Henrik Walter, Susanne Erk, Nina Romanczuk-Seiferth, Leila Haddad, Janina I Schweiger, Oliver Grimm, Andreas Heinz, Heike Tost, et al. Dynamic reconfiguration of frontal brain networks during executive cognition in humans. *Proceedings of the National Academy of Sciences*, 112(37):11678–11683, 2015.

[73] Manlio De Domenico, Shuntaro Sasai, and Alex Arenas. Mapping multiplex hubs in human functional brain networks. *Frontiers in neuroscience*, 10, 2016.

[74] Matthew J Brookes, Prejaas K Tewarie, Benjamin AE Hunt, Sian E Robson, Lauren E Gascoyne, Elizabeth B Liddle, Peter F Liddle, and Peter G Morris. A multi-layer network approach to meg connectivity analysis. *Neuroimage*, 132:425–438, 2016.

[75] Jérémy Guillon, Yohan Attal, Olivier Colliot, Valentina La Corte, Bruno Dubois, Denis Schwartz, Mario Chavez, and F De Vico Fallani. Loss of brain inter-frequency hubs in alzheimer's disease. *Scientific Reports*, 7, 2017.

[76] Mikail Rubinov and Olaf Sporns. Complex network measures of brain connectivity: uses and interpretations. *Neuroimage*, 52(3):1059–1069, 2010.

[77] Danielle Smith Bassett and ED Bullmore. Small-world brain networks. *The neuroscientist*, 12(6):512–523, 2006.

[78] Martijn P van den Heuvel and Olaf Sporns. Network hubs in the human brain. *Trends in cognitive sciences*, 17(12):683–696, 2013.

[79] Urs Braun, Sarah F Muldoon, and Danielle S Bassett. On human brain networks in health and disease. *eLS*, 2015.

[80] Felice T Sun, Lee M Miller, and Mark D'Esposito. Measuring interregional functional connectivity using coherence and partial coherence analyses of fmri data. *Neuroimage*, 21(2):647–658, 2004.

[81] Xia Liang, Jinhui Wang, Chaogan Yan, Ni Shu, Ke Xu, Gaolang Gong, and Yong He. Effects of different correlation metrics and preprocessing factors on small-world brain functional networks: a resting-state functional mri study. *PloS one*, 7(3):e32766, 2012.

[82] Stephen M Smith, Karla L Miller, Gholamreza Salimi-Khorshidi, Matthew Webster, Christian F Beckmann, Thomas E Nichols, Joseph D Ramsey, and Mark W Woolrich. Network modelling methods for fmri. *Neuroimage*, 54(2):875–891, 2011.

[83] Gustavo Deco, Viktor K Jirsa, Peter A Robinson, Michael Breakspear, and Karl Friston. The dynamic brain: from spiking neurons to neural masses and cortical fields. *PLoS Comput Biol*, 4(8):e1000092, 2008.

[84] Michael W Cole, Danielle S Bassett, Jonathan D Power, Todd S Braver, and Steven E Petersen. Intrinsic and task-evoked network architectures of the human brain. *Neuron*, 83(1):238–251, 2014.

[85] Ed Bullmore and Olaf Sporns. The economy of brain network organization. *Nature Reviews Neuroscience*, 13(5):336–349, 2012.

[86] Norbert Marwan and Jürgen Kurths. Nonlinear analysis of bivariate data with cross recurrence plots. *Physics Letters A*, 302(5):299–307, 2002.

[87] Danielle S Bassett, Nicholas F Wymbs, M Puck Rombach, Mason A Porter, Peter J Mucha, and Scott T Grafton. Task-based core-periphery organization of human brain dynamics. *PLoS computational biology*, 9(9):e1003171, 2013.

[88] Qawi K Telesford, Mary-Ellen Lynall, Jean Vettel, Michael B Miller, Scott T Grafton, and Danielle S Bassett. Detection of functional brain network reconfiguration during task-driven cognitive states. *Neuroimage*, 142:198–210, 2016.

[89] DEMOGRAPHIC DATA. *Structured clinical interview for DSM-IV axis I disorders*. American Psychiatric Press, Washington, 1997.

[90] August B Hollingshead et al. Four factor index of social status. 1975.

[91] Richard C Oldfield. The assessment and analysis of handedness: the edinburgh inventory. *Neuropsychologia*, 9(1):97–113, 1971.

[92] Arturo Orsini and Caterina Laicardi. Factor structure of the italian version of the wais—r compared with the american standardization. *Perceptual and motor skills*, 90(3_suppl):1091–1100, 2000.

[93] Lingzhong Fan, Hai Li, Junjie Zhuo, Yu Zhang, Jiaojian Wang, Liangfu Chen, Zhengyi Yang, Congying Chu, Sangma Xie, Angela R Laird, et al. The human brainnetome atlas: a new brain atlas based on connectional architecture. *Cerebral Cortex*, 26(8):3508–3526, 2016.

[94] Floris Takens. Detecting strange attractors in turbulence. In *Dynamical systems and turbulence, Warwick 1980*, pages 366–381. Springer, 1981.

[95] Andrew M Fraser and Harry L Swinney. Independent coordinates for strange attractors from mutual information. *Physical review A*, 33(2):1134, 1986.

[96] Matthew B Kennel, Reggie Brown, and Henry DI Abarbanel. Determining embedding dimension for phase-space reconstruction using a geometrical construction. *Physical review A*, 45(6):3403, 1992.

[97] Gabriel M Mindlin and R Gilmore. Topological analysis and synthesis of chaotic time series. *Physica D: Nonlinear Phenomena*, 58(1-4):229–242, 1992.

[98] Marco Thiel, M Carmen Romano, Jürgen Kurths, Riccardo Meucci, Enrico Allaria, and F Tito Arecchi. Influence of observational noise on the recurrence quantification analysis. *Physica D: Nonlinear Phenomena*, 171(3):138–152, 2002.

[99] Norbert Marwan, M Carmen Romano, Marco Thiel, and Jürgen Kurths. Recurrence plots for the analysis of complex systems. *Physics reports*, 438(5):237–329, 2007.

[100] N Marwan, M Thiel, and NR Nowaczyk. Cross recurrence plot based synchronization of time series. *arXiv preprint physics/0201062*, 2002.

[101] Mark EJ Newman. Modularity and community structure in networks. *Proceedings of the national academy of sciences*, 103(23):8577–8582, 2006.

[102] Martin Rosvall and Carl T Bergstrom. Maps of random walks on complex networks reveal community structure. *Proceedings of the National Academy of Sciences*, 105(4):1118–1123, 2008.

[103] Vincent D Blondel, Jean-Loup Guillaume, Renaud Lambiotte, and Etienne Lefebvre. Fast unfolding of communities in large networks. *Journal of statistical mechanics: theory and experiment*, 2008(10):P10008, 2008.

[104] Aaron Alexander-Bloch, Renaud Lambiotte, Ben Roberts, Jay Giedd, Nitin Gogtay, and Ed Bullmore. The discovery of population differences in network community structure: new methods and applications to brain functional networks in schizophrenia. *Neuroimage*, 59(4):3889–3900, 2012.

[105] Ludmila I Kuncheva and Stefan Todorov Hadjitodorov. Using diversity in cluster ensembles. In *Systems, man and cybernetics, 2004 IEEE international conference on*, volume 2, pages 1214–1219. IEEE, 2004.

[106] Radek Ptak, Armin Schnider, and Julia Fellrath. The dorsal frontoparietal network: A core system for emulated action. *Trends in Cognitive Sciences*, 2017.

[107] Joseph H Callicott, Nicolas F Ramsey, Kathleen Tallent, Alessandro Bertolino, Michael B Knable, Richard Coppola, Terry Goldberg, Peter van Gelderen, Venkata S Mattay, Joseph A Frank, et al. Functional magnetic resonance imaging brain mapping in psychiatry: methodological issues illustrated in a study of working memory in schizophrenia. *Neuropsychopharmacology*, 18(3):186–196, 1998.

[108] Fabio Sambataro, Giuseppe Blasi, Leonardo Fazio, Grazia Caforio, Paolo Taurisano, Raffaella Romano, Annabella Di Giorgio, Barbara Gelao, Luciana Lo Bianco, Apostolos Papazacharias, et al. Treatment with olanzapine is associated with modulation of the default mode network in patients with schizophrenia. *Neuropsychopharmacology*, 35(4):904, 2010.

[109] Kieran CR Fox, R Nathan Spreng, Melissa Ellamil, Jessica R Andrews-Hanna, and Kalina Christoff. The wandering brain: Meta-analysis of functional neuroimaging studies of mind-wandering and related spontaneous thought processes. *Neuroimage*, 111:611–621, 2015.

[110] Pengmin Qin and Georg Northoff. How is our self related to midline regions and the default-mode network? *Neuroimage*, 57(3):1221–1233, 2011.

[111] Jason M Scimeca and David Badre. Striatal contributions to declarative memory retrieval. *Neuron*, 75(3):380–392, 2012.

[112] Jari Peräkylä, Lihua Sun, Kai Lehtimäki, Jukka Peltola, Juha Öhman, Timo Möttönen, Keith H Ogawa, and Kaisa M Hartikainen. Causal evidence from humans for the role of mediodorsal nucleus of the thalamus in working memory. *Journal of Cognitive Neuroscience*, 2017.

[113] Joseph H Callicott, Venkata S Mattay, Alessandro Bertolino, Kimberly Finn, Richard Coppola, Joseph A Frank, Terry E Goldberg, and Daniel R Weinberger. Physiological characteristics of capacity constraints in working memory as revealed by functional mri. *Cerebral Cortex*, 9(1):20–26, 1999.

[114] Danielle S Bassett, Daniel L Greenfield, Andreas Meyer-Lindenberg, Daniel R Weinberger, Simon W Moore, and Edward T Bullmore. Efficient physical embedding of topologically complex information processing networks in brains and computer circuits. *PLoS Comput Biol*, 6(4):e1000748, 2010.

[115] Damien A Fair, Alexander L Cohen, Jonathan D Power, Nico UF Dosenbach, Jessica A Church, Francis M Miezin, Bradley L Schlaggar, and Steven E Petersen. Functional brain networks develop from a "local to distributed" organization. *PLoS comput biol*, 5(5):e1000381, 2009.

[116] Aaron F Alexander-Bloch, Nitin Gogtay, David Meunier, Rasmus Birn, Liv Clasen, Francois Lalonde, Rhoshel Lenroot, Jay Giedd, and Edward T Bullmore. Disrupted modularity and local connectivity of brain functional networks in childhood-onset schizophrenia. *Frontiers in systems neuroscience*, 4:147, 2010.

[117] Jinhui Wang, Xinian Zuo, Zhengjia Dai, Mingrui Xia, Zhilian Zhao, Xiaoling Zhao, Jianping Jia, Ying Han, and Yong He. Disrupted functional brain connectome in individuals at risk for alzheimer's disease. *Biological psychiatry*, 73(5):472–481, 2013.

[118] Jeffrey D Rudie, JA Brown, D Beck-Pancer, LM Hernandez, EL Dennis, PM Thompson, SY Bookheimer, and M Dapretto. Altered functional and structural brain network organization in autism. *NeuroImage: clinical*, 2:79–94, 2013.

[119] Xiaoping Xie, Zhitong Cao, and Xuchu Weng. Spatiotemporal nonlinearity in resting-state fmri of the human brain. *Neuroimage*, 40(4):1672–1685, 2008.

[120] Marta Bianciardi, Paolo Sirabella, Gisela E Hagberg, Alessandro Giuliani, Joseph P Zbilut, and Alfredo Colosimo. Model-free analysis of brain fmri data by recurrence quantification. *NeuroImage*, 37(2):489–503, 2007.

[121] U Rajendra Acharya, S Vinitha Sree, Subhagata Chattopadhyay, Wenwei Yu, and Peng Chuan Alvin Ang. Application of recurrence quantification analysis for the automated identification of epileptic eeg signals. *International journal of neural systems*, 21(03):199–211, 2011.

[122] David E McCarty, Naresh M Punjabi, Paul Y Kim, Clifton Frilot, and Andrew A Marino. Recurrence analysis of the eeg during sleep accurately identifies subjects with mental health symptoms. *Psychiatry Research: Neuroimaging*, 224(3):335–340, 2014.

[123] Leena T Timothy, Bindu M Krishna, and Usha Nair. Classification of mild cognitive impairment eeg using combined recurrence and cross recurrence quantification analysis. *International Journal of Psychophysiology*, 120:86–95, 2017.

[124] Charles L Webber Jr and Norbert Marwan. *Recurrence quantification analysis*. Springer, 2015.

[125] Angela Lombardi, Pietro Guccione, and Cataldo Guaragnella. Exploring recurrence properties of vowels for analysis of emotions in speech. *Sensors & Transducers*, 204(9):45, 2016.

[126] Joseph P Zbilut and Charles L Webber. Embeddings and delays as derived from quantification of recurrence plots. *Physics letters A*, 171(3-4):199–203, 1992.

[127] Reik V Donner, Yong Zou, Jonathan F Donges, Norbert Marwan, and Jürgen Kurths. Recurrence networks—a novel paradigm for nonlinear time series analysis. *New Journal of Physics*, 12(3):033025, 2010.

[128] Reik V Donner, Jobst Heitzig, Jonathan F Donges, Yong Zou, Norbert Marwan, and Jürgen Kurths. The geometry of chaotic dynamics–a complex network perspective. *arXiv preprint arXiv:1102.1853*, 2011.

[129] Isabelle Guyon and André Elisseeff. An introduction to variable and feature selection. *Journal of machine learning research*, 3(Mar):1157–1182, 2003.

[130] Isabelle Guyon, Jason Weston, Stephen Barnhill, and Vladimir Vapnik. Gene selection for cancer classification using support vector machines. *Machine learning*, 46(1):389–422, 2002.

[131] Corinna Cortes and Vladimir Vapnik. Support vector machine. *Machine learning*, 20(3):273–297, 1995.

[132] Ke Yan and David Zhang. Feature selection and analysis on correlated gas sensor data with recursive feature elimination. *Sensors and Actuators B: Chemical*, 212:353–363, 2015.

[133] Surendra K Singhi and Huan Liu. Feature subset selection bias for classification learning. In *Proceedings of the 23rd international conference on Machine learning*, pages 849–856. ACM, 2006.

[134] Nikolaus Kriegeskorte, W Kyle Simmons, Patrick SF Bellgowan, and Chris I Baker. Circular analysis in systems neuroscience: the dangers of double dipping. *Nature neuroscience*, 12(5):535–540, 2009.

[135] Emanuele Olivetti, Andrea Mognon, Susanne Greiner, and Paolo Avesani. Brain decoding: biases in error estimation. In *Brain Decoding: Pattern Recognition Challenges in Neuroimaging (WBD), 2010 First Workshop on*, pages 40–43. IEEE, 2010.

[136] Simon F Eskildsen, Pierrick Coupé, Daniel García-Lorenzo, Vladimir Fonov, Jens C Pruessner, D Louis Collins, Alzheimer's Disease Neuroimaging Initiative, et al. Prediction of alzheimer's disease in subjects with mild cognitive impairment from the adni cohort using patterns of cortical thinning. *Neuroimage*, 65:511–521, 2013.

[137] Eugen Bleuler. Dementia praecox or the group of schizophrenias. 1950.

[138] Karl J Friston. The disconnection hypothesis. *Schizophrenia research*, 30(2):115–125, 1998.

[139] Martijn P van den Heuvel and Alex Fornito. Brain networks in schizophrenia. *Neuropsychology review*, 24(1):32–48, 2014.

[140] Andreas S Meyer-Lindenberg, Rosanna K Olsen, Philip D Kohn, Timothy Brown, Michael F Egan, Daniel R Weinberger, and Karen Faith Berman. Regionally specific disturbance of dorsolateral prefrontal–hippocampal functional connectivity in schizophrenia. *Archives of general psychiatry*, 62(4):379–386, 2005.

[141] Peter J Uhlhaas and Wolf Singer. Abnormal neural oscillations and synchrony in schizophrenia. *Nature reviews neuroscience*, 11(2):100, 2010.

[142] E Angelopoulos. Brain functional connectivity and the pathophysiology of schizophrenia. *Psychiatrike= Psychiatriki*, 25(2):91–94, 2014.

[143] Stefano Boccaletti, Vito Latora, Yamir Moreno, Martin Chavez, and D-U Hwang. Complex networks: Structure and dynamics. *Physics reports*, 424(4):175–308, 2006.

[144] Luıs A Nunes Amaral, Antonio Scala, Marc Barthelemy, and H Eugene Stanley. Classes of small-world networks. *Proceedings of the national academy of sciences*, 97(21):11149–11152, 2000.

[145] Albert-László Barabási. Scale-free networks: a decade and beyond. *science*, 325(5939):412–413, 2009.

[146] Luca Dall'Asta, Alain Barrat, Marc Barthélemy, and Alessandro Vespignani. Vulnerability of weighted networks. *Journal of Statistical Mechanics: Theory and Experiment*, 2006(04):P04006, 2006.

[147] Reuven Cohen and Shlomo Havlin. *Complex networks: structure, robustness and function*. Cambridge university press, 2010.

[148] Amnon Aharony and Dietrich Stauffer. *Introduction to percolation theory*. Taylor & Francis, 2003.

[149] Béla Bollobás and Oliver Riordan. *Percolation*. Cambridge University Press, 2006.

[150] Réka Albert and Albert-László Barabási. Statistical mechanics of complex networks. *Reviews of modern physics*, 74(1):47, 2002.

[151] Vladimir Gol'dshtein, GA Koganov, and Gregory I Surdutovich. Vulnerability and hierarchy of complex networks. *arXiv preprint cond-mat/0409298*, 2004.

[152] Vito Latora and Massimo Marchiori. Vulnerability and protection of infrastructure networks. *Physical Review E*, 71(1):015103, 2005.

[153] Stefano Boccaletti, Javier Buldú, Regino Criado, Julio Flores, Vito Latora, Javier Pello, and Miguel Romance. Multiscale vulnerability of complex networks. *Chaos: An Interdisciplinary Journal of Nonlinear Science*, 17(4):043110, 2007.

[154] Igor Mishkovski, Mario Biey, and Ljupco Kocarev. Vulnerability of complex networks. *Communications in Nonlinear Science and Numerical Simulation*, 16(1):341–349, 2011.

[155] Mahendra Piraveenan, Mikhail Prokopenko, and Liaquat Hossain. Percolation centrality: Quantifying graph-theoretic impact of nodes during percolation in networks. *PloS one*, 8(1):e53095, 2013.

[156] M Angeles Serrano, Marián Boguná, and Albert Díaz-Guilera. Competition and adaptation in an internet evolution model. *Physical review letters*, 94(3):038701, 2005.

[157] Diego Garlaschelli, Stefano Battiston, Maurizio Castri, Vito DP Servedio, and Guido Caldarelli. The scale-free topology of market investments. *Physica A: Statistical Mechanics and its Applications*, 350(2):491–499, 2005.

[158] Albert-László Barabási and Réka Albert. Emergence of scaling in random networks. *science*, 286(5439):509–512, 1999.

[159] Marc Barthélemy, Alain Barrat, Romualdo Pastor-Satorras, and Alessandro Vespignani. Characterization and modeling of weighted networks. *Physica a: Statistical mechanics and its applications*, 346(1):34–43, 2005.

[160] Ginestra Bianconi. Emergence of weight-topology correlations in complex scale-free networks. *EPL (Europhysics Letters)*, 71(6):1029, 2005.

[161] Stephen P Borgatti and Martin G Everett. A graph-theoretic perspective on centrality. *Social networks*, 28(4):466–484, 2006.

[162] Nicola Amoroso, Alfonso Monaco, and Sabina Tangaro. Topological measurements of DWI tractography for the Alzheimer's disease detection. *Computational and mathematical methods in medicine*, in press, 2016.

[163] Andrew L Alexander, Samuel A Hurley, Alexey A Samsonov, Nagesh Adluru, Ameer Pasha Hosseinbor, Pouria Mossahebi, Do PM Tromp, Elizabeth Zakszewski, and Aaron S Field. Characterization of cerebral white matter properties using quantitative magnetic resonance imaging stains. *Brain connectivity*, 1(6):423–446, 2011.

[164] Mark EJ Newman. Finding community structure in networks using the eigenvectors of matrices. *Physical review E*, 74(3):036104, 2006.

[165] Roger Guimera and Luis A Nunes Amaral. Functional cartography of complex metabolic networks. *Nature*, 433(7028):895–900, 2005.

[166] Bruce Fischl, David H Salat, Evelina Busa, Marilyn Albert, Megan Dieterich, Christian Haselgrove, Andre Van Der Kouwe, Ron Killiany, David Kennedy, Shuna Klaveness, et al. Whole brain segmentation: automated labeling of neuroanatomical structures in the human brain. *Neuron*, 33(3):341–355, 2002.

[167] Anders M Dale, Bruce Fischl, and Martin I Sereno. Cortical surface-based analysis: I. Segmentation and surface reconstruction. *Neuroimage*, 9(2):179–194, 1999.

[168] Bruce Fischl and Anders M Dale. Measuring the thickness of the human cerebral cortex from magnetic resonance images. *Proceedings of the National Academy of Sciences*, 97(20):11050–11055, 2000.

[169] Bruce Fischl, Arthur Liu, and Anders M Dale. Automated manifold surgery: constructing geometrically accurate and topologically correct models of the human cerebral cortex. *IEEE transactions on medical imaging*, 20(1):70–80, 2001.

[170] Bruce Fischl, David H Salat, André JW van der Kouwe, Nikos Makris, Florent Ségonne, Brian T Quinn, and Anders M Dale. Sequence-independent segmentation of magnetic resonance images. *Neuroimage*, 23:S69–S84, 2004.

[171] Bruce Fischl, Martin I Sereno, and Anders M Dale. Cortical surface-based analysis: Ii: inflation, flattening, and a surface-based coordinate system. *Neuroimage*, 9(2):195–207, 1999.

[172] Bruce Fischl, Martin I Sereno, Roger BH Tootell, Anders M Dale, et al. High-resolution intersubject averaging and a coordinate system for the cortical surface. *Human brain mapping*, 8(4):272–284, 1999.

[173] Bruce Fischl, André van der Kouwe, Christophe Destrieux, Eric Halgren, Florent Ségonne, David H Salat, Evelina Busa, Larry J Seidman, Jill Goldstein, David Kennedy, et al. Automatically parcellating the human cerebral cortex. *Cerebral cortex*, 14(1):11–22, 2004.

[174] Xiao Han, Jorge Jovicich, David Salat, Andre van der Kouwe, Brian Quinn, Silvester Czanner, Evelina Busa, Jenni Pacheco, Marilyn Albert, Ronald Killiany, et al. Reliability of MRI-derived measurements of human cerebral cortical thickness: the effects of field strength, scanner upgrade and manufacturer. *Neuroimage*, 32(1):180–194, 2006.

[175] Jorge Jovicich, Silvester Czanner, Douglas Greve, Elizabeth Haley, Andre van der Kouwe, Randy Gollub, David Kennedy, Franz Schmitt, Gregory Brown, James MacFall, et al. Reliability in multi-site structural mri studies: effects of gradient non-linearity correction on phantom and human data. *Neuroimage*, 30(2):436–443, 2006.

[176] Florent Ségonne, AM Dale, E Busa, M Glessner, D Salat, HK Hahn, and B Fischl. A hybrid approach to the skull stripping problem in MRI. *Neuroimage*, 22(3):1060–1075, 2004.

[177] Anders M Dale and Martin I Sereno. Improved localizadon of cortical activity by combining EEG and MEG with MRI cortical surface reconstruction: a linear approach. *Journal of cognitive neuroscience*, 5(2):162–176, 1993.

[178] Martin Reuter, H Diana Rosas, and Bruce Fischl. Highly accurate inverse consistent registration: a robust approach. *Neuroimage*, 53(4):1181–1196, 2010.

[179] John G Sled, Alex P Zijdenbos, and Alan C Evans. A nonparametric method for automatic correction of intensity nonuniformity in mri data. *IEEE transactions on medical imaging*, 17(1):87–97, 1998.

[180] Florent Ségonne, Jenni Pacheco, and Bruce Fischl. Geometrically accurate topology-correction of cortical surfaces using nonseparating loops. *IEEE transactions on medical imaging*, 26(4):518–529, 2007.

[181] Rahul S Desikan, Florent Ségonne, Bruce Fischl, Brian T Quinn, Bradford C Dickerson, Deborah Blacker, Randy L Buckner, Anders M Dale, R Paul Maguire, Bradley T Hyman, et al. An automated labeling system for subdividing the human cerebral cortex on MRI scans into gyral based regions of interest. *Neuroimage*, 31(3):968–980, 2006.

[182] HD Rosas, AK Liu, S Hersch, M Glessner, RJ Ferrante, DH Salat, A van Der Kouwe, BG Jenkins, AM Dale, and B Fischl. Regional and progressive thinning of the cortical ribbon in Huntington's disease. *Neurology*, 58(5):695–701, 2002.

[183] Gina R Kuperberg, Matthew R Broome, Philip K McGuire, Anthony S David, Marianna Eddy, Fujiro Ozawa, Donald Goff, W Caroline West, Steven CR Williams, Andre JW van der Kouwe, et al. Regionally localized thinning of the cerebral cortex in schizophrenia. *Archives of general psychiatry*, 60(9):878–888, 2003.

[184] David H Salat, Randy L Buckner, Abraham Z Snyder, Douglas N Greve, Rahul SR Desikan, Evelina Busa, John C Morris, Anders M Dale, and Bruce Fischl. Thinning of the cerebral cortex in aging. *Cerebral cortex*, 14(7):721–730, 2004.

[185] Martin Reuter, Nicholas J Schmansky, H Diana Rosas, and Bruce Fischl. Within-subject template estimation for unbiased longitudinal image analysis. *Neuroimage*, 61(4):1402–1418, 2012.

[186] Raj Kumar, Mazhar Husain, Rakesh K Gupta, Khader M Hasan, Mohammad Haris, Atul K Agarwal, CM Pandey, and Ponnada A Narayana. Serial changes in the white matter diffusion tensor imaging metrics in moderate traumatic brain injury and correlation with neuro-cognitive function. *Journal of neurotrauma*, 26(4):481–495, 2009.

[187] RB Marimont and MB Shapiro. Nearest neighbour searches and the curse of dimensionality. *IMA Journal of Applied Mathematics*, 24(1):59–70, 1979.

[188] S Tangaro, N Amoroso, Marina Boccardi, S Bruno, A Chincarini, G Ferraro, Giovanni Battista Frisoni, R Maglietta, Alberto Redolfi, L Rei, et al. Automated voxel-by-voxel tissue classification for hippocampal segmentation: methods and validation. *Physica Medica*, 30(8):878–887, 2014.

[189] N Amoroso, R Errico, S Bruno, A Chincarini, E Garuccio, F Sensi, S Tangaro, A Tateo, R Bellotti, Alzheimers Disease Neuroimaging Initiative, et al. Hippocampal unified multi-atlas network (HUMAN): protocol and scale validation of a novel segmentation tool. *Physics in medicine and biology*, 60(22):8851, 2015.

[190] Andrea Chincarini, Francesco Sensi, Luca Rei, Gianluca Gemme, Sandro Squarcia, Renata Longo, Francesco Brun, Sabina Tangaro, Roberto Bellotti, Nicola Amoroso, et al. Integrating longitudinal information in hippocampal volume measurements for the early detection of Alzheimer's disease. *Neuroimage*, 125:834–847, 2016.

[191] Sabina Tangaro, Annarita Fanizzi, Nicola Amoroso, Roberto Bellotti, Alzheimer's Disease Neuroimaging Initiative, et al. A fuzzy-based system reveals Alzheimer's Disease onset in subjects with Mild Cognitive Impairment. *Physica Medica*, 38:36–44, 2017.

[192] Esther E Bron, Marion Smits, Wiesje M Van Der Flier, Hugo Vrenken, Frederik Barkhof, Philip Scheltens, Janne M Papma, Rebecca ME Steketee, Carolina Méndez Orellana, Rozanna Meijboom, et al. Standardized evaluation of algorithms for computer-aided diagnosis of dementia based on structural MRI: the CADDementia challenge. *NeuroImage*, 111:562–579, 2015.

[193] Genevera I Allen, Nicola Amoroso, Catalina Anghel, Venkat Balagurusamy, Christopher J Bare, Derek Beaton, Roberto Bellotti, David A Bennett, Kevin L Boehme, Paul C Boutros, et al. Crowdsourced estimation of cognitive decline and resilience in Alzheimer's disease. *Alzheimer's & Dementia*, 12(6):645–653, 2016.

[194] Christos Davatzikos, Priyanka Bhatt, Leslie M Shaw, Kayhan N Batmanghelich, and John Q Trojanowski. Prediction of MCI to AD conversion, via MRI, CSF biomarkers, and pattern classification. *Neurobiology of aging*, 32(12):2322–e19, 2011.

[195] Youngsang Cho, Joon-Kyung Seong, Yong Jeong, Sung Yong Shin, Alzheimer's Disease Neuroimaging Initiative, et al. Individual subject classification for Alzheimer's disease based on incremental learning using a spatial frequency representation of cortical thickness data. *Neuroimage*, 59(3):2217–2230, 2012.

[196] Daoqiang Zhang, Dinggang Shen, Alzheimer's Disease Neuroimaging Initiative, et al. Predicting future clinical changes of MCI patients using longitudinal and multimodal biomarkers. *PloS one*, 7(3):e33182, 2012.

[197] Elaheh Moradi, Antonietta Pepe, Christian Gaser, Heikki Huttunen, Jussi Tohka, Alzheimer's Disease Neuroimaging Initiative, et al. Machine learning framework for early MRI-based Alzheimer's conversion prediction in MCI subjects. *Neuroimage*, 104:398–412, 2015.

[198] J Young, M Modat, MJ Cardoso, A Mendelson, D Cash, S Ourselin, et al. Accurate multimodal probabilistic prediction of conversion to Alzheimer's disease in patients with mild cognitive impairment. *NeuroImage: Clinical*, 2:735–45, 2013.

[199] R Filipovych, C Davatzikos, Alzheimer's Disease Neuroimaging Initiative, et al. Semi-supervised pattern classification of medical images: application to mild cognitive impairment (MCI). *NeuroImage*, 55(3):1109–19, 2011.

[200] Leo Breiman. Random forests. *Machine learning*, 45(1):5–32, 2001.

[201] Geoffrey E Hinton, Simon Osindero, and Yee-Whye Teh. A fast learning algorithm for deep belief nets. *Neural computation*, 18(7):1527–1554, 2006.

[202] Yoshua Bengio, Pascal Lamblin, Dan Popovici, Hugo Larochelle, et al. Greedy layer-wise training of deep networks. *Advances in neural information processing systems*, 19:153, 2007.

[203] Ian Goodfellow, Yoshua Bengio, and Aaron Courville. *Deep Learning*. MIT Press, 2016. http://www.deeplearningbook.org.

[204] Hoo-Chang Shin, Holger R Roth, Mingchen Gao, Le Lu, Ziyue Xu, Isabella Nogues, Jianhua Yao, Daniel Mollura, and Ronald M Summers. Deep convolutional neural networks for computer-aided detection: CNN architectures, dataset characteristics and transfer learning. *IEEE transactions on medical imaging*, 35(5):1285–1298, 2016.

[205] Thijs Kooi, Geert Litjens, Bram van Ginneken, Albert Gubern-Mérida, Clara I Sánchez, Ritse Mann, Ard den Heeten, and Nico Karssemeijer. Large scale deep learning for computer aided detection of mammographic lesions. *Medical image analysis*, 35:303–312, 2017.

[206] Andre Esteva, Brett Kuprel, Roberto A Novoa, Justin Ko, Susan M Swetter, Helen M Blau, and Sebastian Thrun. Dermatologist-level classification of skin cancer with deep neural networks. *Nature*, 542(7639):115–118, 2017.

[207] Raman Arora, Amitabh Basu, Poorya Mianjy, and Anirbit Mukherjee. Understanding Deep Neural Networks with Rectified Linear Units. *arXiv preprint arXiv:1611.01491*, 2016.

[208] Diederik Kingma and Jimmy Ba. Adam: A method for stochastic optimization. *arXiv preprint arXiv:1412.6980*, 2014.

[209] DP Devanand, Ravi Bansal, Jun Liu, Xuejun Hao, Gnanavalli Pradhaban, and Bradley S Peterson. MRI hippocampal and entorhinal cortex mapping in predicting conversion to Alzheimer's disease. *Neuroimage*, 60(3):1622–29, 2012.

[210] KK Leung, J Barnes, GR Ridgway, JW Bartlett, MJ Clarkson, K Macdonald, et al. Automated cross-sectional and longitudinal hippocampal volume measurement in mild cognitive impairment and Alzheimer's disease. *Neuroimage*, 51(4):1345–59, 2010.

[211] L Zadeh. From computing with numbers to computing with words—from manipulation of measurements to manipulation of perceptions. In *Logic, Thought and Action*, pages 507–44. Springer, 1999.

[212] Siqi Liu, Sidong Liu, Weidong Cai, Hangyu Che, Sonia Pujol, Ron Kikinis, Dagan Feng, Michael J Fulham, et al. Multimodal neuroimaging feature learning for multiclass diagnosis of alzheimer's disease. *IEEE Transactions on Biomedical Engineering*, 62(4):1132–1140, 2015.

[213] Manlio De Domenico, Vincenzo Nicosia, Alexandre Arenas, and Vito Latora. Structural reducibility of multilayer networks. *Nature communications*, 6:ncomms7864, 2015.